BROADBAND SEMICONDUCTOR LASER AS A SOURCE IN OPTICAL COMMUNICATION SYSTEMS

BY

EMAD ABDULSHAFI ALKHAZRAJI

A Thesis Presented to the
DEANSHIP OF GRADUATE STUDIES

KING FAHD UNIVERSITY OF PETROLEUM & MINERALS

DHAHRAN, SAUDI ARABIA

In Partial Fulfillment of the
Requirements for the Degree of

MASTER OF SCIENCE

In

ELECTRICAL ENGINEERING

May 2016

KING FAHD UNIVERSITY OF PETROLEUM & MINERALS
DHAHRAN- 31261, SAUDI ARABIA
DEANSHIP OF GRADUATE STUDIES

This thesis, written by EMAD ABDULSHAFI ALKHAZRAJI under the direction of his thesis advisor and approved by his thesis committee, has been presented and accepted by the Dean of Graduate Studies, in partial fulfillment of the requirements for the degree of MASTER OF SCIENCE IN ELECTRICAL ENGINEERING.

Dr. Ali Al-Shaikhi
Department Chairman

Dr. Mohammed Zahed
Moustafa Khan
(Advisor)

Dr. Salam A. Zummo
Dean of Graduate Studies

Dr. Husain Al-Jamid
(Member)

16/5/16

Date

Dr. Samir Alghadhban
(Member)

Dedicated to

my beloved Parents, Dr. Abdulshafi Alkhazraji and Eng. Hanaa Amer

my sister, Dr. Mai Alkhazraji

my little brothers, Omar and Ali Alkhazraji.

ACKNOWLEDGEMENTS

First and foremost, all praises and glory are for Allah the most merciful, the most graceful. Prayers and blessings upon the last Prophet, peace be upon him, his family and his companions.

Words cannot begin to suffice my gratitude for my parents for their everlasting love and support in every single possible way. My gratitude extends to my beloved little brothers and sister of being the best life companions one can wish for. May Allah reward them all and protect them from all harm and evil.

I offer my heartfelt appreciation to my advisor Dr. Mohammed Zahed Moustafa Khan for being the ideal mentor one can wish for. He never ceases to overwhelm me with his vast knowledge, good manners and patience. I am eternally indebted to him for giving me the opportunity to pursue my research in the field I am passionate about when all doors seemed closed. I hope this only marks the beginning of our professional relationship.

I sincerely offer my gratitude to the person who is the main reason I am in this field in the first place, Dr. Husain Al-Jamid, who taught and inspired me in more ways than he even realizes.

I also present my heartfelt appreciation to Dr. Samir Alghadhban who taught me all I know about digital communications while overwhelming me with his kind heart and great knowledge.

In addition, I offer my sincere thanks to Dr. Mohammad Alsunaidi with whom I started this journey and due to very unfortunate circumstances was not able to continue.

I also thank Dr. Khurram Qureshi for his generosity and for allowing us to use his optical fibers laboratory to carry out our experimentations.

I also extend my thanks to the our collaborators at the photonics laboratory in King Abdullah University of Science and Technology (KAUST) headed by Dr. Boon Ooi and including Dr. TienKee Ng, Chao Shen, and Bilal Janjua for fabricating the laser specimens, their kind hospitality, and for giving us the opportunity to use their lab in device level characterization.

I would like also to extend my thanks to our collaborators in Prince Sultan Advanced Technology Research Institute (PSATRI) and Radio Frequency and Photonics for the e-Society (RFTONICS) at King Saud University (KSU) especially Dr. Habib Fathallah, Dr. Amr Ragheb and Saleh Chebaane for giving us the opportunity to perform our system level analysis in their cutting edge one-of-a-kind optical communications laboratory.

I finally thank all my relatives, friends and colleagues for their love and support, for the laughs, and for their continuous prayers for me.

TABLE OF CONTENTS

LIST OF TABLES

LIST OF FIGURES

LIST OF ABBREVIATIONS

AFM	:	Atomic Force Microscopy
ASE	:	Amplified Spontaneous Emission
AWG	:	Array Waveguide Grating
AWGN	:	Additive White Gaussian Noise
BER	:	Bit Error Rate
BTB	:	Back-to-Back
CW	:	Continuous Wave
DCA	:	Digital Communication Analyzer
DCD	:	Duty Cycle Distortion
DOS	:	Density of States
DQPSK	:	Differential quaternary Phase-Shift Keying
EDFA	:	Erbium Doped Fiber Amplifier

EL : Electroluminescence

FP : Fabry-Perot

FSO : Free Space Optics

ISI : Inter-symbol Interference

ITU : International Telecommunications Union

LED : Light Emitting Diode

LPE : Liquid Phase Epitaxy

MBE : Molecular Beam Epitaxy

MML : Mode-Locked Laser

MOCVD : Metal-Organic Chemical Vapor Deposition

MZM : Mach-Zehnder Modulator

NRZ : Non-Return To Zero

OOK : On-Off-Keying

OSA : Optical Spectrum Analyzer

OTF	:	Optical Tunable Filter
PDF	:	Probability Density Function
PRBS	:	Pseudo-Random Bit Sequence
QDash	:	Quantum Dash
QDot	:	Quantum Dot
QWell	:	Quantum Well
RF	:	Radio Frequency
SHF	:	Super High Frequency
SNR	:	Signal to Noise Ratio
SPW	:	Short Pulse Width
TEM	:	Transmission Electron Microscopy
TOF	:	Tunable Optical Filter
VOA	:	Variable Optical Attenuator
WDM	:	Wavelength Division Multiplexing

ABSTRACT

Full Name : Emad Abdulshafi Moawad Moustafa Alkhazraji

Thesis Title : Broadband Semiconductor Laser as a Source in Optical Communication Systems

Major Field : Electrical Engineering

Date of Degree: May 2016

Quantum dash based laser diodes have attracted the focus of study and research in the very recent years due to what they possess of myriad advantages that make them ideal for several applications. Among these advantages is their ultra-broad band emission as a result of the inherent inhomogeneous nature of the growth process of quantum dashes. The main objective of this thesis is to investigate a novel multi-stacked chirped InAs/InAlGaAs/Inp quantum dash-in-well laser structure that introduces an extra layer of inhomogeneity due to the dissimilar sizes of the different dash stacks. The investigation of this laser is carried out at two levels; device level and system level.

In device level, fundamental laser diode characterization experiments are performed to extract its principle parameters in addition to the bandwidth of its spectral emission under short pulse width operation mode. We then follow by expanding the *investigation scope of operation modes to higher order duty cycles pulsed and continuous wave operation modes and compare their effect on the spectra profile and the laser principle parameters. Junction temperature of the laser diode plays a vital role in different quantum phenomena that affect carrier distribution processes within the active medium. Hence, we conclude the device level characterization by performing a parametric study on the temperature dependent lasing spectral profiles at different geometrical configurations, current injections, and temperature values.*

Thereafter, the found results are used to optimize different ambient and operation parameters that achieved successful implementation of the quantum dash laser in an optical communication system in On-Off-Keying modulation. Results show that the maximum achieved data rate is 20 Gb/s while error-free communication was achieved at 10 Gb/s. Moreover, a 10 km optical fiber link was used in successful transmission while the maximum fiber length over which successful transmission can be achieved was estimated to be 35 km while error-free transmission can be achieved over a maximum fiber link length that was estimated to be 20 km at 5 Gb/s.

ملخص الرسالة

الاسم الكامل: عماد عبد الشافي معوض مصطفى الخزرجي.

عنوان الرسالة: الليزر شبه الموصل ذو نطاق الإشعاع العريض كمصدر في أنظمة الاتصالات الضوئية.

التخصص: الهندسة الكهربائية.

تاريخ الدرجة العلمية: مايو ٢٠١٦.

ديودات الليزر المبنية على الخطوط الكمية جذبت ولا تزال تجذب انتباه العديد من الأبحاث والدراسات في السنوات الأخيرة لكونها تمتلك العديد من المميزات التي تجعلها مثالية في العديد من التطبيقات. أحد هذه التطبيقات هو الإشعاع فائق العرض كنتيجة طبيعية للاتجانس الذي تتصف به عملية تكوين الخطوط الكمية. الهدف الرئيسي من هذه الرسالة هو دراسة الليزر المكون من In/InAlGaAs/InP الذي يعتمد على تركيب خط-كمي-في بئر المعدل متعدد الطبقات الذي ينتج درجة إضافية من اللاتجانس كنتيجة للأحجام الغير متساوية في الطبقات المختلفة. هذه الدراسة مبنية على مستويين; مستوى الجهاز ومستوى النظام.

على مستوى الجهاز، أجريت تجارب مبدئية خاصة بديودات الليزر من أجل قياس خواص الليزر الأساسية بالإضافة إلى عرض الإشعاع الطيفي تحت عمليات تشغيل نبضية قصيرة. من ثم قمنا بتوسيع منظور الاختبار ليشمل عمليات نبضات تشغيل أطول بالإضافة إلى عمليات التشغيل المستمرة وقارنا تأثيرهم على الإشعاع الطيفي بالإضافة إلى خواص الليزر الأساسية. درجة الحرارة داخل الوسط الفعال الخاص الليزر تلعب دوراً حيوياً في العديد من الظواهر الكمية التي تؤثر على توزيع نواقل الشحنات داخل الوسط الفعال. من أجل ذلك اختتمنا دراسة مستوى الجهاز بالقيام بدراسة العوامل المرتبطة بدرجة الحرارة والأبعاد الهندسية والتيار الكهربائي المضخ لليزر على الإشعاع الطيفي الخاص بالليزر.

هذه النتائج استخدمت بعد ذلك من أجل تحسين العوامل التشغيلية والبيئية المختلفة التي حققت تطبيقاً ناجحاً لليزر الخطي الكمي في نظام اتصالات ضوئي يعتمد على تضمين الإيقاف والتشغيل (On-Off-Keying). تشير النتائج إلى أن المعدل الأقصى الذي تمكنا من تحقيقه بنجاح هو ٢٠ جيجابت في الثانية فيما أن معدل نقل البينات الاقصى الخالي من الأخطاء هو ١٠ جيجابت في الثانية. بعد ذلك تم القيام بعملية نقل البيانات بنجاح من خلال ليف ضوئي طوله ١٠ كم فيما أن طول الليف الضوئي الاقصى الذي يمكن أن تتم عليه نقل عملية الاتصال بنجاح مقدر ب٣٥ كم والطول الذي يضمن الخلو من الأخطاء مقدر ب٢٠ كم على معدل ٥ جيجابت في الثانية.

CHAPTER 1

INTRODUCTION

1.1 Background

1.1.1 Historical Overview

Although modern optical communication systems have come later to be employed, man has been using visual communication techniques, such as smoke, lighthouses, and fire for millennia. By using Morse codes in communications between sailors and lighthouses, semaphore telegraphy greatly resembles modern optical communication systems. This technique was first schematically introduced by Robert Hook in 1684 [1]. As modern communication systems developed, such primitive techniques were fast replaced by more modern systems that outclassed them in all aspects.

However, as communication systems evolved, the need for a better solution, compared to the bandwidth-exhausted copper-wired transmission lines, has become more pressing. At the same time, light-wave communication systems showed a great potential in achieving significantly higher data transmission rates, higher channel capacities [2], and lower attenuation rates in long-haul communication systems, all while attaining a lower cost [3].

The first attempt in trapping light inside a dielectric was in 1841 when young Jean-Daniel Colladon used total internal reflection to guide light within a stream of water inside a hole-filled tank [4]. However, G. A. Hockman's and Charles Kao's are considered the first to utilize a glass fiber to guide light for data transmission over long distances. [5, 6], but the material problem stated in their paper was yet to be solved until 1970 when the low-loss glass fabricated by Croning [7] achieved the 20 dB/km loss goal that was set in [5].

Meanwhile, starting in the late 1950s, the development race in realizing a semiconductor laser diode that operates on the theoretical foundations that were set by Albert Einstein in 1917 had begun [8]. In large, much like any communication system, optical communication systems can be divided into three main elements, namely a transmitter, a channel and a receiver, as shown in Figure 1.1 [9].

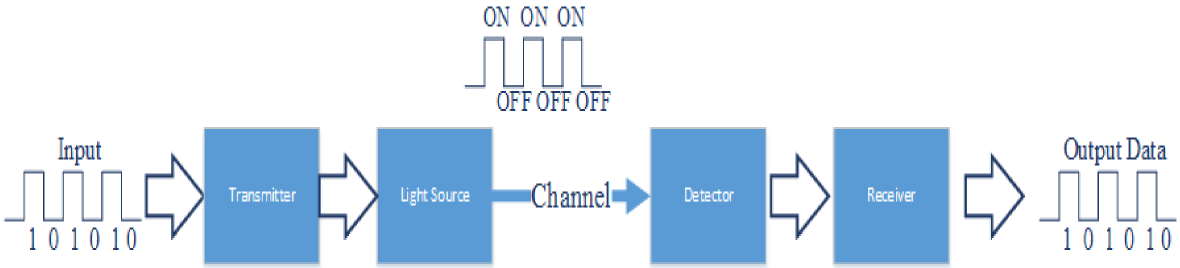

Figure 1.1: Illustration of elements of an optical communication system.

At this point, while photon-over-fiber links significantly improved the channel capacity of the communication system, the need for an appropriate and efficient light source to be used over this channel had risen and was met when Robert Hall introduced the first laser diode in 1962 that emitted at a wavelength of 850 nm in the near infra-red, which later became a revolution in the telecommunication field [10, 11].

1.1.2 Quantum Confinement

In quantum theory, the quantum confinement effect is one of the most fundamental topics that has a large impact on semiconductor devices, particularly optoelectronic devices such as light sources and detectors. The generation (and absorption) of photons is governed by the excitation and recombination of quasi-particles in the crystal lattice. These quasi-particles are electrons and holes.

The potential seen by these quasiparticles can be approximated by the basic quantum-wall problem in one dimension, shown in Figure 1.2, where their wave-like nature is governed by Schrödinger's wave equation whose time-independent one-dimensional form is given by [12]:

$$\frac{\partial^2}{\partial x^2}\psi(x) + \frac{2m}{\hbar}[E_o - U(x)]\psi(x) = 0 \tag{1.1}$$

where

- $\hbar = \frac{h}{2\pi}$ is the reduced Planck's constant which equals $1.0545718\times10^{⊠34}$ J.s.
- ψ is the time-independent wave function.
- U is the electrical potential function experienced by the particle.
- E_o is the total energy of the particle.
- m is the effective mass of the particle.

By applying (1.1) into the quantum-well configuration shown in Figure 1.2, the associated solutions, *i.e.* eigen energies, to this differential equation are given by [12]:

$$E_n = n^2\left(\frac{\pi^2\hbar^2}{2mL^2}\right) \tag{1.2}$$

where,

E_n is the n^{th} Eigen energy.

L is the width of the quantum-well (the confined region).

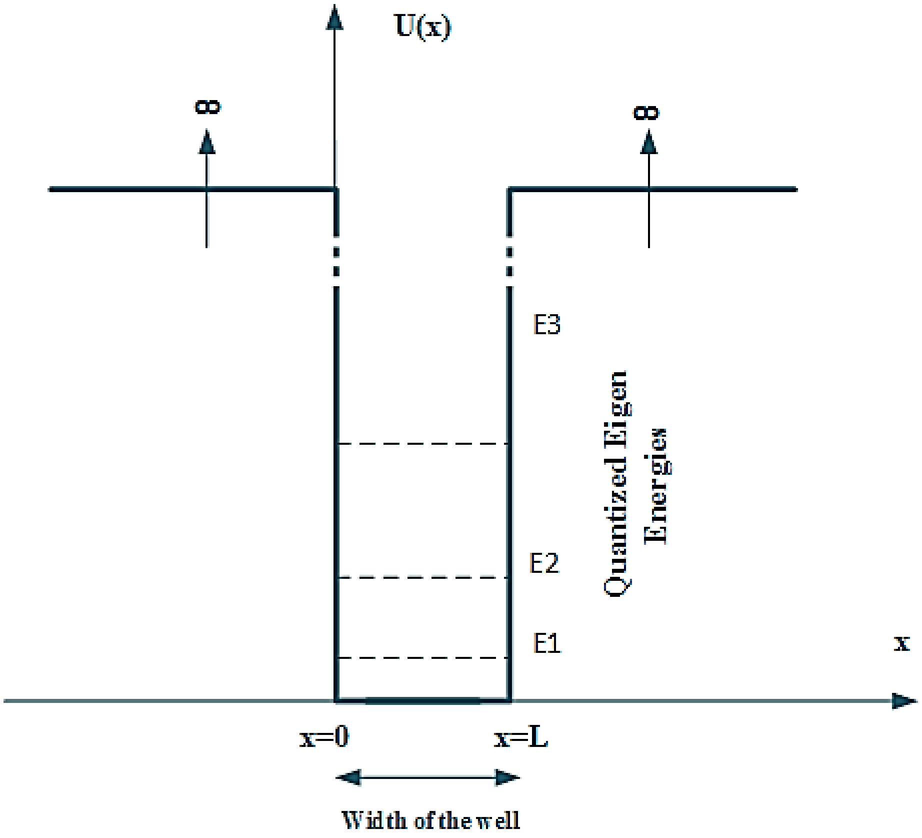

Figure 1.2: A potential configuration representing a one-dimensional quantum well problem with the associated discretized eigen energies.

Hence, these eigen energies (eigen states) are quantized as square-multiples of the quantity $\left(\frac{\pi^2\hbar^2}{2mL^2}\right)$ where L (well thickness) can be used to control how far these eigen energies are from each other.

Quantum confinement effects appear when the geometrical dimensions of the device are of the same order of magnitude as the DeBroglie wavelength of the electrons, which is of the order of tens of nanometers. A one-dimensional-confinement based structure is called a quantum well (QWell) and can be modeled, in terms of energy, by the one-dimensional quantum wall problem shown in Figure 1.2 alongside the eigen energies associated with the solutions of the Schrödinger equation that predicts the allowed energy levels electrons can inhabit in that configuration [12].

Figure 1.3 shows dimensionally different confinement structures alongside their density of states (DOS). The density of states is a significant parameter in semiconductors that indicates the number of available states (energies) that electrons and holes can occupy. Introducing quantum confinement in different dimensions introduces different quantum structures. While one-dimensional confinement results in quantum wells, two-dimensional confined structures are known as quantum wires whereas three-dimensional confinement results in quantum dots (QDots). The more a structure is confined, the more discretized (quantized) the density of states gets. For instance, the parabolic DOS profile of a bulk structure reduces to a stair case (for one-dimensional confinement) to a quasi-zero-dimensional DOS (for two-dimensional confinement) to a zero-dimensional DOS (for three-dimensional confinement). These features of quantum confinement, significantly improve the number of electron-hole pair recombinations that results in photons of more discretized wavelengths. In addition to a narrower emission, a highly confined structure provides more controllability over the emission. The emission wavelength depends solely on the effective bandgap after quantization which is depicted by the geometrical dimensions of the structure and how confined it is [12, 13].

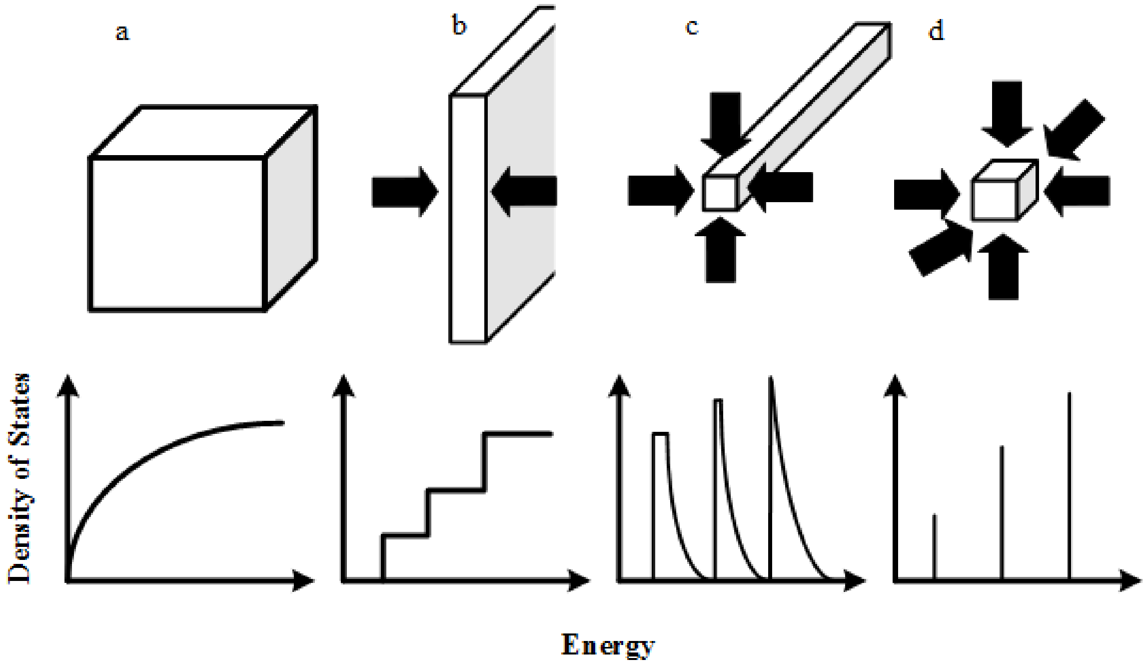

Figure 1.3: Different quantum confinements. (a) Zero-dimensional confinement (bulk material). (b) One-dimensional confinement (quantum well). (c) Two-dimensional confinement (quantum wire). (d) Three-dimensional confinement (quantum dot), with their respective density of states.

1.1.3 Optical Communication

In the following years, for the myriad advantages and properties that optical communication systems promised, telecommunication industries had focused on this technology in research and development. Ever since, fiber optics grew to become the backbone of data transmission of all different shapes and configurations

[14]. Today, optical communication takes different forms, free space optical communication (FSO) and optical fibers [15]. The range of wavelengths used in optical communications is based on the performance of the emitted light inside the traditional silica-based optical fibers and is divided into three main windows (in the near infra-red region) as follows:

- The first window (around 850 nm) which was initially used because it corresponds to the emission wavelength from the first GaAs/AlGaAs III-V material based light emitting diodes (LED) and Laser diodes.
- The second telecom window (around 1300 nm) where the total dispersion in single mode silica-based optical fibers is minimum.
- The third telecom window (around 1550 nm) where the attenuation in silica-based optical fibers is minimum, as shown in Figure 1.4(b).

Moreover, the wavelengths for efficient optical communications (centered around 1300 nm and 1550 nm) are also divided into windows or bands as shown in Figure 1.4(a) [16], which have been standardized by the International Telecommunication Union (ITU).

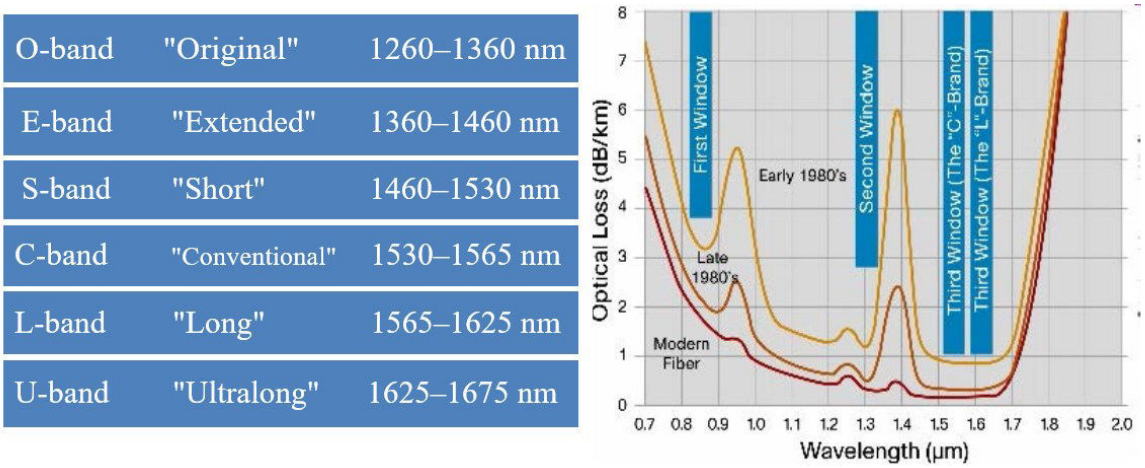

O-band	"Original"	1260–1360 nm
E-band	"Extended"	1360–1460 nm
S-band	"Short"	1460–1530 nm
C-band	"Conventional"	1530–1565 nm
L-band	"Long"	1565–1625 nm
U-band	"Ultralong"	1625–1675 nm

(a) (b)

Figure 1.4: (a) Optical communication working bands. (b) Associated optical losses in silica-based fibers as a function of wavelength [17].

The rapidly increasing demand for high-speed telecommunications and higher data transmission rates is ever growing as reliable fast telecommunication has become one of our daily life necessities [18]. Moreover, the call for energy efficiency in all aspects of research and development has become louder than ever as a direct route to environment preservation and economic prosperity. In order to meet such demands, research has been seeking solutions to a better utilization of the communication system elements.

Among the widely used techniques for that purpose is wavelength division multiplexing (WDM, coarse WDM, and dense WDM) where a single shared medium can be used to transmit multiple channels, simultaneously. Theoretically, one single-mode fiber should be able to carry tens of terahertz over all the telecom sub-bands (1.2 μm – 1.6 μm). However, realizing such huge bandwidth has yet to be achieved because of the practical limitations of different elements such as the optical sources, amplifiers, and detectors [19]. A typical WDM system is illustrated in Figure 1.5 where each of the multiplexed N channels is carried by a single wavelength, which is generated by a single source. Thus, for N channels, N sources are required.

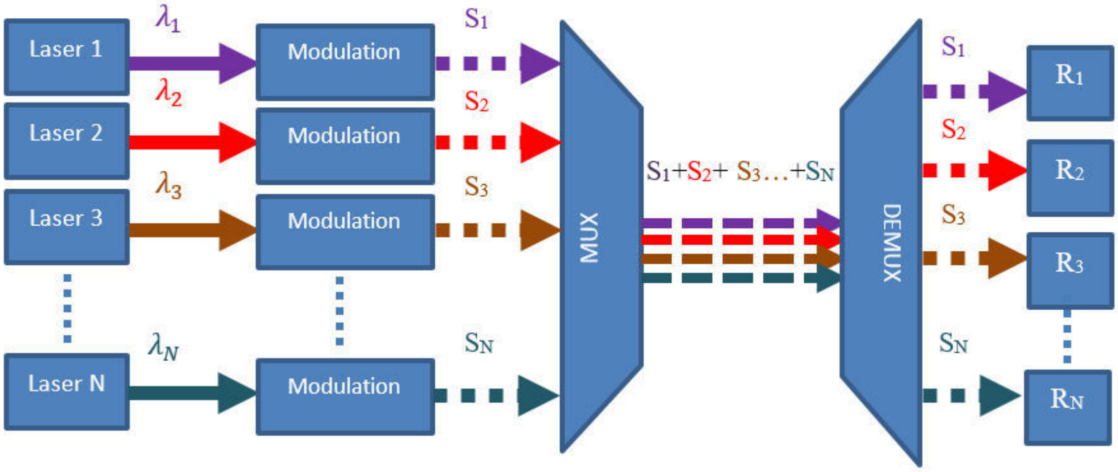

Figure 1.5: A typical WDM optical communication system where N laser sources are used in order to provide the N wavelength pulses (sub-carriers) on which the N information signals are transmitted over a single channel simultaneously.

A broadband emitter, on the other hand, possesses the potential to reduce the required number of laser diodes in the WDM system, significantly. However, broadband emitters in the form of light emitting diodes (LEDs) suffer from small power-bandwidth product which limits their usage in communications. Very recently, a novel broadband semiconductor lasers with large power-bandwidth product has been reported which has the potential to be used as a source in a WDM systems. As shown in Figure 1.6, a single broadband laser can replace the

N laser diodes, given that its emission is wide enough. This results in significant reduction of the cost and the total power consumption of the transmitter.

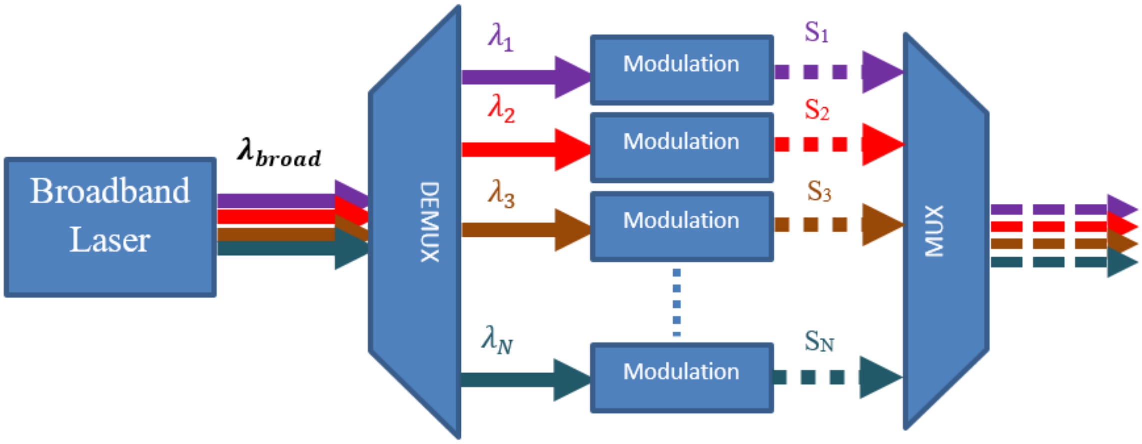

Figure 1.6: A reduced transmitter using a single demultiplexed broadband laser as an optical source instead of N narrow-emission laser diodes, in an optical WDM system.

Traditional quantum-well structures laser diodes are characterized by their narrowband emission and are already deployed in optical communications, serving as sources in WDM system. On the other hand, dimensionally-higher confined laser structures such as self-assembled quantum dots and quantum dashes can achieve broader band emissions by the virtue of their inherent inhomogeneity [20]. Exploiting this feature of quantum dashes and quantum dots have resulted in the demonstration of ultra-broadband lasers, a potential candidate used in optical WDM systems.

A Quantum dash (QDash) is a quantum confined nanostructure that resembles a stretched quantum dot due to a high lattice mismatch strain during the selfassembly growth process. As a result, QDashes share the same average cross-sectional area of quantum dots while ranging from tens to hundreds of nanometers of their length [20].

1.2 Research Contribution

In this work, we investigate a novel chirped structure of quantum dash lasers that show a high degree of inhomogeneity and, consequently, an ultra-broad emission. We investigate the device level characteristics and shed light on the physics involved during the emission process of this novel structure under different parameters and configurations. Nonetheless, the main contribution of this work is to build the knowledge foundation upon which, different system level applications can be built while demonstrating the employment of these structures in an ON-OFF-KEYING-based optical communication system as one of said applications.

1.3 Thesis Organization

This thesis is organized as follows:

Chapter 1	Contains an introduction and a historical overview covering basic concepts of quantum confinement.
Chapter 2	contains an in-depth literature review covering developments in different quantum confined structures, *i.e.* quantum well, dots, and

dashes. In addition, the chapter covers recent applications of said structures in optical communication systems.

Chapter 3 contains a rigorous investigation of the device level characterization of chirped quantum dash based laser diodes. Moreover, the chapter explores the effect of varying different geometrical parameters on the characteristics of the laser.

Chapter 4 explores different modes of operation of the Qdash laser including different pulsed duty cycles and continuous wave emission and how each affects the performance of the laser.

Chapter 5 investigates the junction temperature associated with higher duty cycle operations and high current injections and its effect on the leasing spectral and performance characteristics.

Chapter 6 discusses the employment of the quantum dash laser in optical communication systems after optimizing different ambient and operation parameters according to the acquired knowledge from the previous chapters. It then examines the limit of using the quantum dash laser in terms of the bit data rate and fiber link length.

Chapter 7 summarizes concludes this thesis, and discusses possible future extension of this work.

CHAPTER 2

LITERATURE REVIEW

2.1 Quantum Well Structures

The previously mentioned first laser diode that Hall had introduced was a regular GaAs p-n homo-junction that emitted at 850 nm. However, it took only one year after that for H. Kroemer to introduce the concept of hetero-junction structures [21]. That concept was later realized in 1967 when IBM grew the first double hetero-structured laser using liquid phase epitaxy (LPE) [22] with a layer of GaAs sandwiched between two layers of AlGaAs whose bandgap is larger than that of GaAs resulting in a relatively more confined active region compared to that of regular p-n homo-junctions. Figure 2.1 shows a comparison between homo-junctions and double hetero-junctions in terms of their structures and energy-band diagrams.

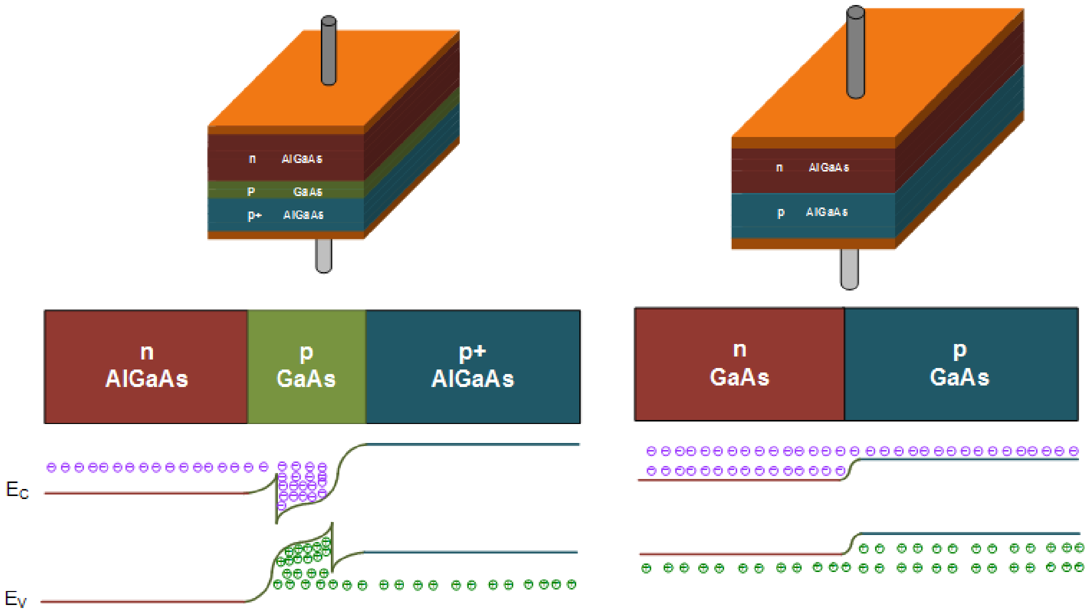

Figure 2.1. Comparison between the energy band diagrams of homo-structured p-n junctions (right) and double hetero-structured junctions (left).

The figure clearly shows that the carriers (electrons and holes) are more confined inside the active region in the case of hetero-structures. The radiative recombination of electron-hole pairs occur inside the active region of the structure which makes their confinement in that region extremely desirable. In 1972, P. S. Zory, Jr. of BELL labs suggested an analogy between the confinement of photons in a slab waveguide and the confinement of electrons inside the potential walls that appear in hetero-structures where the discrete guidance modes of the slab would be analogous to discrete state levels rather than energy bands given that the electrons are potentially confined enough [23].

Following these steps, quantum wells were introduced as double hetero-structures where the thickness of the active region is less than the De Broglie wavelength of the electrons. However, at that time, the traditionally used LPE for growing LEDs and bulk lasers was only capable of producing layers of thicknesses greater than 200 nm which made it obsolete for growing quantum-well lasers. Due to that reason, the newly developed molecular beam epitaxy (MBE) in 1968 gained a great deal of popularity because it ability to be used to grow quantum-well layers [24].

Quantum-well structures showed promising properties that made them replace bulk laser diodes ever since. Most of the advantages are due to the dramatic increase in population inversion in the active region resulting from improved carrier confinement. Consequently, the lasing phenomenon occurs earlier at a lower threshold current with less variance of the refractive index of the active medium. Moreover, a significant advantage of this configuration is that by varying the thickness of the well, we can control the eigen energies of the quantum well, which ultimately leads to more controllability of the emission wavelength while keeping the material composition constant [25,26]. However, the output optical power of these lasers were very low compared to bulk lasers due to the quicker gain saturation as a result of the limited volume of the active medium. The introduction of the multiple-quantum-well structure in [27], [28], and [29] (1976, 1978, and 1979, respectively) solved this issue, where an aggregate of single quantum-wells are coupled to lase together, at the expense of higher threshold current values as more layers are used.

Having the laser materials, their respective compositions, and the thickness of the active region layer as factors to control the emission of quantum-well lasers, researchers have been introducing different configurations in order to cover a wide range of wavelengths. Whereas the first semi-conductor GaAs lasers emitted around 850 nm, in the following couple of decades, research groups around the world had been proposing different configurations of different materials and compositions until a wide wavelength range from ultra-violet to visible to infra-red regions have become achievable via quantum-well-structured lasers [23]. Nevertheless, for communication applications, among the possible emission wavelengths, the most relevant ones are those that lie inside the second and third telecommunication windows which lie around 1.3 µm and 1.55 µm, respectively.

Later $In_{1-x}Ga_xAs_yP_{1-y}$ have been commonly used, up until today, all to grow quantum-well laser diodes that emit in the second and the third telecom windows via the newly emerging metal-organic chemical vapor deposition (MOCVD) epitaxial technique. Depending on the composition of each of the quaternary components, different energy bandgaps, and hence emission wavelengths, can be achieved. Figure 2.2 shows the different possible compositions alongside the resulting effective energy bandgap. The corners of the polygon show the binary possibilities, namely, GaP, GaAs, InP, and InAs. On the other hand, the solid lines of the polygon show the ternary configurations, i.e. InGaAs, InAsP, GaAsP, and, InGaP. Moreover, points inside the polygon represent the quaternary $In_{1-x}Ga_xAs_yP_{1-y}$ materials. The composition of the grown materials must be in such a way that their bandgap energy is 0.9537 eV and 0.7999 eV in order to lase at 1.3 µm as proposed in [30-33] and 1.55 µm as done in [34-36], respectively. Such compositions are achieved by moving along the horizontal blue and red dotted lines in the figure, respectively.

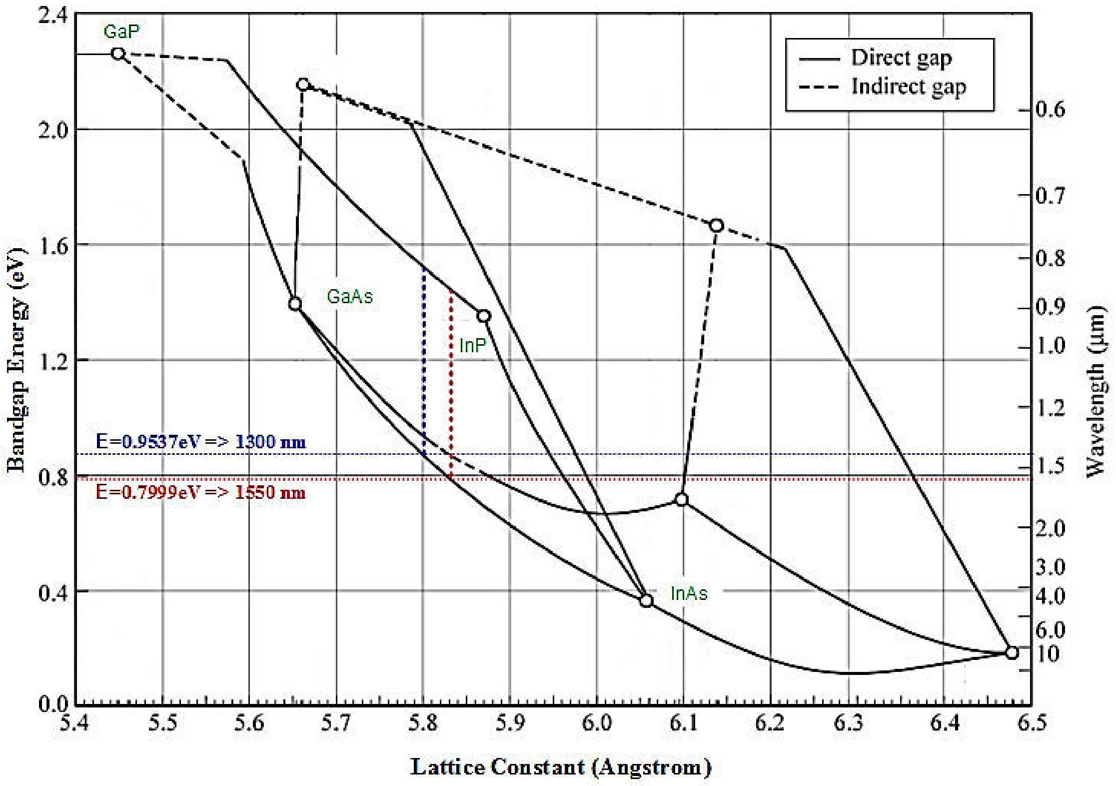

Figure 2.2: Quaternary configurations used in semiconductor laser materials in the second and third telecom windows [26].

The traditional epitaxial growth technique used in nanotechnology and semiconductor devices is done through the deposition of crystalline over-layers over a substrate in a layer-by-layer fashion where each layer is lattice-matched with the subsequent layers. In Figure 2.2, any vertical line indicates composition of identical lattice constants. This type of growth is used in fabricating thin two-dimensional layers, such as hetero-structures and QWells, where the lattice constants of the substrate and the subsequent over-layers are required to have a minimum strain-mismatch in order to reduce defects and dislocations that have detrimental effects on the mobility and electron-hole pair recombination rates of the grown device [37]. This technique results in uniform and highly crystalline two-dimensional layers as seen in Figure 2.3 (a).

2.2 Quantum Dots and Quantum Dashes

Recently, a new growth technique was introduced called Stranski–Krastanov or self-assembled growth. In this technique, a deliberate lattice mismatch is introduced in the epitaxial growth where the first layer will be a two-dimensional layer similar to that of Figure 2.3 (a), called a barrier layer. After that, when enough material is deposited in two dimensional form, due to the resulting strain caused by the lattice mismatch, three-dimensional pyramid shaped islands will start to emerge, as shown in Figure 2.3 (b), along with the formation of a thin two dimensional layer underneath them, known as the wetting layer (thickness in the range of 1 – 2 nm).

These three dimensional islands are the highly confined quantum dots. This strain-based growth is a random process resulting in a random formation of the QDots in terms of their locations, inter-distances and sizes that range between 1-20 nm [38]. Hence, the inhomogeneous nature of self-assembled QDots as a result of this random process affects the emitted photon energy, which depends on the quantized energies governed by the three-dimensional confinement (function of the geometrical configuration of the QDots) [37].

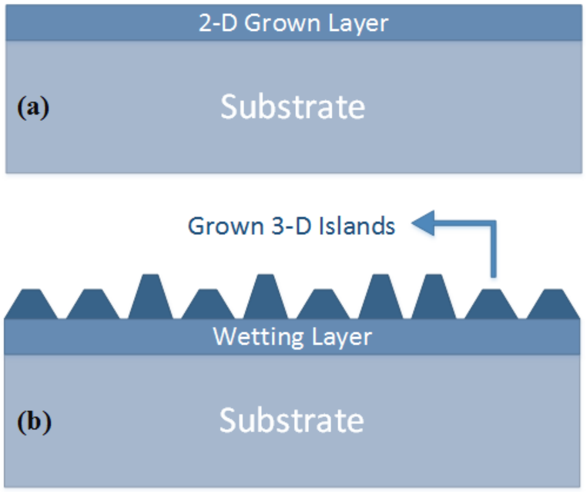

Figure 2.3: Two types of epitaxial grown layers: (a) Traditional 2D epitaxial layers. (b) 3D grown QDots.

When the lattice mismatch strain is not equivalent in all directions for QDots to emerge, the grown islands are prolonged albeit resembling the QDots in their cross-sectional areas. These types of structures are termed as quantum dashes that exhibit an inhomogeneous nature that might sometimes even exceed that of QDots. Figure 2.4 (a) and (b) show Atomic Force Microscopic (AFM) images of InAs

QDots and QDashes, respectively [39], grown on InP substrate, which reveal that QDashes are a mix of QDot-like and quantum wire-like structures.

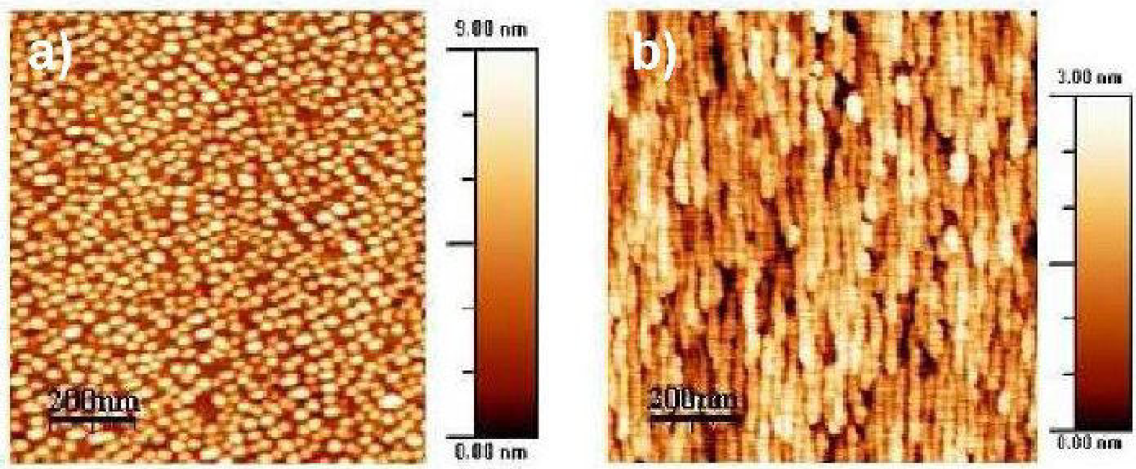

Figure 2.4: AFM images of InAs grown (a) QDots and (b) QDashes on InP substrate [39].

Nonetheless, as the demand for more emission efficiency and more compact designs emerged, extra dimensionally confined structures, i.e. self-assembled quantum dots and quantum dashes provide promising substitutes. Indeed, the introduced InAs/GaAs self-assembled QDots in [40] and [41] displayed excellent performance while emitting at ~1.3 µm. Besides showing tremendous improvement in the laser performances characteristics, another noteworthy progress QDots based lasers showed over the QWell counterpart is their extremely wideband emission of a 3dB bandwidth that reached ~ 75 nm at 1.24 µm. This was achieved by exploiting the inherent inhomogeneous nature of QDots as reported in [42] together with an intentional inhomogeneity (usually known as chirping) introduced in the form of varying the thickness of the monolayer deposition in the growth of each QDot stack. On the other hand, intentional inhomogeneity in a QWell laser was introduced by employing an asymmetrical multiple well structure, *i.e.* wells of different thickness. This device had a maximum bandwidth of ~30 nm as reported in [43]. As a result, InAs/GaAs QDot-based lasers have started to take over the commercial and industrial scene for 1.3 µm applications. However, for telecommunication applications, the GaAs based QDots are still unable to cover the C, L, U bands (1.5 µm -2.0 µm) and thus InAs/InP QDots/QDashes have been a research focus for emission in these bands [44]. In [45], InAs/InP QDot (grown over a QWell layer of InGaAs) based lasers were reported for the first time initially emitting at ~1.9 µm at cryogenic-temperature of 77 K, and emission at room temperatures was reported later in [46]. Later, in [47], Caroff et al. demonstrated a QDot-based laser that emitted at 1.59 µm at room temperature, (see Figure 2.5), using InAs/InP Qdots with a quantum dot density of 1.1×10^{11} /cm^2. The reported transparency threshold current density was a low 68 kA/cm^2.

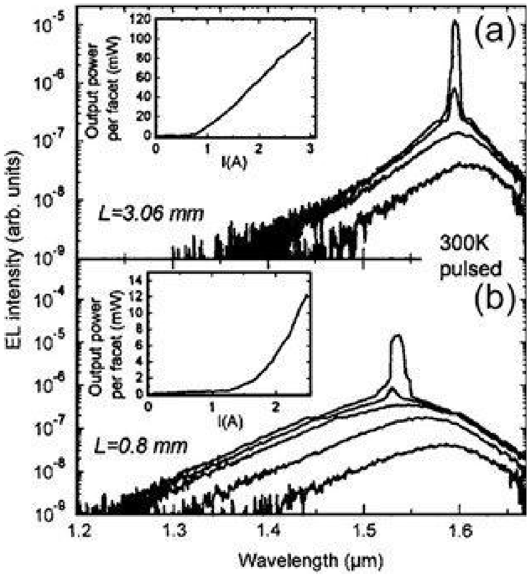

Figure 2.5: Room temperature lasing spectra of the demonstrated InAs/InP QDot laser at two different cavity lengths, namely 0.8 mm and 3.06 mm [47].

Shortly after, different researchers and groups reported different improvements based on InAs/InGaAsP QDots. For instance, a high mode gain of 13/cm was achieved in [48] using a single layer of InAs/InP. In [49], a dot density of $1.3\times10^{11}/\text{cm}^2$, which was the largest to be achieved using these materials, while the internal loss was reduced to 6/cm.

InGaAlAs is another material that is used as a base material over InP substrates in QDots growth. The first instance where this material was used was in [50] where emission at a center wavelength of 1.63 µm was demonstrated while having an internal loss of 3.6/cm which is considered the lowest internal loss value of InAs/InP based QDot lasers. Six years later, by taking advantage of the Aluminum atoms in the InGaAlAs substrate and using the strain compensation technique, Akahane et al. [51] reported emission at 1.58 µm out of a multi-stack of

InAs/InGaAlAs with a threshold current density of 2.7 kA/cm^2. A lower value of 1.72 kA/cm^2 was reported later in [52] which is the lowest reported threshold current density for any InAs/InP grown QDot laser. Later, it was demonstrated in [53] that the emission wavelength showed a tunability range from 1.47 µm to 1.70 µm by controlling the amount of deposited InAs, as illustrated by Figure 2.6. Three different emission peaks were demonstrated using the same materials albeit with different compositions.

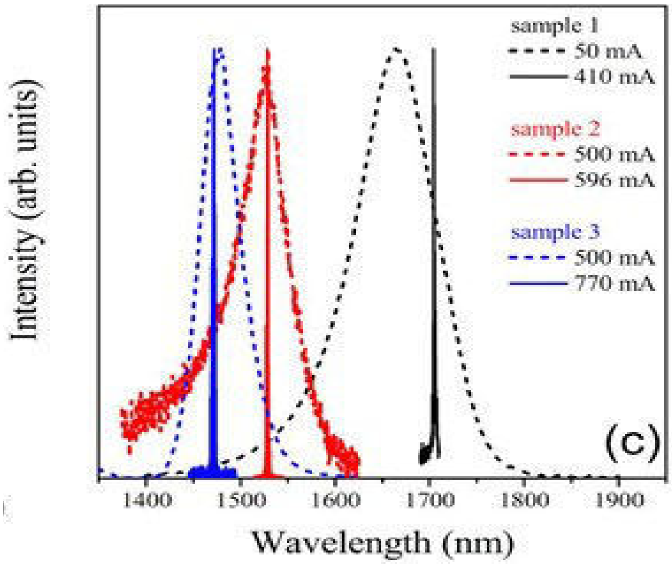

Figure 2.6: Electroluminescence (EL) and lasing spectra of three different InAs/InGaAlAs occurring at 3 different peaks through controlling the composition of the deposited InAs [53].

The InAs/InP QDot laser research, summarized in the above few paragraphs, in general, employed assisted growth techniques (to alter the strain distribution) to achieve InAs QDots on InP substrate because a typical growth usually results in a highly inhomogeneous elongated QDash structure. However, these structures were also exploited to demonstrate semiconductor lasers in the vital C – L – U communication bands. In the following, some of the laser achievements in the QDash domain are summarized.

QDash lasers were first introduced in [55] as InAs QDashes over a substrate of InP which emitted around 1.60 µm with a slight red shift as more layers of InAs/InGaAlAs were introduced. The reported threshold current density was 410 A/cm^2 while the internal loss and internal quantum efficiency were ~10/cm and 60% respectively. This work encouraged researchers and groups to work on this quantum confined nanostructure based semiconductor lasers.

Not so long afterwards, Schwertberger and his group [56] reported a great tunability range of their QDash laser based on the same materials whose emission peak ranged from 1.54 to 1.78 µm by the virtue of changing the thickness of the deposited InAs layers while keeping the threshold current at the low value of 900 A/cm^2.

As the quality of the growth process improved, better results had been reported. In [57], Rotter and his group were able to expand on the concept of the tunability shown in [56] to achieve the longest reported emission wavelength that reached 2.03 µm using a stack of 5 layers of InAs Dashes embedded in an InGaAs quantum well.

In [58], chirping the active region was introduced where different layers of QDashes were deposited at different stages by varying barrier layer thicknesses with the purpose of increasing the inhomogeneous broadening of the self-assembled QDashes and to achieve broad gain materials for semiconductor optical amplifier and broadband laser applications. Different research works have followed the chirped active region technique such as [59] and [60] with internal loss values of 4.6/cm and 11/cm, respectively, and internal quantum efficiencies of 60% and 85%, respectively, while lasing at 1.53 µm and 1.62 µm, respectively.

Due to their broadband emission, QDots and QDashes are great contenders that can be used in energy efficient optical telecommunication. Another potential application of broadband lasers is in producing extremely short light pulses in the order of picoseconds and femtoseconds which can be done through mode-locking where the emitted short pulses are phase-locked depending on the round-trip taken by photons inside the laser cavity. In QDot and QDash lasers, mode-locking can be achieved via an external signal, which in this case is called active mode-locking, or can be achieved passively without the need to an external source which makes it more favorable due to its compact nature and lower cost requirements [61].

One of the simplest techniques used in passive mode-locking is to divide the device into two sections. The first section is to be forwardly-biased acting as the light emitting laser (amplifier section) while the second section is reversely biased acting as a saturable absorber that can be used for control and synchronization through the forward bias of that section [61].

2.3 Recent Applications in Communication Systems

The use of QDash lasers in optical communication applications is still living its infancy years. At the end of 2009, the CNRS Laboratory for Photonics and Nanostructures in France first used a mode-locked laser (MLL) based on QDash active region. The MLL was emitting at 1.55 µm as a source for WDM spacing of 100 GHz, which is standardized by the International Telecommunication Union (ITU) for emissions in the C and L bands. With that laser, they were able to achieve data rates as high as 100 Gb/s [62, 63].

Therefore, in order to obtain a mode spacing of 100 GHz , they cleaved their lasers to have an amplification cavity length of 420 µm which resulted in the comb-like (clear Fabry-Perot longitudinal modes) emission shown in Figure 2.7. By using an array waveguide grating (AWG) wavelength demultiplexer, as shown in their setup block diagram shown in Figure 2.7, they were able to achieve a transmission rate of 10 Gb/s over a 50 km long single mode fiber using the 8 Fabry-Perot spaced mode-locked modes. One year later, they were able to raise that rate to 56 Gb/s through implementing a differential quaternary phase-shift keying (DQPSK) scheme in their setup with a bit error rate (BER) of 4×10^{-7} [64].

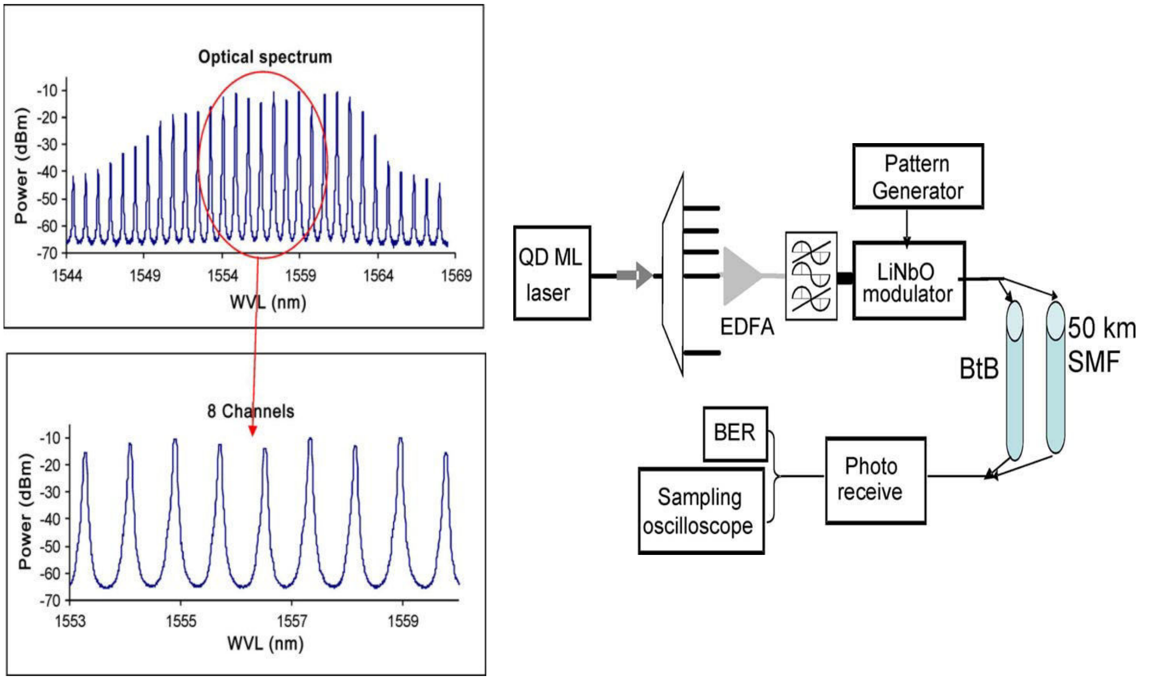

Figure 2.7: The experimental setup proposed in [62] (right) alongside the emission spectrum of the MLL QDash laser (left).

Near the end of 2015, the same group used a 980 µm long six-stacked MLL QDash laser whose emission spectrum is shown in Figure 2.8 (a) [65]. They were able to use 25 of the shown spectral lines in a 16QAM transmitter at a symbol rate of 18 gigabaud, as shown in Figure 2.8 (c). As a result, they were able to achieve a transmission rate of 1.562 Tb/s over a 75 km long single mode optical fiber and up to an aggregate rate of 2.678 Tb/s over B-B transmission where the associated BER at different emission wavelengths is shown in Figure 2.8 (b).

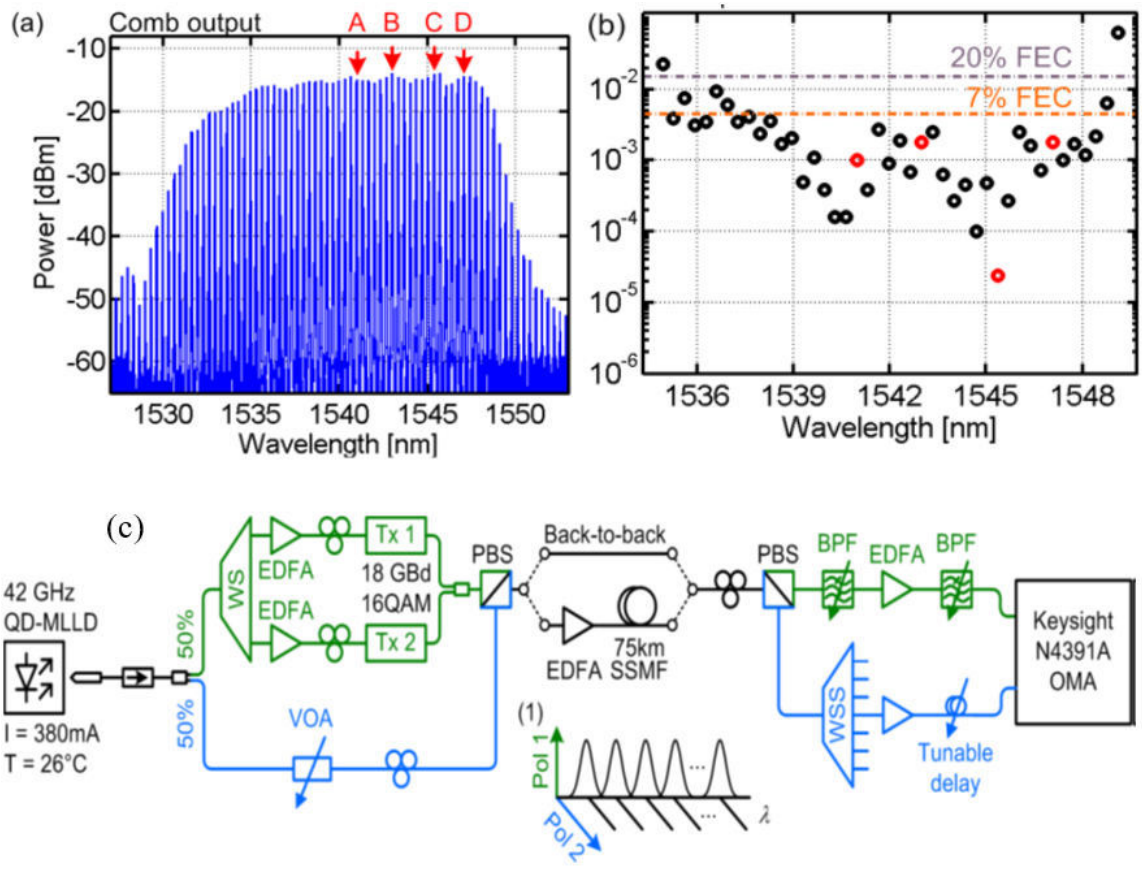

Figure 2.8: (a) Emission spectrum and (b) BER at different wavelength values of the demonstrated work in [65] which employed the setup illustrated in (c).

CHAPTER 3

DEVICE LEVEL CHARACTERIZATION

In this chapter, we investigate the chirped multi-stack QDash active region based semiconductor laser device. It is of great significance to quantitatively assess the performance and the quality of the laser device by performing a series of experimental measurements to extract fundamental laser parameters.

3.1 Chirped Multi-stacked QDash Laser

The main pivotal element of this work is the chirped InAs/InGaAlAs/InP QDash laser diode in the form of an as-cleaved Faby-Perot index-guided semiconductor device.

This laser has been grown by MBE over an n-type InP substrate doped with Sulfur. Figure 3.1 shows an AFM image of the quantum dashes where the elongated inhomogeneous dashes are clearly visible with the bright/dark regions representing the height variations among the dashes.

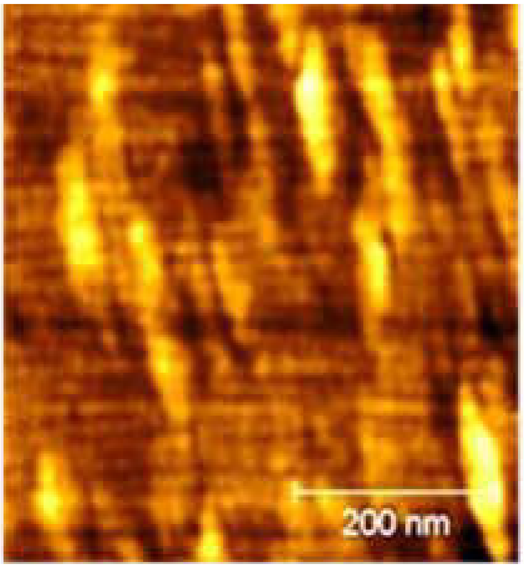

Figure 3.1: AFM image showing a horizontal slice of the active region of the chirped QDash laser where the bright/dark regions represent the height variations among the dashes (KAUST Photonics Laboratory).

The active region of this QDash laser is composed of four stacks each of 5 monolayers of InAs dashes embedded within 7.6 nm of strained $In_{0.64}Ga_{0.16}Al_{0.2}As$ non-symmetric quantum-wells followed by tensile-strained $In_{0.50}Ga_{0.32}Al_{0.18}As$ top layer with varying thickness values of 20 nm, 15 nm, 10 nm and 10 nm and a bottom barrier layer of fixed thickness of 25 nm. For convenience, we name these dash stacks as S20, S15, S10b and S10a, respectively. In general, varying the barrier layer thickness between different dash ensembles introduces more inhomogeneity thereby introducing wide emission range. Such inhomogeneity is attributed to the variant vertical strain exhibited by each stack during the growth process which has a direct influence on the variation of the dashes height leading ultimately to dissimilar emission wavelengths and consequently broader emissions. Figure 3.2 illustrates the laser structure used.

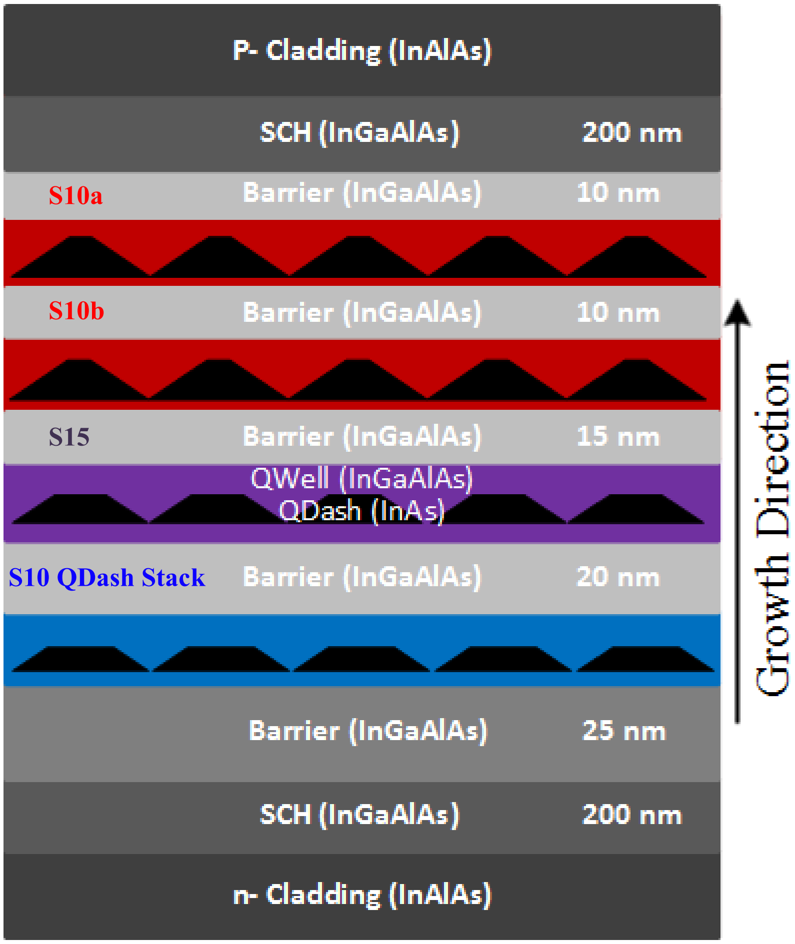

Figure 3.2: A layer-by-layer illustration of the structure of the laser diode.

In general, empirical results show that larger barrier layer thickness values correspond to grown QDashes of smaller heights and thus lower wavelengths when compared to QDashes of thinner barrier layers probably due to the different exhibited vertical strain during the growth process that is influenced by the thickness of the barrier layers in each case [60].

On the other hand, Figure 3.3 shows two Transmission Electron Microscopic (TEM) micrographs of the active region along the $[0\bar{1}1]$ plane (left) and $[011]$ plane (right). While the former show the dash elongation across the stacks, the latter shows the cross-sectional sizes of the dashes among each stack. The quantum dashes corresponds to the bright regions while the dark region corresponds to the barrier layers in both images.

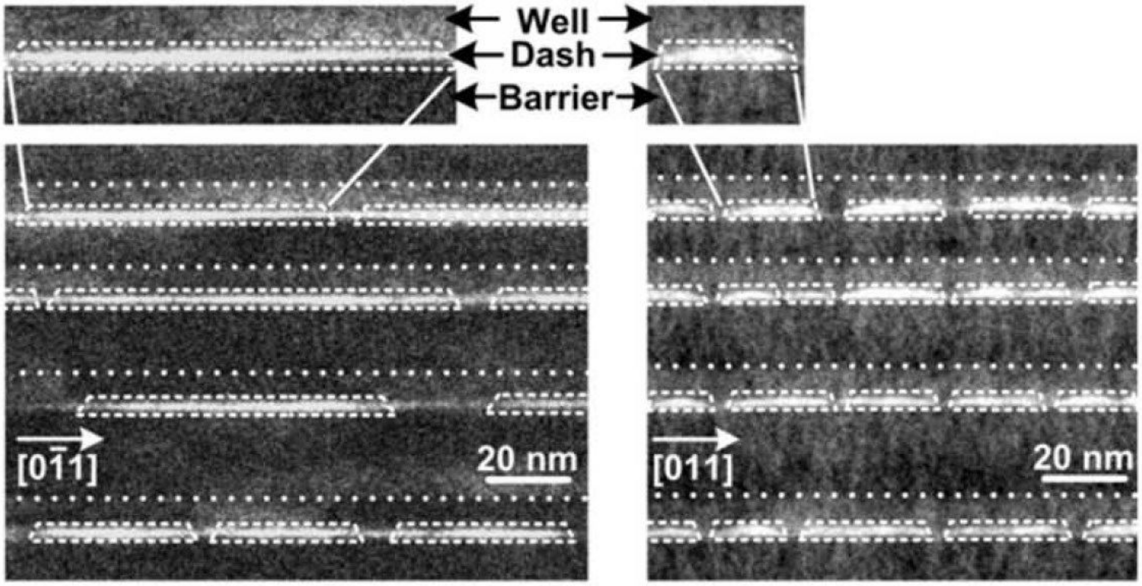

Figure 3.3: TEM images of the chirped active region of the QDash laser along the $[0\bar{1}1]$ plane (left) and $[011]$ (right) where the QDashes are visible as the bright regions while the dark region corresponds to the barrier layers (KAUST Photonics Laboratory).

Nevertheless, Figure 3.4 shows an illustration of the bandgap diagram of each of the four QDash ensembles inside the chirped active region alongside their overlapping quasi-zero-dimensional DOS. In addition, the normal distributions of the sizes of the QDash within each stack are represented by the dashed Gaussian curves that illustrate the overlap between QDashes that belong to neighboring stacks in terms of their sizes.

The ground state emission of each dash family is governed by Planck's equation:

$$\lambda = \frac{hc}{E} \tag{3.1}$$

where

- λ is the wavelength (in meters) of the emitted photon.
- h is Plank's constant which equals 6.626×10^{-34} J.s.
- c is the free-space speed of light.
- E is the energy (in Joule) of the emitted photon which corresponds to the effective energy bandgap of the QDash.

Therefore, QDashes of larger heights within the thinner barrier-layer stack are associated with longer wavelength (lower energy) emission. On the other hand, QDashes of smaller heights within thicker barrier-layer stacks are associated with shorter wavelength (higher energy) emission. This behavior can be attributed to the extra quantum confinement exerted by the smaller height QDashes when compared to their larger height counterparts.

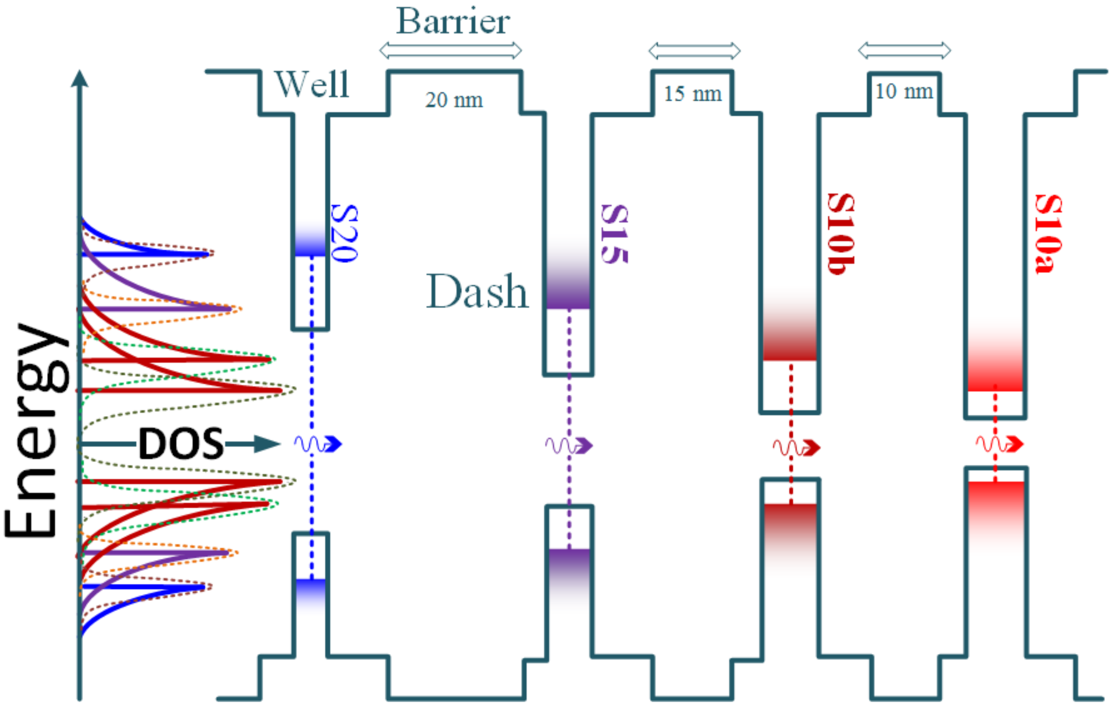

Figure 3.4: An illustration of the energy band diagram corresponding to different QDash stacks alongside their respective overlapping quasi-dimensionless DOS.

3.2 Characterization Elements

3.2.1 Laser Diode Specimens

Using the previously discussed structure, lasers were fabricated and then cleaved into bars of different cavity lengths. Figure 3.5 shows an illustration of a laser bar containing three laser devices of identical cavity length. In our case, each bar contains laser devices with different ridge width values, namely 2 µm, 3 µm, and 4 µm among which different devices were tested and characterized.

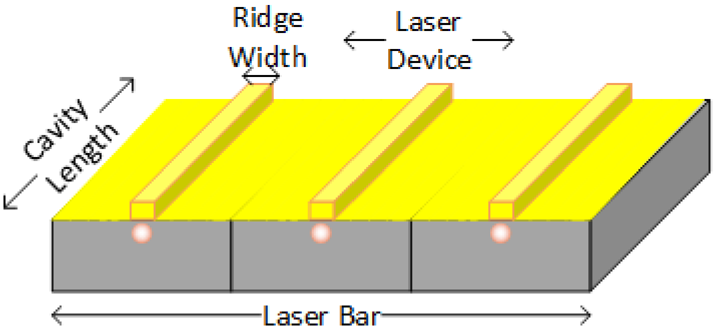

Figure 3.5: An illustration of a single laser bar containing several fixed cavity-length devices.

Figure 3.6 shows a microscopic image of three laser devices of different ridge widths, all having a 2500 µm long cavity length.

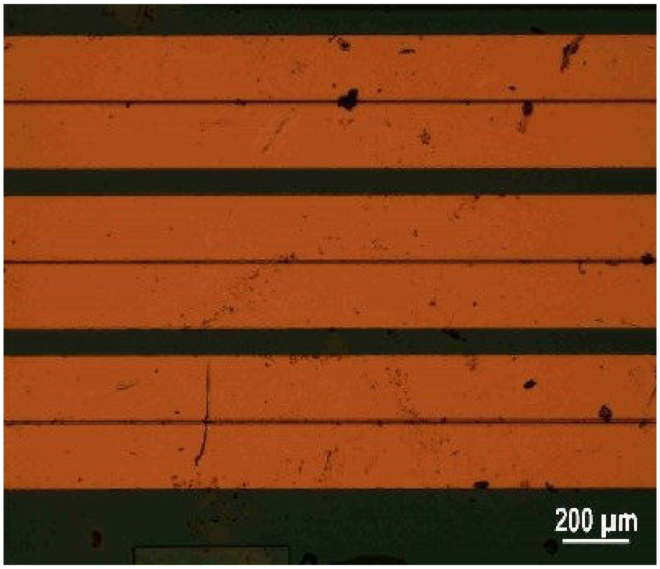

Figure 3.6: A microscopic image of a single 2500 um laser bar where three laser diodes are visible with different ridge width, namely 2 µm, 3 µm, and 4 µm (from top to bottom).

3.2.2 Experimental Setup

To characterize the performance of these devices, each of them was mounted on a brass base with p side up configuration. Two probes are then used where the negative one is connected to the brass base while the positive probe is placed over a gold plated clamp that is in contact with the p side of the laser in order to safely probe the current into the laser diode. The characterization of these lasers was done under a short-pulse width (SPW) operation with a pulse width of 0.5 µs and a delay width of 250 µs (0.2% duty cycle). This is done in order to minimize the heat buildup within the laser that can lead to increased junction temperature, which has a drastic impact on the performance of the laser diodes. After probing each laser, the voltage drop across the device was measured and recorded. Simultaneously, an integrating hemi-sphere with an InGaAs photodetector collects the emitted photons from the laser device facet and provides an equivalent optical power that is used to find the output light vs drive current (L-I) characteristics of the laser. Figure 3.7 shows a mounted laser bar that is being probe-injected alongside the integrating hemi-sphere.

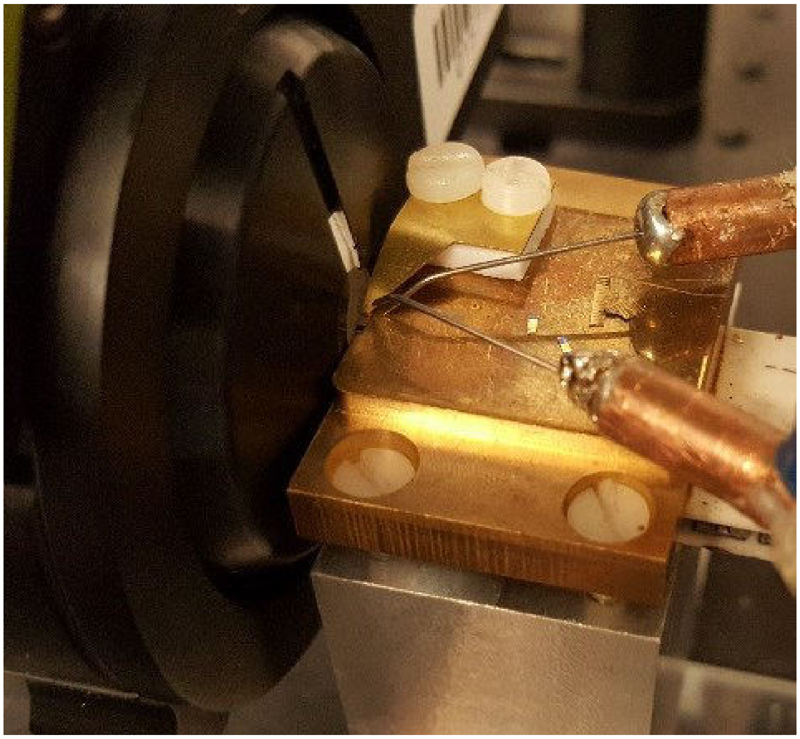

Figure 3.7: A laser diode being pumped while the voltage drop and the output optical power are being measured.

Next, the best performing laser device among each group of identical cavity length devices was selected depending on their threshold current values and efficiency slopes (both are extracted from the L-I characteristics of the device). Each selected device optical power was butt-coupled into an optical fiber, as shown in Figure 3.8, whose other end was connected into an optical power meter in order to successfully align the optical fiber facet with the emitted laser beam from ridge of the laser.

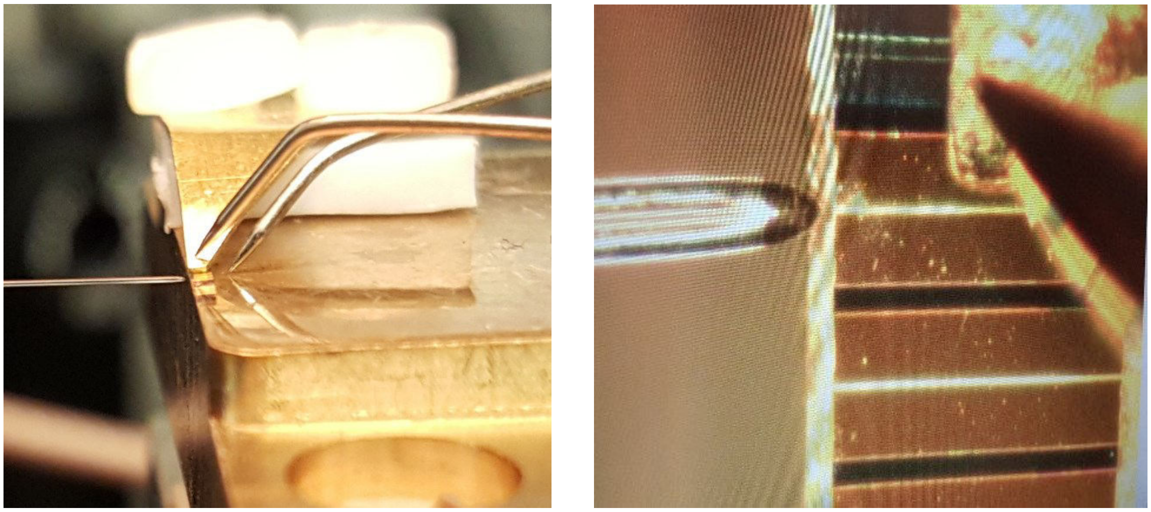

Figure 3.8: Side and top views showing the alignment of the fiber with the facet of a laser diode to its ridge.

Finally, after successfully positioning the fiber with the optical mode of the laser diode, we connect it into an optical spectrum analyzer (OSA) which shows the emission spectra. Different emission spectra are collected from each device at different current injection values which are later used to identify their emission profiles and ultimately their emission coverage and 3dB bandwidth.

Figure 3.9 shows a schematic that illustrates the various setup components used for the characterization experiments.

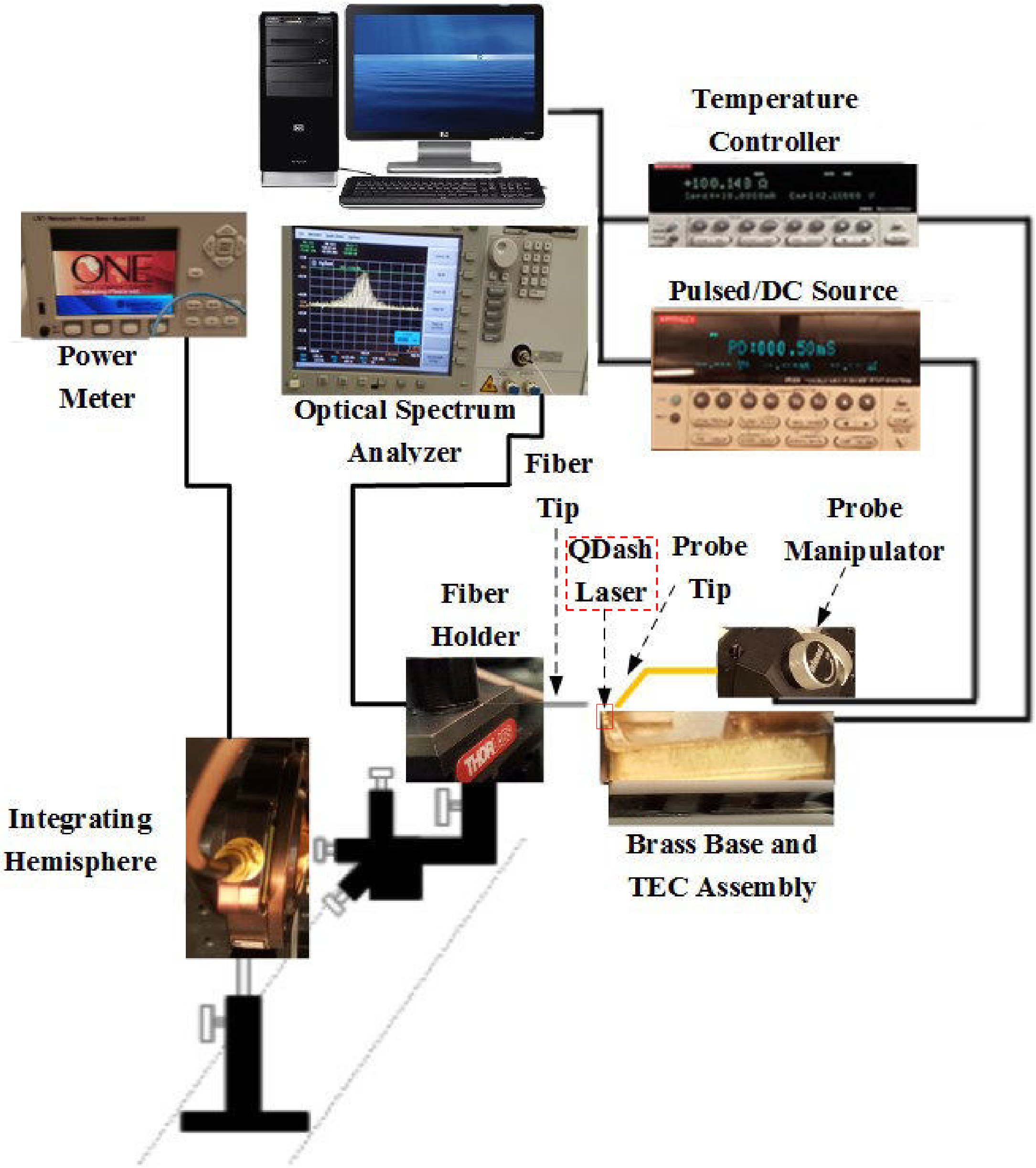

Figure 3.9: Illustration showing the laser diode characterization setup.

3.3 Laser Diode Principle Parameters

3.3.1 Voltage Drop vs. Input Current Characteristics

The purpose of finding the voltage drop vs. input current curve (I-V) is to identify the diode-like behavior of the laser devices. The slope of the I-V curve denotes the dynamic series resistance of the diode. Figure 3.10 shows the I-V characteristics curve of a sample laser diode whose ridge width is 4 µm. As expected from a typical diode behavior, the turn on voltage is ~ 0.7 V beyond which, the average dynamic series resistance is ~ 3.2 Ω.

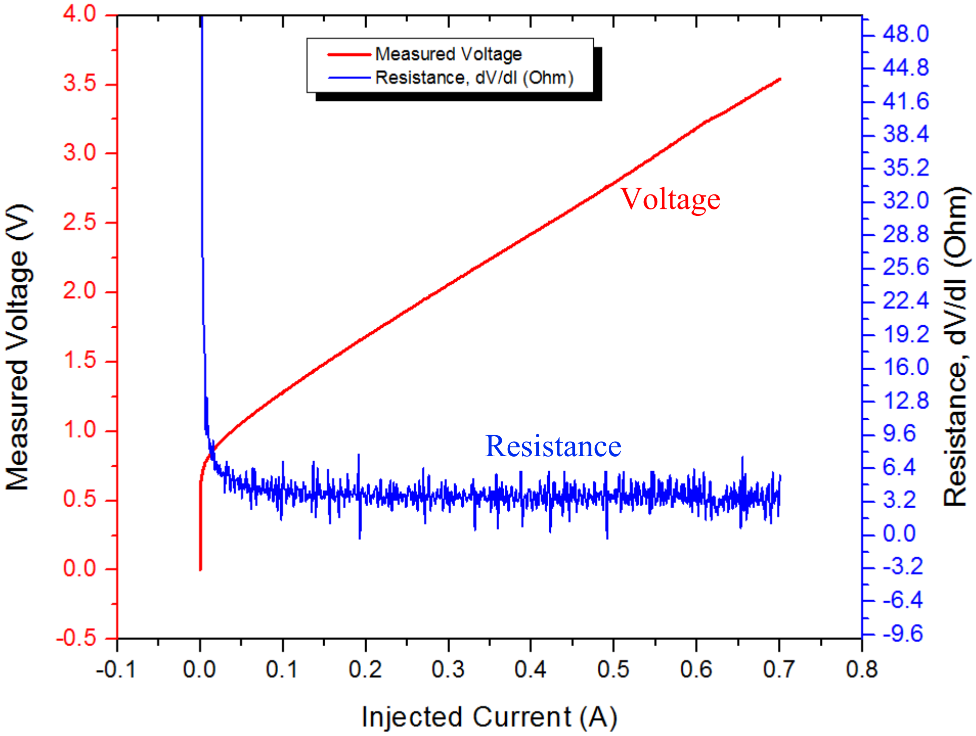

Figure 3.10: I-V characteristic curve of a sample laser diode alongside its corresponding resistance vs. injected current curve.

3.3.2 Output Light Power vs. Input Current Characteristics

The output light power vs. input current (L-I) curve is considered among the most significant characteristics of laser diodes as it describes how well the device performs with respect to the injected current. The photodetector that was used in our characterization actually measures the photo current, which is then converted to optical power using a responsivity of 6.54 mA/W (for 1.6 µm wavelength).

As a small current is being injected into the device, the laser diode operates as an LED with spontaneous emission taking place since the gain of the active medium at this point has not yet overcome the losses. However, as injection current increases beyond the threshold current I_{th}, the gain inside the active medium exceeds the threshold gain resulting in stimulated emission and lasing action takes place. When the threshold current is divided by the area of current pumping (we assumed it to be cavity length × ridge width) gives the threshold current density J_{th}. Threshold current density is an indicator of how good the active medium material is; the lower its value the better the material is.

Another significant parameter that can be extracted from the L-I curve is its slope which is called “slope efficiency”. This slope indicates how much optical power is being emitted by the laser diode with respect to the injected current. Therefore, a higher value for this slope is desirable and is another direct indicator of the performance efficiency of the laser device. Figure 3.11 shows the L-I curve of a sample laser diode.

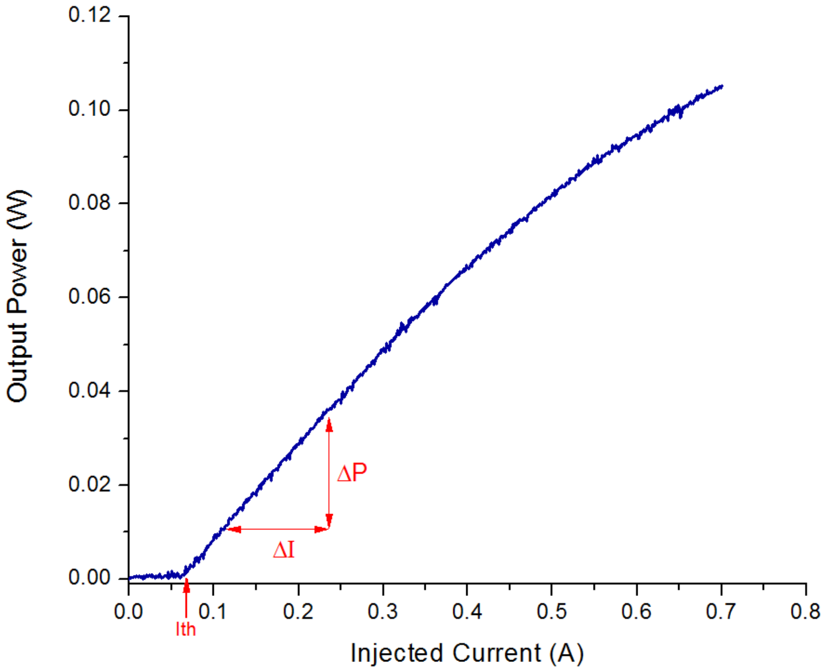

Figure 3.11: L-I characteristic curve of a sample laser diode showing the sloe efficiency alongside the threshold current at the onset of the stimulated emission.

3.3.3 External Quantum Efficiency

When a flux of charge carriers flows through the active region as current gets pumped into the device, photons get generated after successful radiative electron-hole pair recombination. However, not all recombinations result in generation of photons but rather, some recombinations result in non-radiative processes like the

Auger recombination. This type of recombinations raises the junction temperature of the device. Moreover, a portion of the generated photons do not successfully escape the boundaries of the device as they reflect at the interface or get reabsorbed altogether. The external quantum efficiency is a parameter that relates the amount of generated optical power out of the laser diode with respect to the amount of injected current. It represents how efficient the laser diode is in converting the pumped carriers inside the device into optical power that gets out of the laser diode. The external quantum efficiency can be found through the slope efficiency using the following relation [66]:

$$\eta_d = \frac{\Delta P}{\Delta I} \cdot \frac{q\lambda}{hc} \tag{3.2}$$

where

- η_d is the external differential quantum efficiency.
- $\frac{\Delta P}{\Delta I}$ is the L-I curve slope efficiency in W/A.
- h is Planck's constant and equals 6.6262×10^{-34} J.s.
- λ is the emission center wavelength.
- c is the speed of light in a vacuum and equals 2.99×10^{8} m/s.
- q is the charge of an electron which equals 1.60022×10^{-19} C.

3.3.4 Internal Quantum Efficiency and Internal Loss

The external quantum efficiency is a measure of performance of different laser cavities. On the other hand, the internal quantum efficiency (η_i) is a performance parameter of the material of the active region itself regardless of its length. The internal quantum efficiency is a measure of how much of the injected electron-hole pairs is contributing to light emission through radiative recombinations.

In order to find this parameter, the external differential quantum efficiency values are plotted against different cavity lengths. The plotted data points are linearly fitted then extrapolated as a straight line in order to find the y-intercept of the fitted straight line. The inverse of this value represents the internal quantum efficiency according to [66]

$$\frac{1}{\eta_d} = \frac{1}{\eta_i}[1 + \frac{\alpha_i}{\ln(1/R)} L] \tag{3.3}$$

where

- η_i is the internal quantum efficiency
- α_i is the internal loss (cm^{-1})
- R is the reflectivity of the mirror facets of the laser cavity and equals 31% in typical lasers GaAs or InP based lasers

The internal loss is a parameter that represents the portion of lost generated photons due to reabsorption in the device structure before exiting the cavity through the mirror facets of the laser diode.

3.3.5 Transparency Current Density

Much like the internal quantum efficiency being a material parameter of the active region, the transparency current density, unlike the threshold current density, does not depend on the length of the active region. It is a measure of when the losses in the active region is compensated (i.e. Loss = Gain). Therefore, it makes more sense to use this parameter instead as an absolute indicator rather than dimension dependent parameters.

The transparency current density J_o equals the y-intercept of the plot between the threshold current density J_{th}, at different cavity length values, against the inverse of these lengths.

3.3.6 Characteristic Temperature

The characteristic temperature (T_o) is a parameter that indicates how consistent the performance of the laser diode is at increasing temperature. This parameter is of a substantial significance since temperature plays a vital role in most of the quantum mechanics that occur within the active region. In general, higher values of T_o correspond to more thermally stable specimens. As temperate increases, an overall degradation is witnessed by the device as the quantum efficiency decreases. Hence, the threshold current density that is required to overcome the extra introduced losses is increased exponentially as temperature increases as [66]

$$J_{th} = J_c \, e^{T/T_o} \tag{3.4}$$

$$\ln\left(\frac{J_{th}}{J_c}\right) = \frac{T}{To} \tag{3.5}$$

$$\ln(J_{th}) - \ln(J_c) = \frac{T}{To} \tag{3.6}$$

$$\Delta \ln(J_{th}) = \frac{1}{T_o} \Delta \mathrm{T} \tag{3.7}$$

$$T_o = \frac{\Delta \mathrm{T}}{\Delta \ln(\mathrm{J_{th}})} \tag{3.8}$$

where

- J_{th} is the threshold current density.
- J_c is a differential constant.
- T_o is the characteristic temperature.

Therefore, the characteristic temperature of a laser device can be found by plotting the natural logarithm of J_{th} vs. different temperature values and finding the reciprocal of the slope.

3.4 Parameters Measurements

The previously discussed laser diode characterization has been carried out for multiple laser diodes of different cavity lengths while using 2 and 4 ridge width devices in each case.

3.4.1 The Narrow Ridge Laser

Figure 3.12 shows the I-V curves of 5 different cavity length lasers, all having a narrow ridge width of 2 µm. Table 3.1 shows the average Ohmic series resistance values of different cavity lengths after they were extracted from the slope of their respective I-V curves.

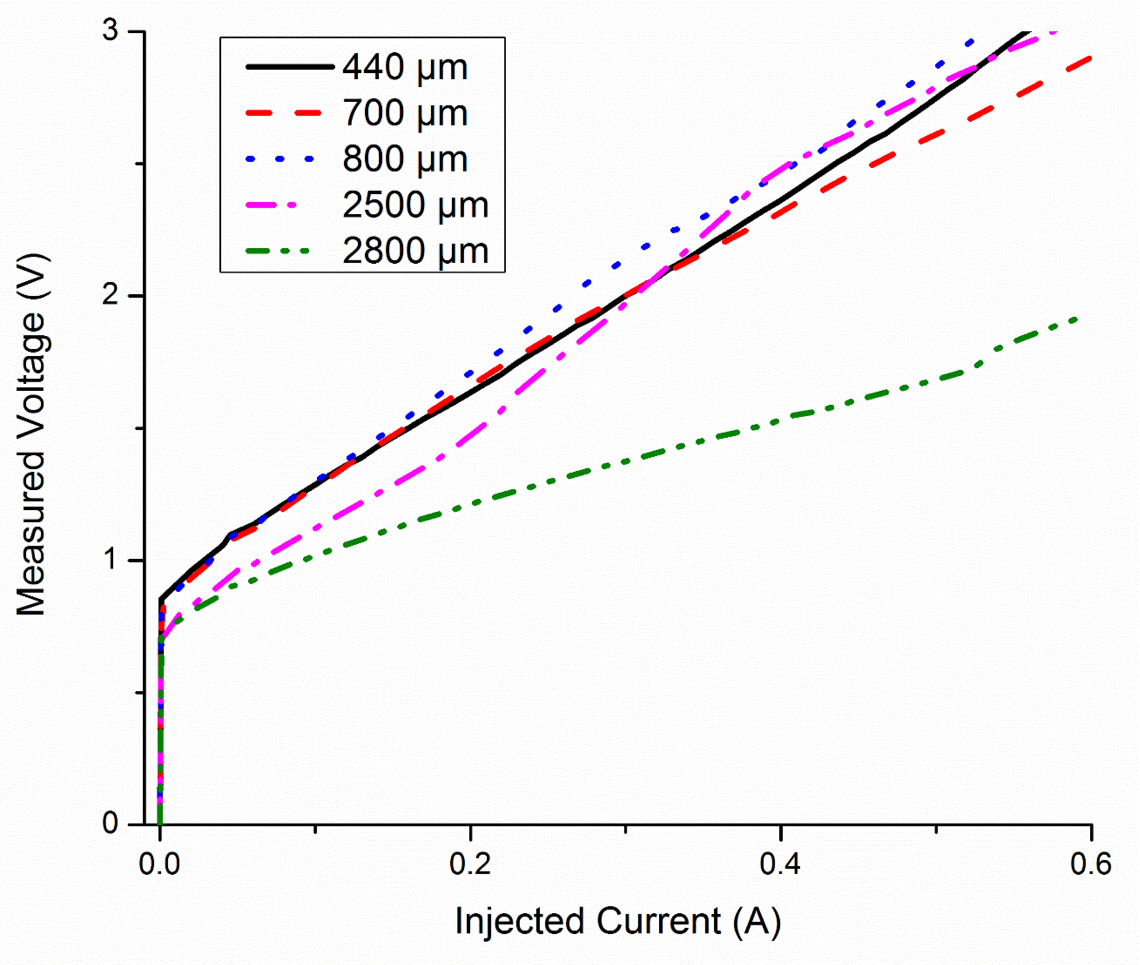

Figure 3.12: I-V characteristic curves for 5 different cavity length devices each of 2 um ridge width.

Table 3.1: Resistance values of different cavity length lasers.

Cavity Length [µm]	440	700	800	2500	2800
Resistance [Ω]	1.52	2.92	3.52	5.22	5.56

As expected, the longer the cavity, the higher the resistance of the device is, starting from 1.52 Ω for the 440 µm up to 5.56 Ω for the 2800 µm long device.

Figure 3.13 shows the L-I curve of all examined cavity lengths while Table 3.2 shows the threshold current and threshold current density and optical power slope efficiencies.

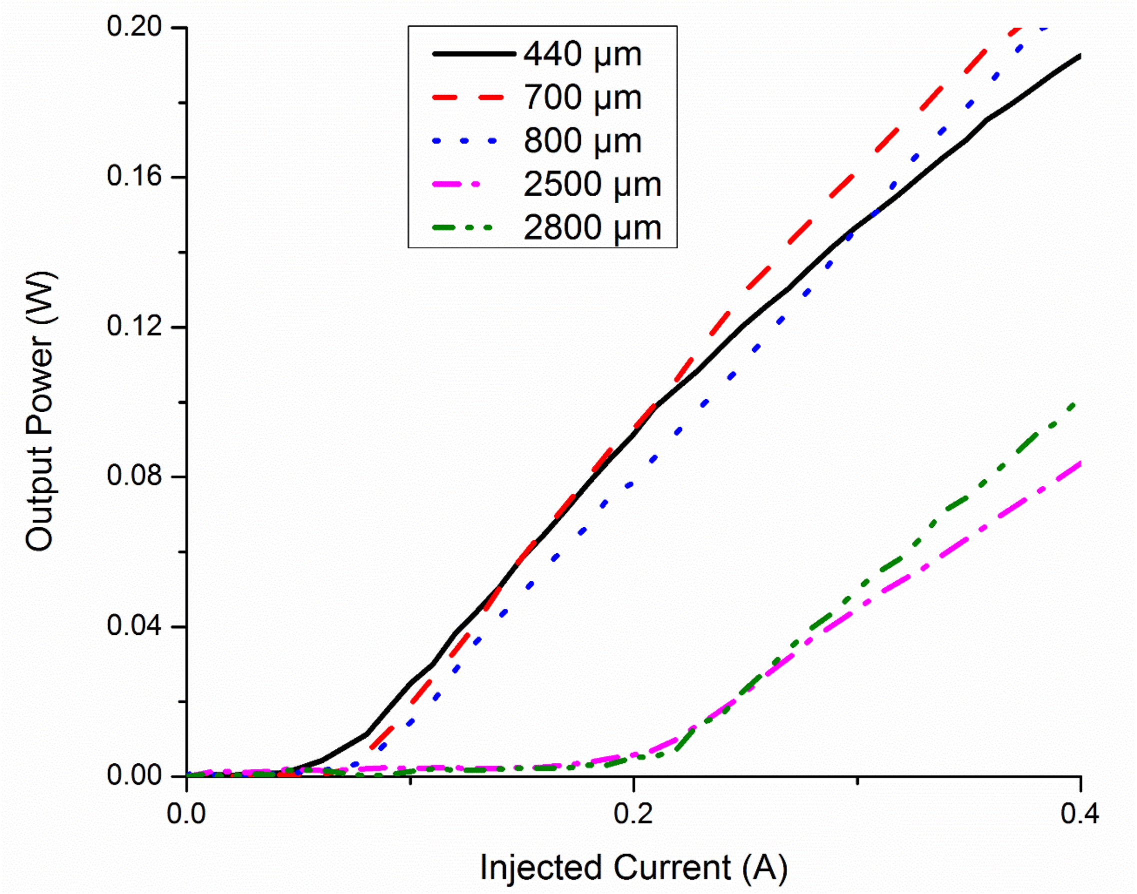

Figure 3.13: L-I Characteristics of different cavity length devices.

It is clear from the plots that the longer the cavity is, the lower its threshold current density gets. Such behavior is probably a direct result of reduction in the mirror loss of the device (which is inversely proportional to the cavity length) and hence the total device loss.

Table 3.2: Threshold current density and efficiency slope of different cavity length devices.

Cavity Length [µm]	440	700	800	2500	2800
Threshold Current [A]	0.0415	0.0575	0.0656	0.180	0.1994
Active region Area [cm^2]	0.88×10^{-5}	1.4×10^{-5}	1.6×10^{-5}	5.0×10^{-5}	5.6×10^{-5}
Threshold Current Density (J_{th}) [A/cm2]	4704.55	4107.14	4100.00	3600.00	3560.71
Optical Efficiency Slope [W/A]	0.840	0.634	0.571	0.347	0.347

This in turn enables stimulated emission process to commence at earlier current injections. However, as more carriers are injected into the active medium, the losses accelerate as the junction temperature rises resulting in a reduction of the efficiency slopes as observed in Figure 3.13 at intermediate and high current injections with an eventual optical power roll-off that is taking place when the slope is reduced by 50%.

Using (3.1), the external quantum efficiency for each cavity length laser is found using the optical efficiency slope and tabulated in Table 3.3. Much like threshold current density, longer cavities show lower external quantum efficacies according to the equation 3.3. In other words, longer cavity lengths are clamped at lower threshold gain compared to the shorter cavity lengths which directly effects the optical slope efficiency of the device.

Table 3.3: The external quantum efficiency of different 2 µm cavity lengths laser devices.

Cavity Length [µm]	440	700	800	2500	2800
External Quantum Efficiency (η_d) [%]	90.77	82.84	74.75	45.80	45.52
$1/\eta_d$	1.83	2.41	2.68	4.37	4.39

In order to find the internal quantum efficiency, the external differential quantum efficiency values are plotted against different cavity lengths as shown in Figure 3.14 which are then tabulated in Table 3.4. The y-intercept of the extrapolated line represents the inverse of the internal quantum efficiency while its slope can be used to find the internal loss according to according to (3.3). The y-intercept of the extrapolated line is 1.23885 which is when inverted equals η_i=80.72%. On the other hand, the slope of the line equals α_i / η_i ln(1/R)=0.00119 which when multiplied by $\eta_i$ln(1/R) gives the internal loss of the medium that equals 11.90 cm^{-1}.

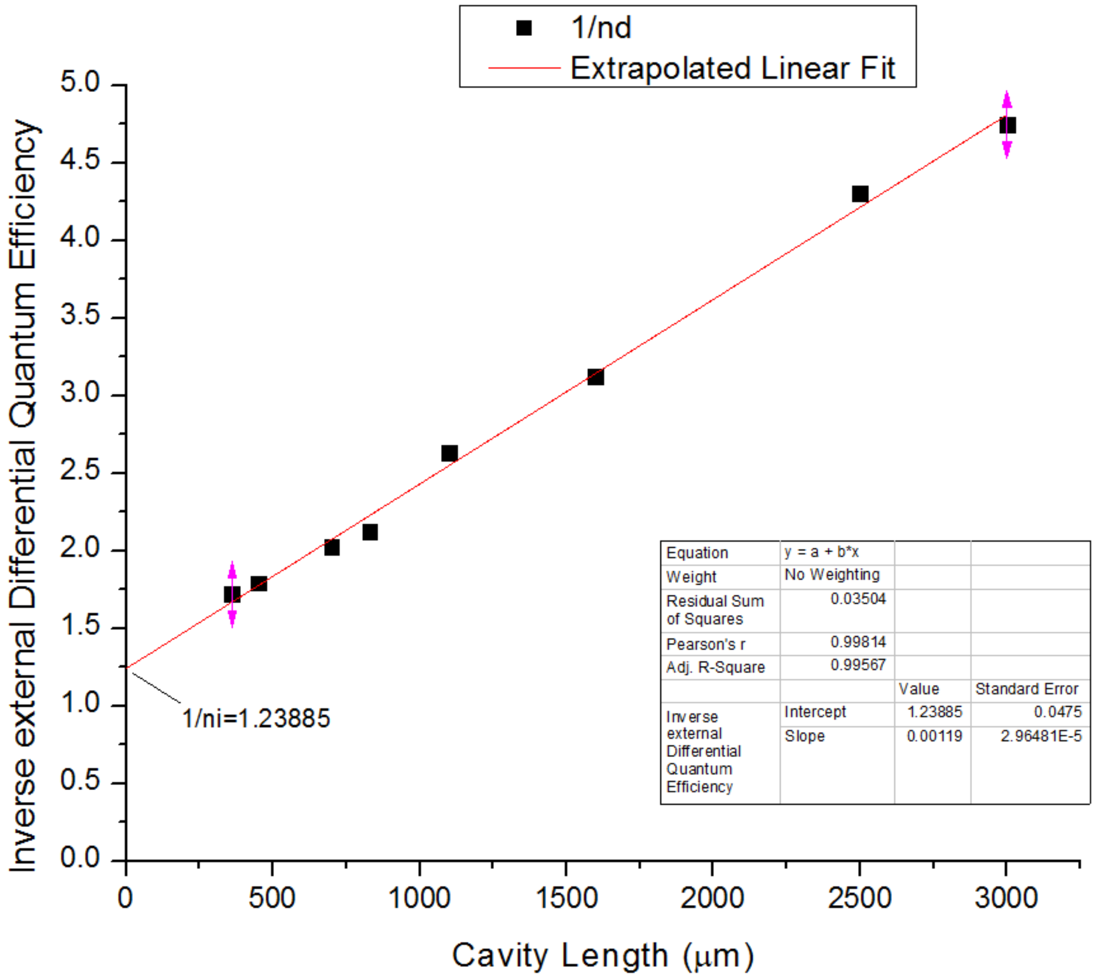

Figure 3.14: Linearly fitted line of $1/\eta_d$ against different cavity lengths whose y-intercept gives the inverse of internal quantum efficinecy while the slope can be used to find the internal loss of the active region.

Figure 3.15 shows an extrapolated linearly fitted line from the threshold current density values at the inverse of different cavity length values in cm^{-1} tabulated in Table 3.5. The extrapolated fitted line shows that the transparency threshold current density of this laser is 3349.07 A/cm^2.

Table 3.4: The Internal quantum efficiency and the internal loss parameters of the 2 µm QDash laser.

$1/\eta_i$	Internal Quantum Efficiency (η_i) [%]	Slope [µm^{-1}] $\alpha_i/\eta_i \ln(1/R)$	Internal Loss (α_i) [cm^{-1}]
1.2388	80.72	0.00119	11.90

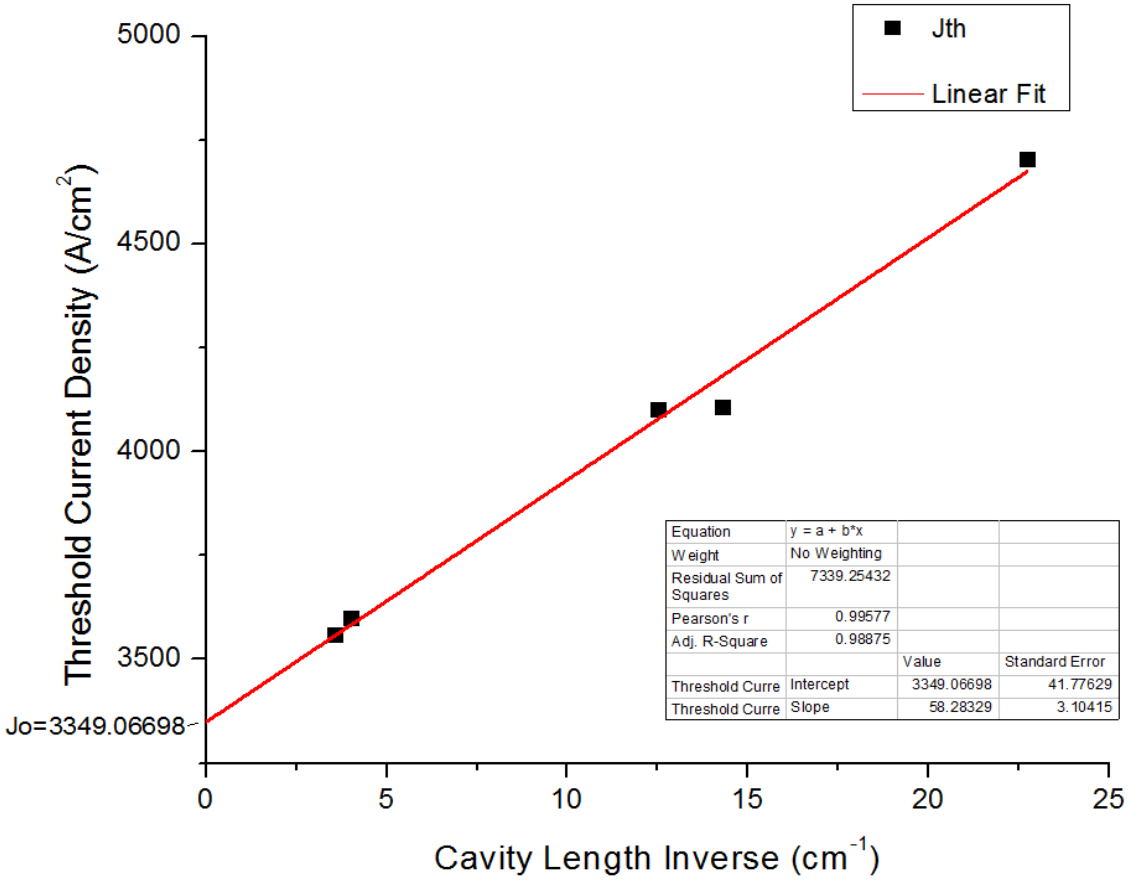

Equation	y = a + b*x		
Weight	No Weighting		
Residual Sum of Squares	7339.25432		
Pearson's r	0.99577		
Adj. R-Square	0.98875		
		Value	Standard Error
Threshold Curre	Intercept	3349.06698	41.77629
Threshold Curre	Slope	58.28329	3.10415

Figure 3.15: An extrapolated linear fit of threshold current density vs. the inverse of different cavity length values of the 2 µm ridge width lasers.

Table 3.5: Threshold current densities at different cavity lengths and their inverse for the 2 µm ridge width.

Cavity Length (L) [cm]	0.044	0.07	0.08	0.25
Inverse Cavity Length (1/L) [cm^{-1}]	22.73	14.29	12.5	4.00
Threshold Current Density (J_{th}) [A/cm^2]	4704.55	4107.14	4100.00	3600.00

3.4.2 The Wide Ridge Laser

In order to investigate the effect of the ridge width of the laser diode on its characteristic parameters, we perform the same measurements on different cavity length laser diodes using the 4 µm ridge width devices for each cavity length and compare the results to the previously found ones for the case of 2 µm ridge width case.

Starting with the I-V characteristics, Figure 3.16 shows the I-V curve of different cavity length laser diodes. In addition, Figure 3.17 shows the L-I characterisitcs of each of these laser diodes where the extracted paramters are tabulated in Table 3.6.

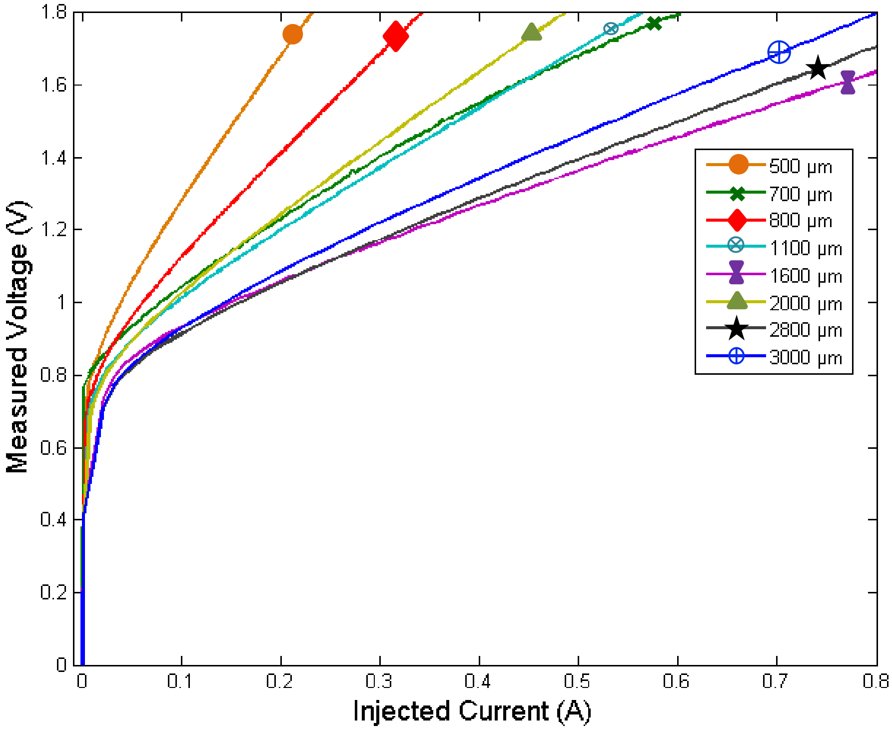

Figure 3.16: I-V characteristics of different cavity length laser diodes of 4 µm ridge width.

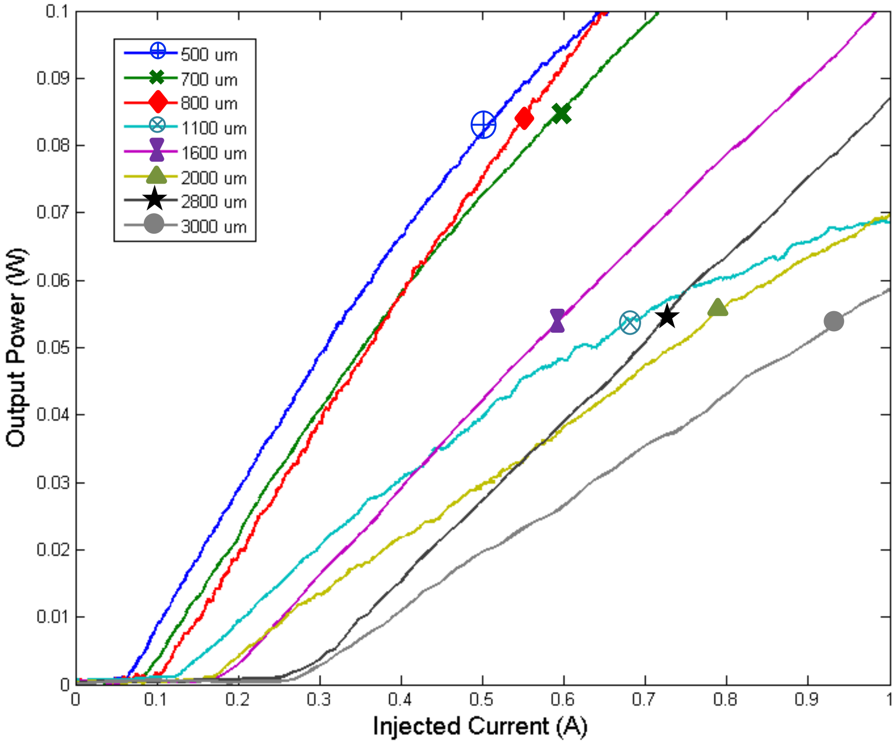

Figure 3.17: L-I characteristics of different cavity length laser diodes of 4 µm ridge width.

As previously discussed, in general, longer cavity laser diodes are associated with lower threshold gain and hence less quantum efficiency. However, a sharp decrease in the slope efficiency is observed in the case of the 1100 µm and 2000 µm lasers at higher current injections suggesting sub-optimal fabrication of these two devices. More interestingly, by comparing the L-I characteristics of the narrower 2 µm ridge lasers with their wider 4 µm counterparts, we observe that the latter has a better overall performance as it has a higher slope efficiency (external quantum efficiency) while requiring lower threshold current density in order to initialize the stimulated emission process. Such observation can be possibly explained by the smaller active region volume in the 2 µm ridge lasers compared with their wider 4 µm counterparts. Moreover, the narrower ridge widths exhibit a more substantial lateral current spreading as demonstrated in [67] in addition to the possible ridge side-wall scattering loss.

Table 3.6: Extracted efficiency parameters of the 4 µm ridge laser diodes.

Cavity Length [µm]	500	700	800	1100	1600	2000	2800	3000
I_{th} [A]	0.068	0.088	0.108	0.129	0.180	0.197	0.280	0.299
(J_{th}) [A/cm2]	3415	3372	3146	2925	2808	2467	2496	2488
Efficiency Slope [W/A]	0.208	0.185	0.182	0.181	0.131	0.100	0.097	0.080

Thereafter, by extrapolating the linearly fitted line of the reciprocals of the extracted external quantum efficiencies as shown in Figure 3.17, we can find the internal loss α_i from the slope of the fitted line while its y-intercept gives the reciprocal of the internal quantum efficiency η_i according to (3.3) which are tabulated in Table 3.7.

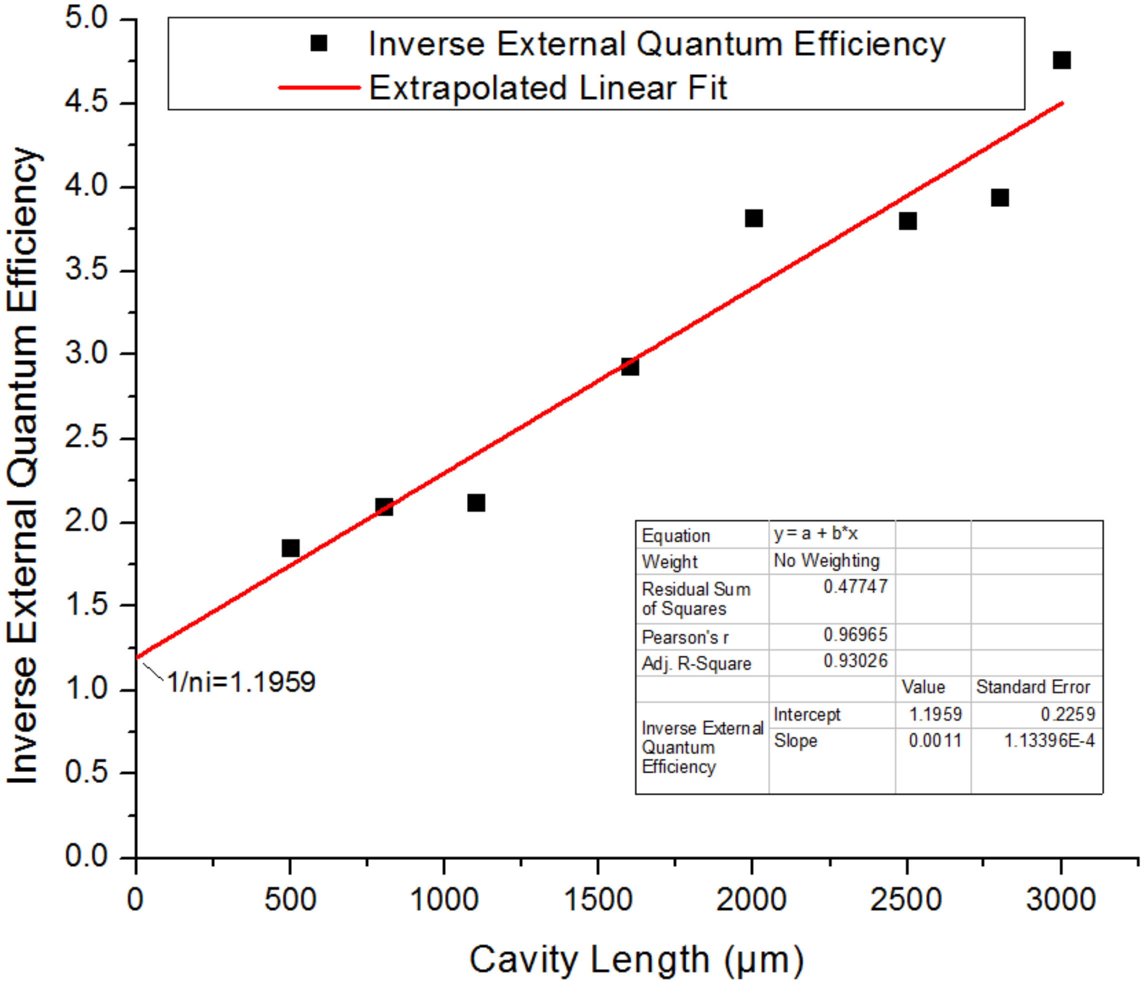

Equation	y = a + b*x		
Weight	No Weighting		
Residual Sum of Squares	0.47747		
Pearson's r	0.96965		
Adj. R-Square	0.93026		
		Value	Standard Error
Inverse External Quantum Efficiency	Intercept	1.1959	0.2259
	Slope	0.0011	1.13396E-4

Figure 3.18: Extrapolated linear fit of the inverse external quantum efficiencies of the difference 4 μm cavity length devices.

As expected, the material dependent internal quantum efficiency is nearly the same in both cases of the wider 4 μm and the narrow 2 μm case averaging around ~ 82%

± 1.5%. Similarly, the internal loss was more or less identical in both cases averaging around 11.3 cm^{-1} ± 0.55 cm^{-1}.

Table 3.7: The Internal quantum efficiency and the internal loss parameters of the 4 µm QDash laser

$1/\eta_i$	Internal Quantum Efficiency (η_i) [%]	Slope [µm^{-1}] $\alpha_i/\eta_i \ln(1/R)$	Internal Loss (α_i) [cm^{-1}]
1.1959	83.62	0.00110	10.77

Figure 3.19 shows an extrapolated linear fit of the threshold current densities associated with different cavity lengths in order to extract the transparency current density which was found to be ~ 2183.4 A/cm^2.

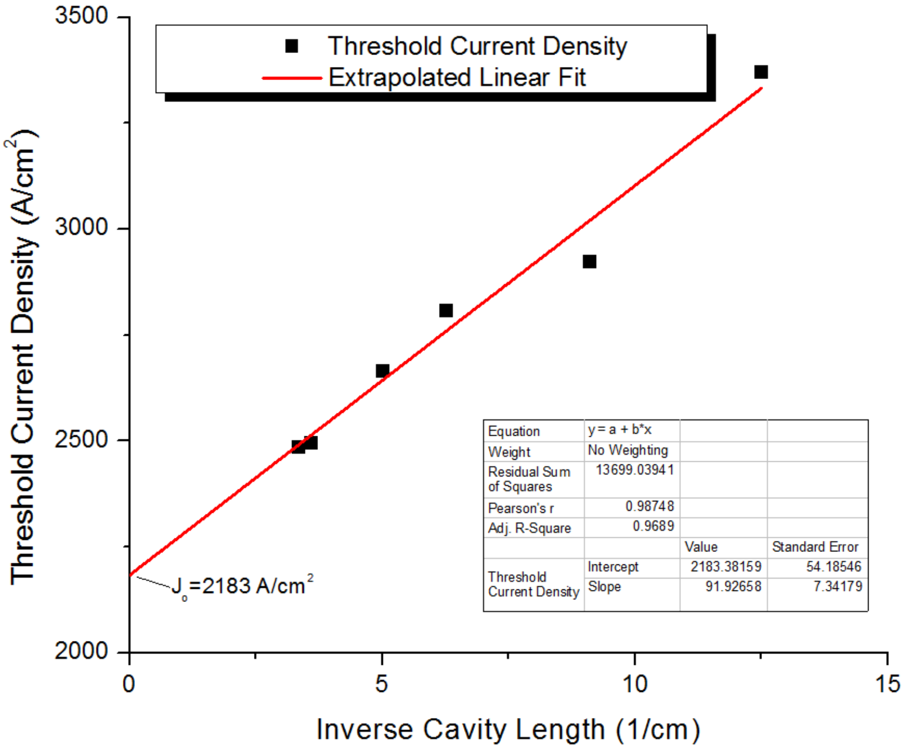

Equation	y = a + b*x		
Weight	No Weighting		
Residual Sum of Squares	13699.03941		
Pearson's r	0.98748		
Adj. R-Square	0.9689		
		Value	Standard Error
Threshold Current Density	Intercept	2183.38159	54.18546
	Slope	91.92658	7.34179

Figure 3.19: An extrapolated linear fit of threshold current density vs. the inverse of different cavity length values of the 4 µm ridge width case.

The improvement in the transparency current densities observed in the wider ridge lasers also affirm our postulation that the lateral current spreading and side-wall scattering possess more dominant effect on narrower ridge widths lasers.

Finally, the L-I curve was found for a 4 µm × 1600 µm laser diode at different temperatures by controlling the temperature of the brass base over which the laser device was mounted through a thermo-electric cooler. Since lasing operation takes place under a very short duty cycle (0.2%), it is safe to assume that the junction temperature of the laser is very close to that of the temperature of the brass base. Figure 3.20 shows the L-I characteristics of the examined laser specimen at different temperatures (15^{o} C, 20^{o}C – 70^{o} C in steps of 10^{o} C).

The inset of Figure 3.20 shows the progressive increase (decrease) in threshold current (slope efficiency) as a function of the temperature. At 50^{o}C, a very sharp decrease in the slope efficiency occurs, and thus in the quantum efficiency, is observed accompanied by a steep increase in the threshold current of the device. It is no surprise that the threshold current increases as the temperature rises. Such observation can be attributed to the increased active region losses as more phonons are generated as a result of thermally induced lattice vibrations. In addition, less photons are generated at elevated temperatures as more non-radiative recombinations take place.

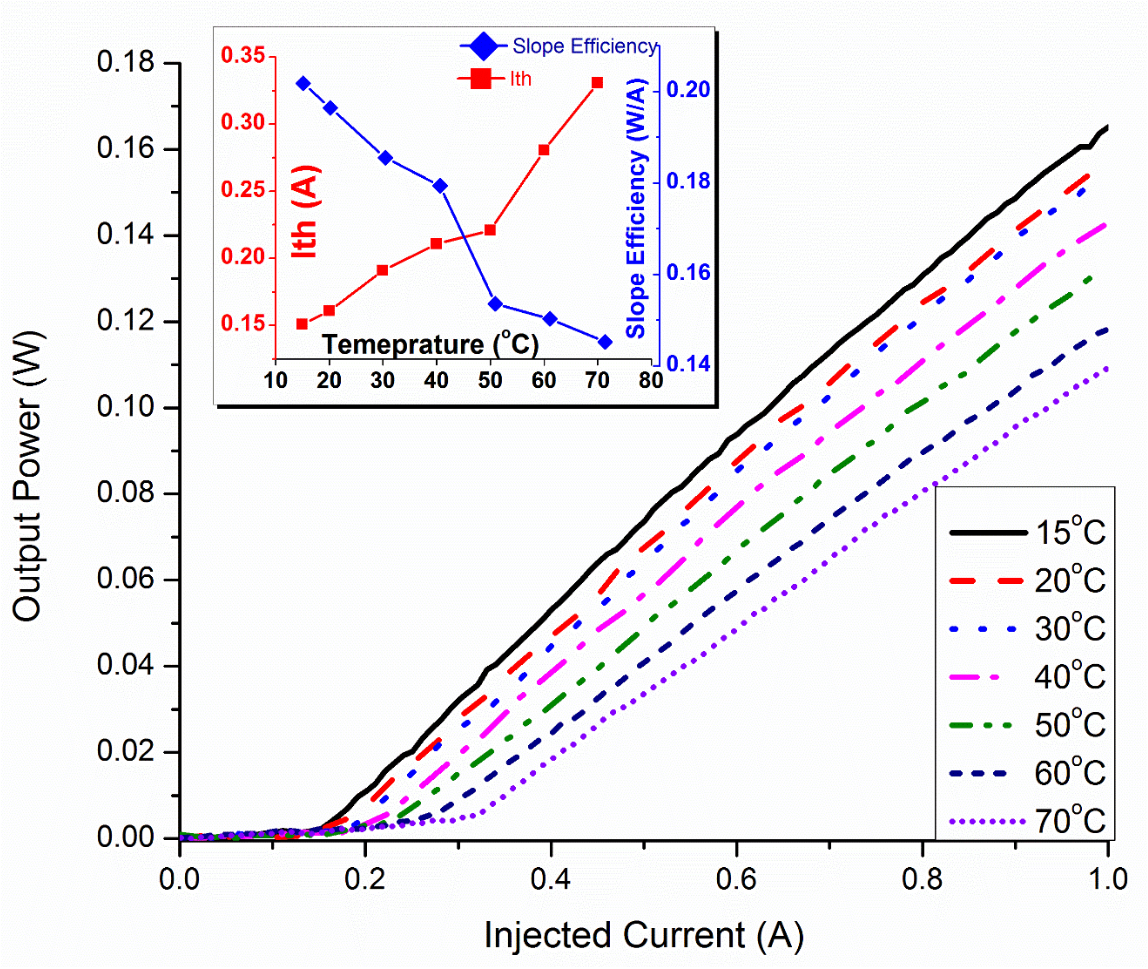

Figure 3.20: L-I characteristics of the examined 4 µm × 1600 µm laser at different temperatures (15^{o} C, 20^{o} C – 70^{o} C in steps of 10^{o} C). The inset shows the progressive increase (decrease) in I_{th} (slope efficiency) as a function of the temperature.

After extracting the threshold current densities at each temperature value, the natural logarithm of these densities are plotted as a function of the temperature as shown in Figure 3.21. Thereafter, according to (3.8), the reciprocal of the slope of the linearly fitted curve gives the characteristic temperature which was equal to 73^{o} K.

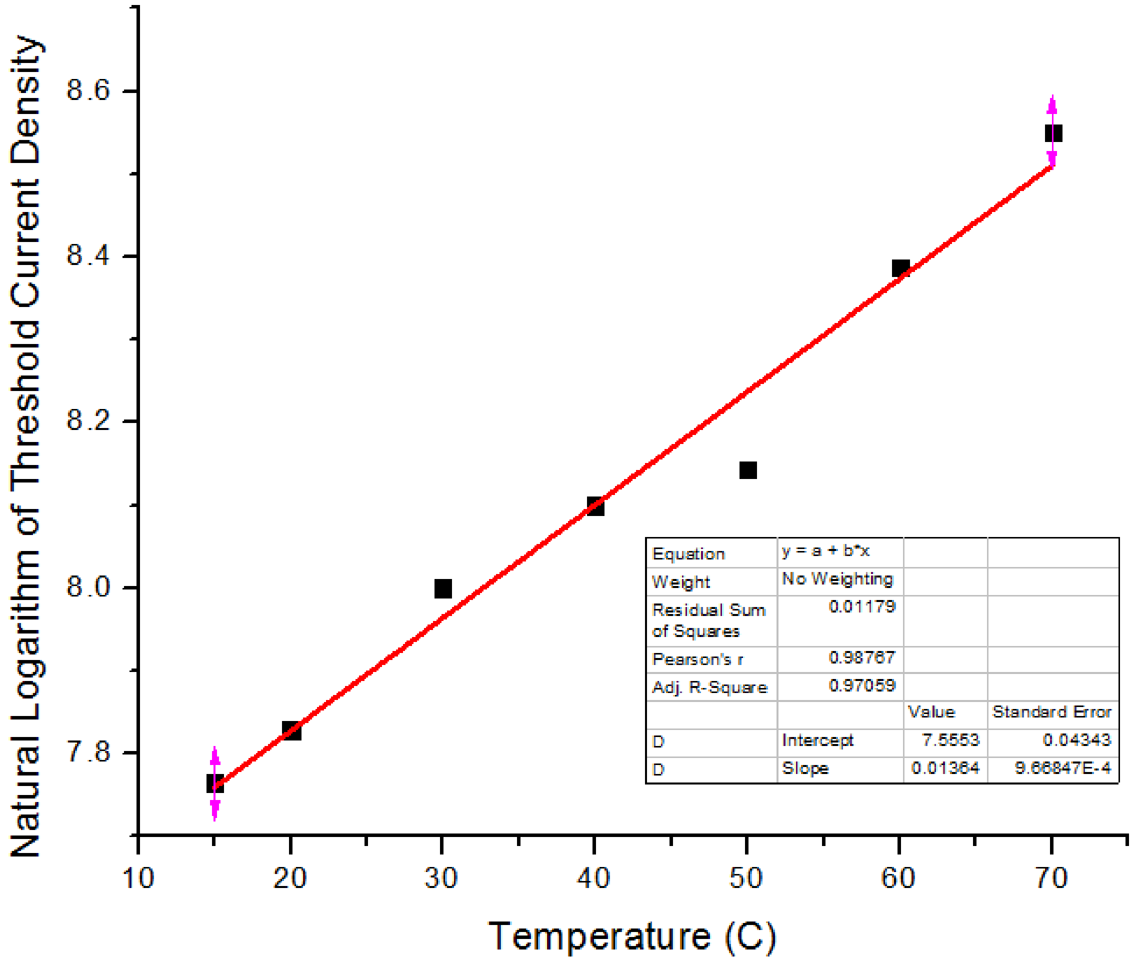

Equation	y = a + b*x		
Weight	No Weighting		
Residual Sum of Squares	0.01179		
Pearson's r	0.98767		
Adj. R-Square	0.97059		
		Value	Standard Error
D	Intercept	7.5553	0.04343
D	Slope	0.01364	9.66847E-4

Figure 3.21: Natural logarithm of the extracted threshold current densities of the 4 µm × 1600 µm laser as a function of temperature.

3.5 Emission Bandwidth

The most attractive part in chirping these QDash lasers is their dash size inhomogeneity that can be categorized into two types:

1. Intra-plane inhomogeneity; by the virtue of the variant heights of the individual QDashes within each dash ensemble as a result of the inherent random nature of their growth process.

2. Inter-plane inhomogeneity; in the form of the variant average QDash height between the different dash stacks, *i.e.* S20, S15, S10a, and S10b.

Ultimately, such inhomogeneity leads to dissimilar emission wavelengths that collectively yields in an ultra-broad emission.

The emission spectra of multiple of laser diodes at different cavity lengths have been acquired via an optical spectrum analyzer while fixing the ridge width to 4 µm. Figures 3.22 (a) – (d) show the progressive emission spectra of 4 µm ridge devices of cavity lengths of 500 µm, 700 µm, 800 µm, and 1100 µm, respectively, while Figures 3.23 (a) – (d) show the spectra of the 1600 µm, 2000 µm, 2800 µm, and 3000 µm cavity lengths, respectively. In both figures, the spectra are shown at five different current injections equivalent the first five multiples of their associated threshold current densities, *i.e.* 1 I_{th} – 5 I_{th} in steps 1 I_{th}. Each spectrum shows the relative intensity in logarithmic arbitrary units (a.u.) at different wavelength values between 1580 nm and 1650 nm.

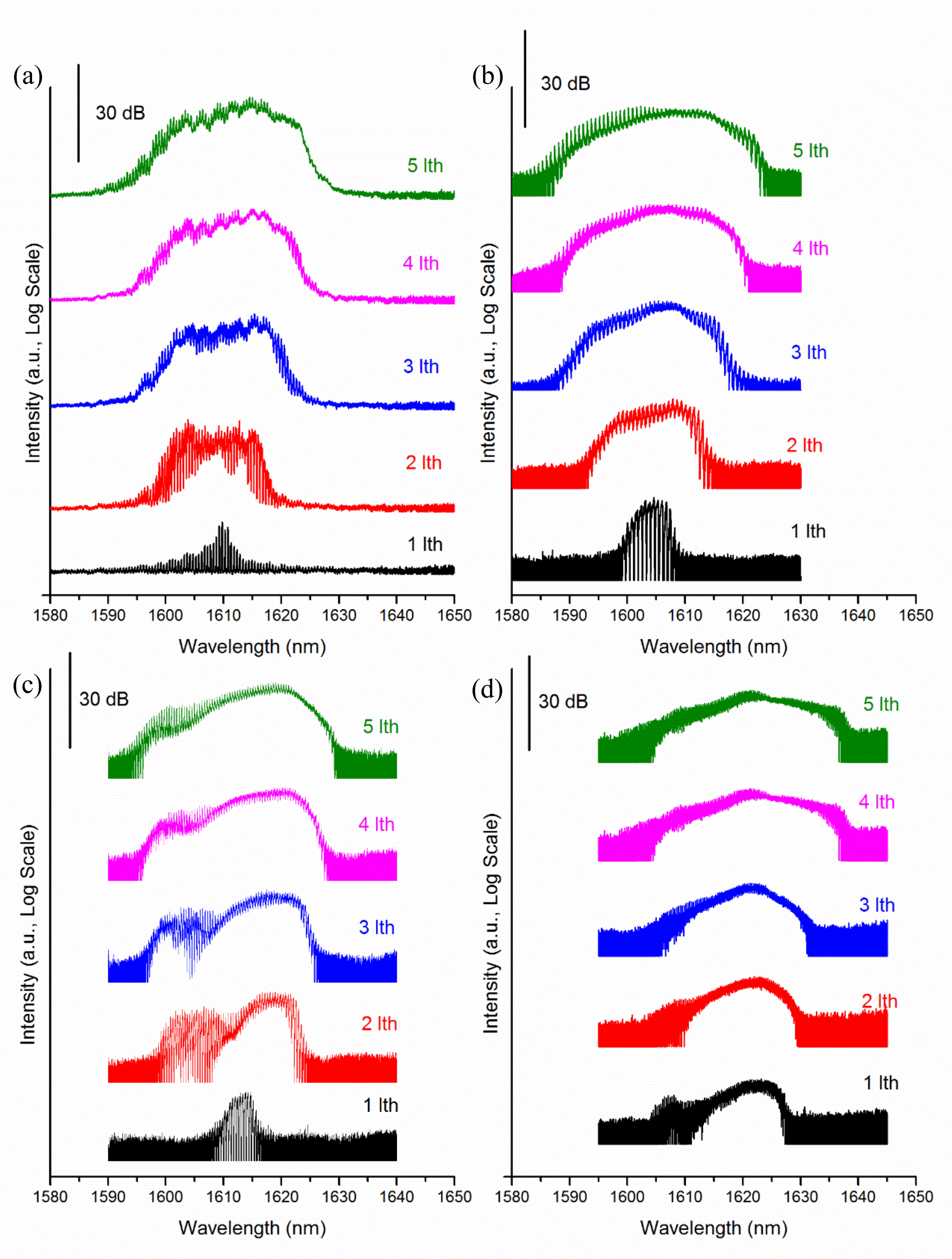

Figure 3.22: The progressive emission spectra of 4 µm ridge devices of cavity lengths of (a) 500 µm, (b) 700 µm, (c) 800 µm, and (d) 1100 µm, respectively, at five different current injections (1 Ith – 5 Ith in steps of 1 Ith).

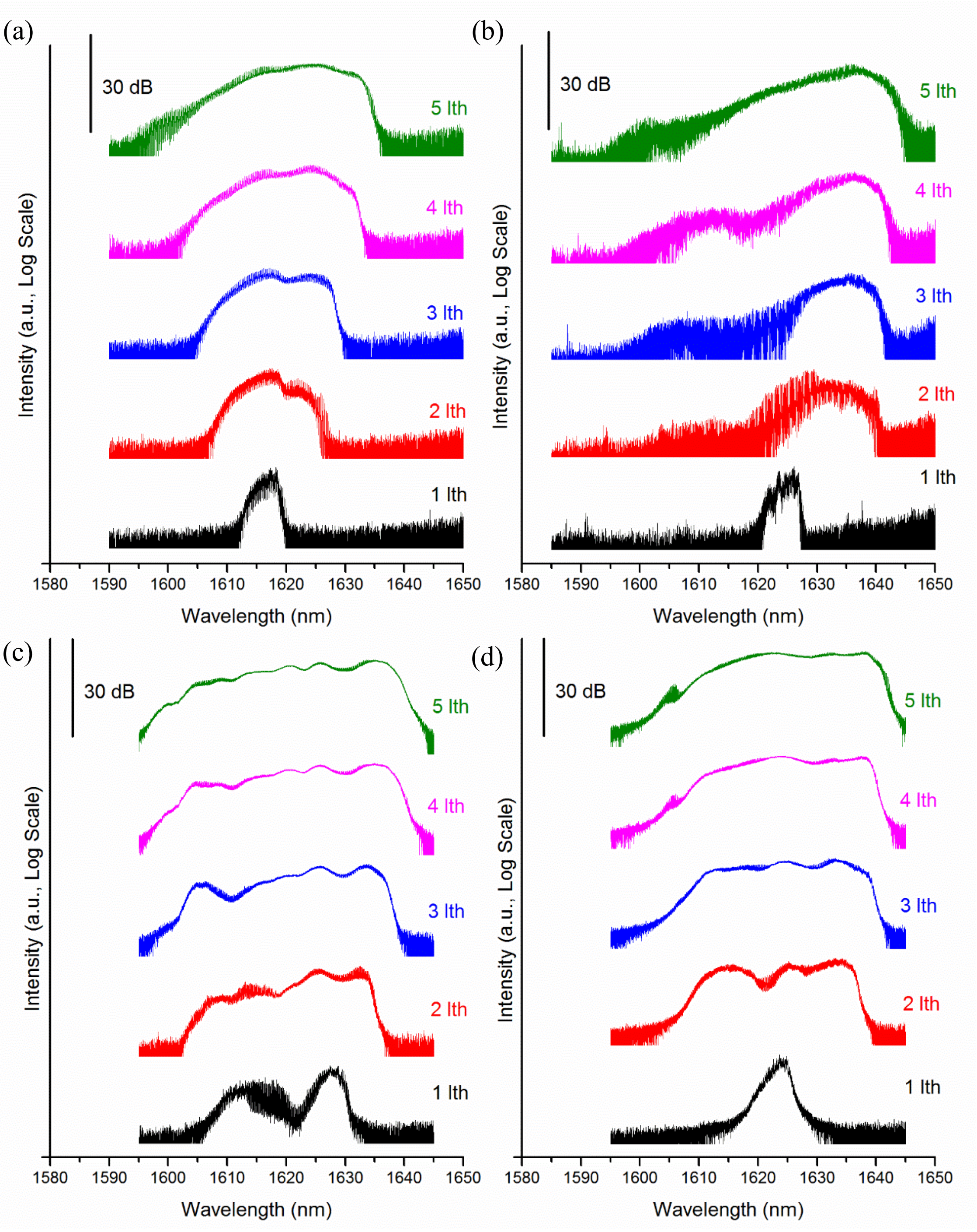

Figure 3.23: The progressive emission spectra of 4 µm ridge devices of cavity lengths of (a) 1600 µm, (b) 2000 µm, (c) 2800 µm, and (d) 3000 µm, respectively, at five different current injections (1 Ith – 5 Ith in steps of 1 Ith).

Although ultra-broad emission is observed from all cavity length these lasers, three among them showed better broadband profiles than the others. The first device is the 700 µm long laser whose close-up emission spectrum (at injection current of 5 I_{th}), shown in Figure 3.24, reached a wide emission of a 3dB bandwidth of ~ 15.5 nm with a signal-to-noise ratio (SNR) of ~ 20dB and an emission coverage of ~ 38.4 nm which can be translated into 2.37 THz and 4.41 THz respectively according to

$$\Delta f = \frac{c}{\lambda^2}\Delta\lambda \tag{3.9}$$

where

- Δf is the frequency bandwidth in Hz.
- c is the free-space speed if light.
- λ is the centeral wavelength.
- $\Delta\lambda$ is the wavelength bandwidth.

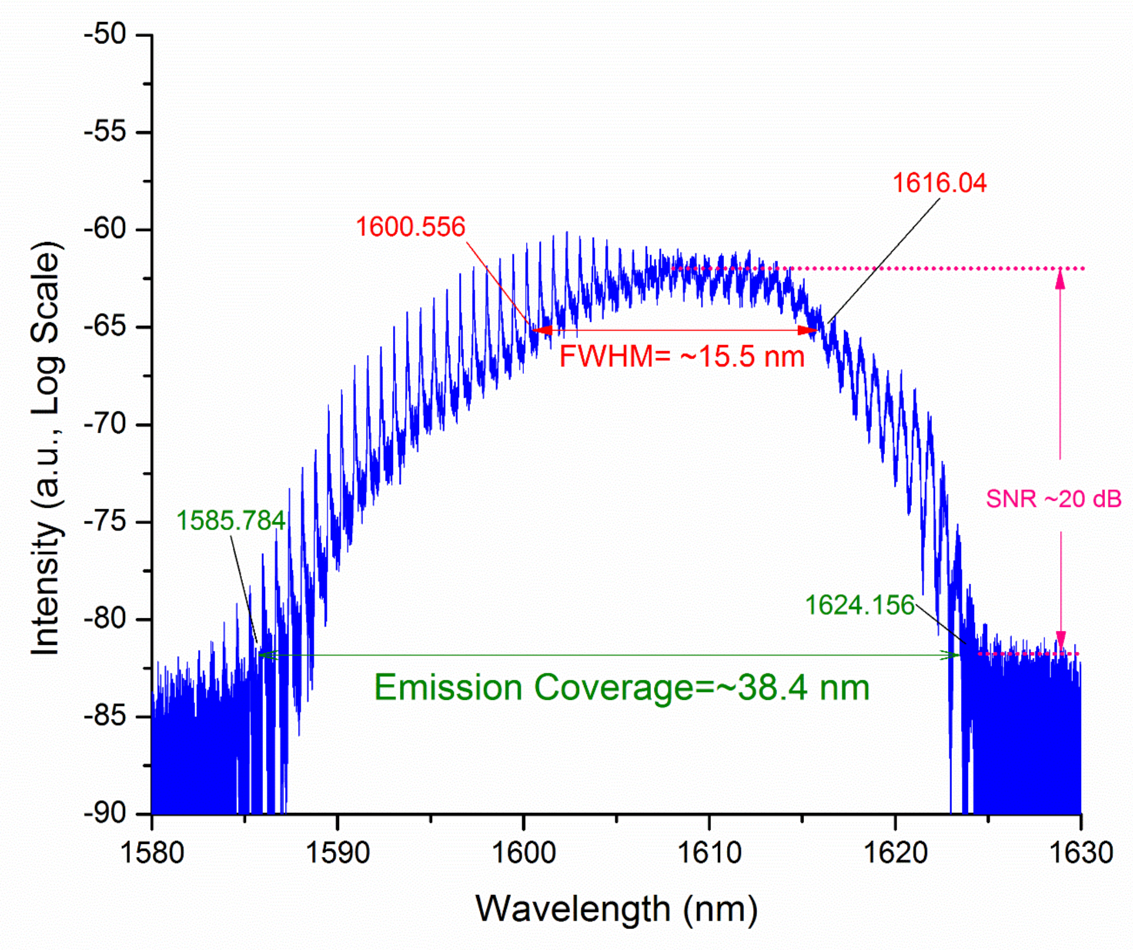

Figure 3.24: A close up emission spectrum of the 4 µm × 700 µm showing an ultra-broad emission.

The 3000 µm long laser showed a wide emission of a 3dB bandwidth of ~ 20.73 nm ≡ 2.37 THz. Moreover, the 2800 µm cavity long achieved an even broader emission with a 3dB bandwidth of ~ 30.36 nm ≡ 3.47 THz. In chapter 5, we thoroughly describe the lasing spectral profiles in greater detail.

CHAPTER 4

HIGHER DUTY CYCLE LASING CHARACTERISTICS

In the previous chapter, the characterization of the QDash laser diodes has been carried over under SPW operation with a duty cycle of 0.2%. The reasoning behind such decision was due to the fact that these chirped QDash lasers are still novel structures that had been grown as exploratory research-based specimens. As a result, different parameters and operations involved in their growth process had not been yet fully optimized. Consequently, longer exposure to more carrier influx, during higher duty cycle operations or during continuous wave (CW) operation, results in diminishing the lasing performance of these devices and possibly damaging them entirely. Nevertheless, characterizing these specimens under SPW gives a very close estimate of their expected performance when they are better growth-optimized.

However, in order for these lasers to be used in optical communication systems, operating under SPW becomes obsolete since the output optical average power plays a vital role in successful modulation, transmission and detection of the optical signal. Hence, exploration of higher duty cycle operations becomes necessary as we move forward. Moreover, in general, an external continuous optical modulation necessitates a CW operation of the optical sources used to ensure easy successful modulation of the continuous data bit-stream.

In this chapter, we firstly investigate the performance of the chirped QDash lasers under higher duty cycle SPW and then under CW operations in terms of their characteristic parameters and emission spectral profiles.

4.1 Higher Duty Cycle SPW Operation

4.1.1 Lasing Characteristics

In order to investigate the impact of operation under higher duty cycles, a 4 µm × 1600 µm QDash laser diode has been tested using injection current pulses of different duty cycles, namely 0.2%, 0.5%, 1%, 2%, 3%, and 4%, with a fixed delay width of 250 µs. Figure 4.1 shows the extracted L-I characteristic curve under these duty cycles. From the figure, we observe that the threshold current did not change for different duty cycle operations while, at high current injections, a progressive reduction in the slope efficiency (thereby external quantum efficiency) is observed.

Such observation can be attributed to the non-optimized nature of the growth of the active region as stated previously. This results in higher non-radiative recombination centers due to the accelerated rise in temperature. Besides, built-up heat due to the associated high thermal resistance in such non-optimized structures compared to better optimized ones as demonstrated in [68] renders the heat incapable to dissipate into the substrate fast enough and leads to deteriorated performance of the device. Hence, as discussed before, the resulting temperature rise results in introducing more losses in the active region in the form of phonon generation due to lattice vibrations.

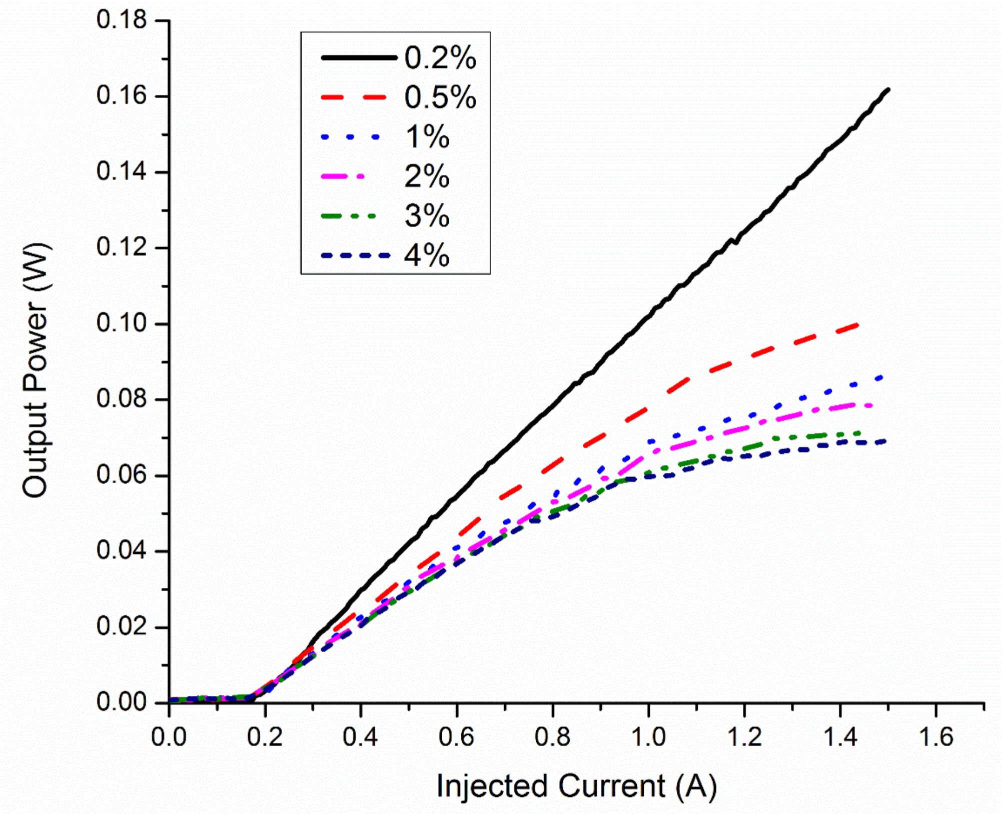

Figure 4.1: L-I characteristic curve of the 4 µm × 1600 µm laser diodes under different duty cycle operations.

On the other hand, the consistency of the threshold current for different duty cycle operations is due to the low values of I_{th} that causes minimal heat generation and conserve the integrity of the structure which is contrary to higher current injections. Hence, this behavior agrees with our attribution of the performance degradation to the buildup heat and further validates our use of SPW to estimate the performance of CW operation mode when the growth process is optimized.

The L-I curve in each case in Figure 4.1 exhibits optical power rollover at earlier current injections when the duty cycle increases. Figure 4.2 shows the effect of operation under higher duty cycles on the slope efficiency of the chirped QDash 1600 µm laser diode in addition to the pumping current value at which the output power rolls over (slope is reduce by 50%). The duty cycle is denoted as D_c in the figure.

Approximately 30% reduction is observed in the slope efficiency (external quantum efficiency) as the duty cycle is increased from 0.2% to 4%. More interestingly, both the onset roll over current and slope efficiency witness an identical simultaneous response to increasing the duty cycle, following an exponential decay.

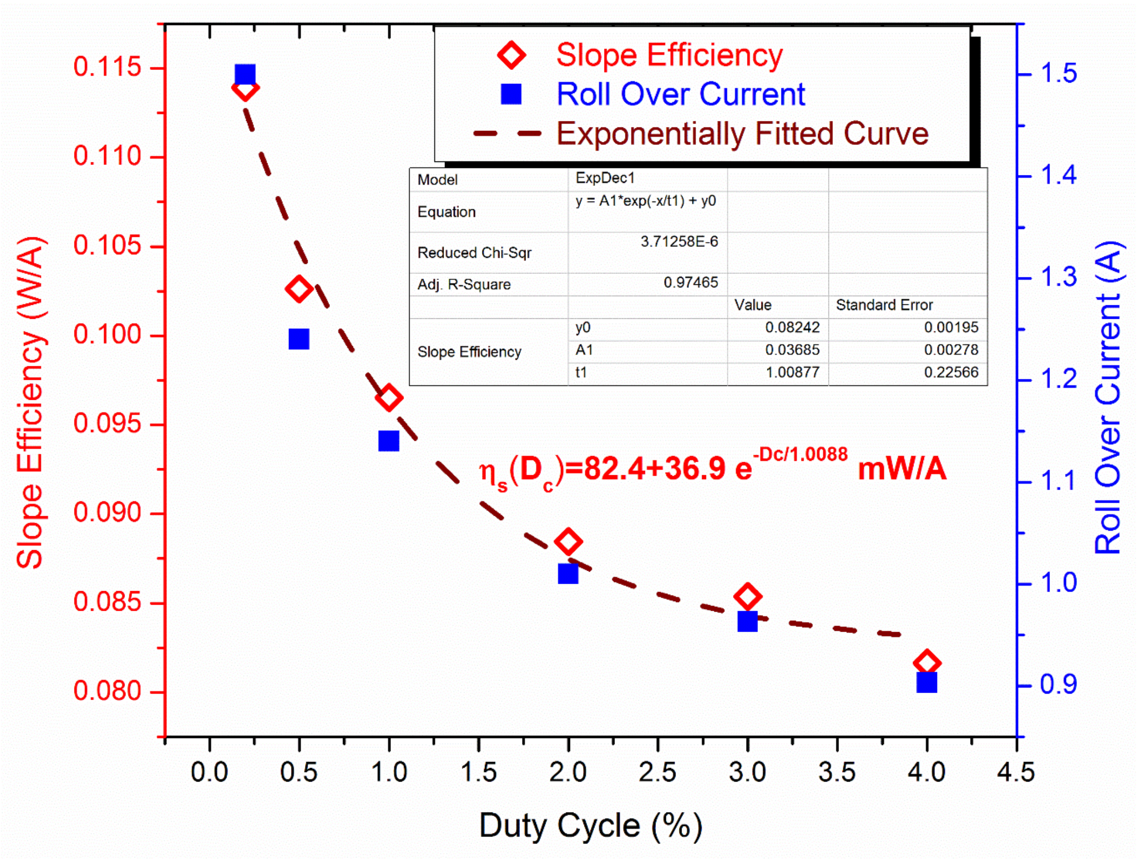

Figure 4.2: Slope efficiency and rollover initial injection current as functions of the duty cycle.

The dashed curve in Figure 4.2 is the exponentially fitted slope efficiency values at different duty cycles. The equation of the fitted curve, according to the extracted parameters from the inset table in Figure 4.2, is

$$\eta_s(D_c) = 82.4 + 36.9\ e^{-D_c/1.0088}\ mW/A \tag{4.1}$$

where

- η_s is the slope efficiency.

- D_c is the operation duty cycle.

4.1.2 Peak Power and Average Power

The vertical axis of an L-I curve shows the instantaneous peak power for different injection current values. However, rather than the value of the instantaneous peak power, detection of the light emission depends on the average power of the laser emission. Figure 4.3 shows an arbitrary pulse train of period T with a peak power P_{peak} spanning over Δt amount of time.

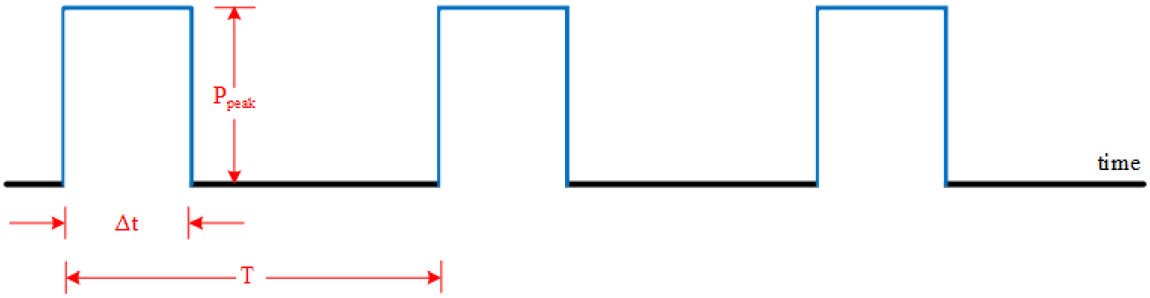

Figure 4.3: An illustration of a train of pulses each occupying Δt amount of time with a T period.

Given that each pulse corresponds to energy E, we can relate the peak power over Δt with the integrated average power per time period, that corresponds to the same amount of energy, by

$$P_{peak}\,\Delta t = P_{average}T \tag{4.2}$$

$$Duty\ Cycle \equiv \frac{\Delta t}{T} = \frac{P_{average}}{P_{peak}} \tag{4.3}$$

$$P_{average} = P_{peak} \times Duty\ Cycle \tag{4.4}$$

Figure 4.4 shows both the peak optical power, extracted from Figure 4.1, alongside the corresponding integrated average power according to (4.4) as functions of the duty cycle.

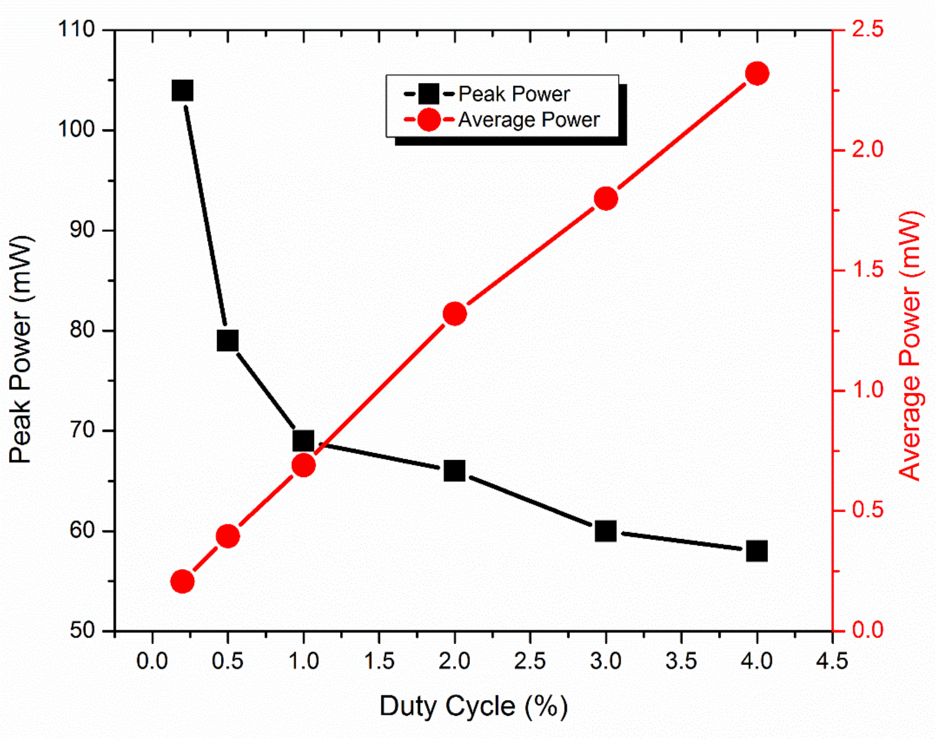

Figure 4.4: The variation of the peak power and the average power as functions of the operation duty cycle.

Figure 4.4 shows that at duty cycles 0.2% and 4%, the peak power exhibits about 46% reduction in the optical peak power from ~104 mW to ~58 mW. However, it is interesting to note that as the pulse width is increased, the total average power increases at a rate that outweighs the reduction of the peak power resulting ultimately in a net integrated average power increase of approximately ten folds from 0.207 mW to 2.32 mW as the pulse width increases by 20 folds between 0.2% and 4% duty cycles.

4.1.3 Emission Spectra

The emission spectra of the 4 µm by 1600 um cavity length QDash laser diode are shown in Figure 4.5 for the different duty cycles at a current injection of 1.0 A which is about 5 I_{th}. The peak power, denoted as P_p and integrated average power, denoted as P_a) are shown for each duty cycle. In addition, the dotted lines outline the emission wavelength coverage while the dashed line traces the emission central wavelength for each case. There are few observations that can be inferred from Figure 4.5, as the duty is increased from 0.2% to 4%,

- A small redshift that is observed in the emission central wavelength from ~1619.5 nm to ~1625 nm.

- An overall emission wavelength coverage enhancement of ~38% and a FWHM increase from 17 nm to 28 nm when the duty cycle is increased from 0.2% to 4%.

- A quenching of the quantum efficiency in the form of spectral power density reduction displayed by a 13 dB in the SNR due to the increase of the duty cycle from 0.2% (27 dB) to 4% (14 dB).

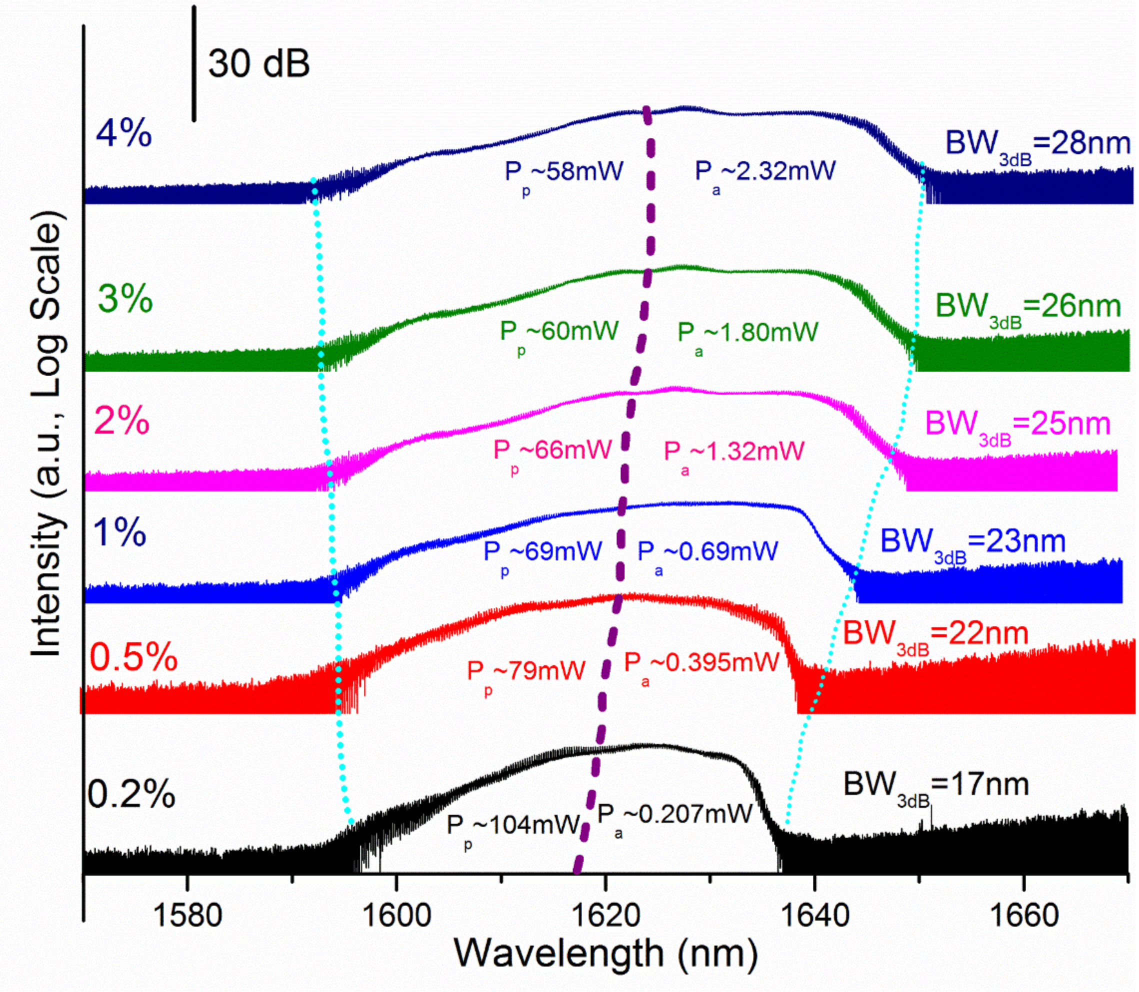

Figure 4.5: The emission spectra under different duty cycle operations showing the peak and average power in each case. The cyan dotted lines outline the emission wavelength covereage while the purple dashed line traces the cenral emission wavelength for each case.

These observations are signature effects of temperature rise within the active medium of the laser diodes. In the next chapter we go in more depth in analyzing these effects. Figure 4.6 shows the effect of the duty cycle on the SNR, wavelength coverage and central wavelength of the emission spectra that were presented in Figure 4.5.

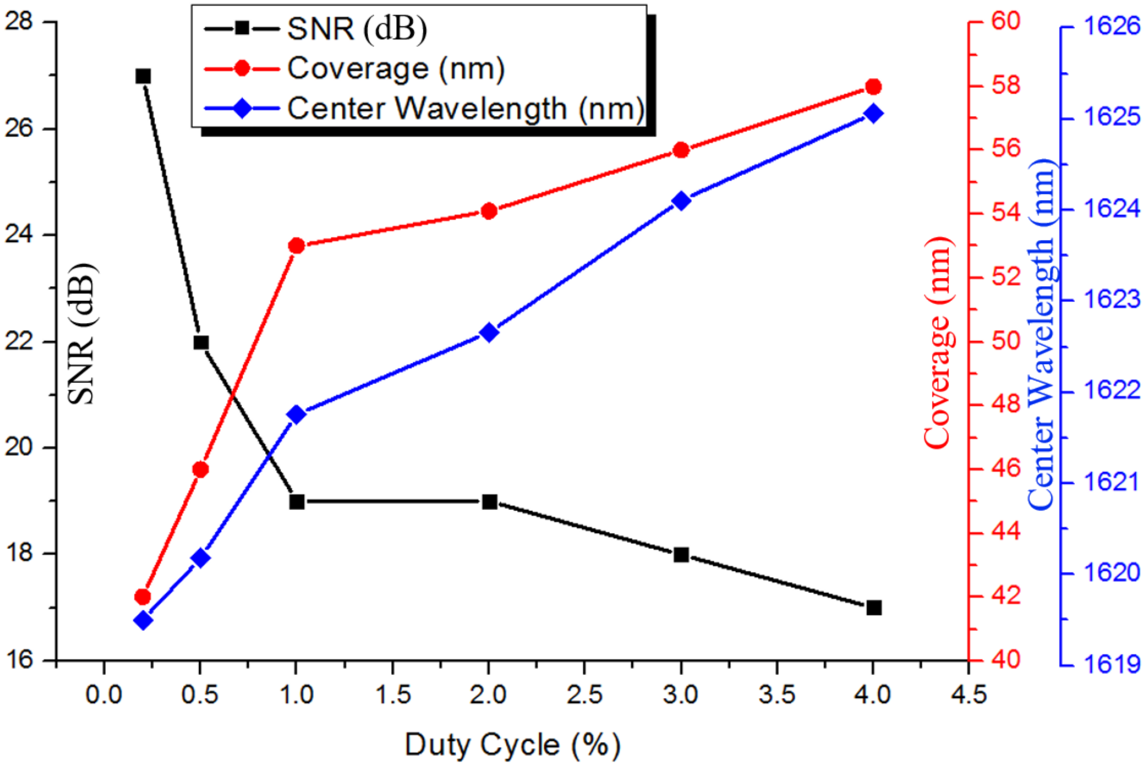

Figure 4.6: The variation of the SNR, wavelength coverage, and central wavelength of the emission spectra as functions of the duty cycle.

4.2 CW Mode Operation

As discussed in the introduction of this chapter, for a continuously generated bit stream, the laser optical emission acting as a carrier signal of the system should be operating in CW for easy and successful modulation. In the following, we examine the performance of lasing under CW mode.

4.2.1 Thermionic Enhancement

So far, the junction temperature rise within the active medium, whether it be via high current injections or as the duty cycle is increased, has been associated with deteriorating the performance of the laser diode. However, appropriate values of temperature has the potential to enhance the photon generation processes due to the fact that the density of free carriers within semiconductor devices is a function of energy and temperature according to [69]

$$dn(E,T) = f_D(E,T)g(E)dE \tag{4.5}$$

where

- dn is the number of electrons occupying energies between E and dE.
- $g(E)$ is the DOS.
- $f_D(E,T)$ is the Fermi-Dirac distribution given as

$$f_D = \frac{1}{1 + \exp(\frac{E - \mu}{K_B T})} \tag{4.6}$$

where

- μ is the chemical potential that results in an occupation probability of 1/2 at the Fermi level.

- K_B is the Boltzmann's constant that is equal to 1.380×10^{-23} J/K.

- T is the absolute temperature.

4.2.2 CW L-I Characteristics

Due to the non-optimized growth of these structures, their operation under CW mode has been observed to be extremely unstable due to the exceedingly high amount of generated losses under high continuous influx of supplied carriers in CW mode. Therefore, the generated optical power in each case witnesses steep plunge in a very short periods of time. Hence, the acquisition of the real transient peak optical power becomes not viably possible. Therefore, extracting power dependent parameters, *e.g.* slope, internal, and external quantum efficiencies, becomes difficult from these CW measurements. However, by normalizing the detected optical power throughout the different cases, other parameters are still conserved such as transparency current density and the relative general degradation in the quantum efficiencies. Figure 4.7 shows the normalized L-I characteristic curves of different 5 µm wide ridge laser diodes of different cavity length (500, 800, 1100, 1600, and 3000 um).

As a result of the lower threshold gain in longer cavity devices, a reduction in the slope of the optical power curve is observed when compared to shorter cavities, much like the previously discussed behavior in SPW mode. On the other hand, due to the fact that more QDashes exist in longer cavities, long devices are able to sustain stimulated emission for wider spans of current injections. This can observed in Figure 4.7 by the fact that longer laser devices exhibit wider L-I curves and higher roll over currents when compared to shorter devices. In addition, this might also be attributed to the possible different degrees of heat dissipation from the active region as a function of the cavity length.

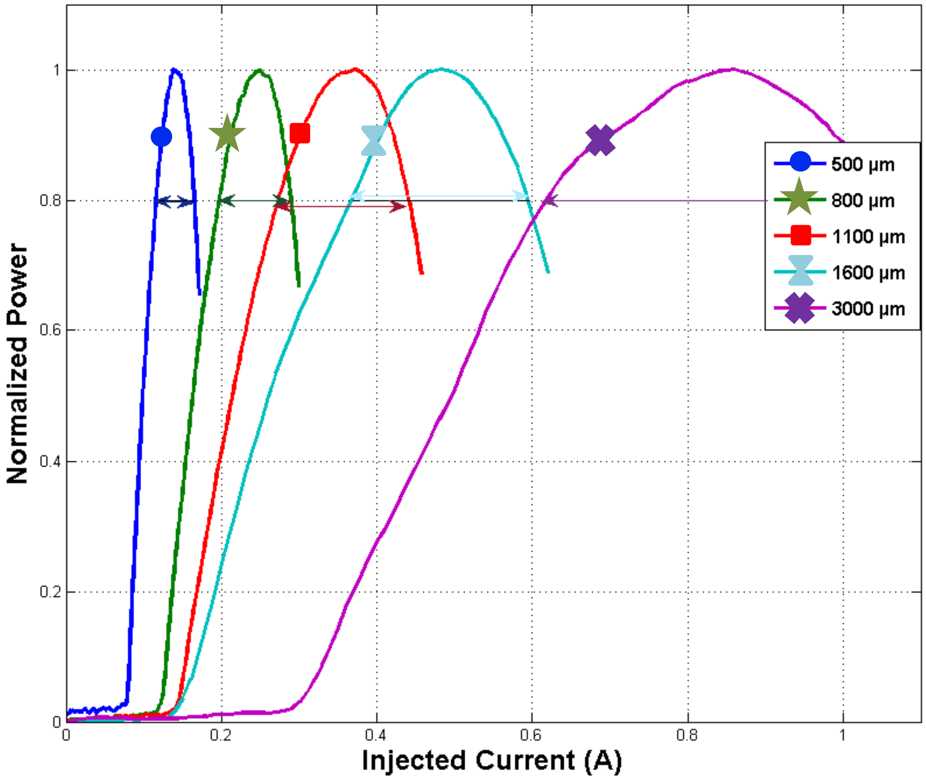

Figure 4.7: Normalized CW L-I characteristic curves of different 4 µm ridge width laser diodes of different cavity lengths (500, 800, 1100, 1600, and 3000 um).

Figure 4.8 shows a comparison between the CW and SPW (0.2% duty cycle) L-I curves of this device which demonstrates the impact of operating under CW mode. In this mode, stimulated emission only occurs for a sort range of injection currents (from 0.18 A to 0.71 A) outside which, spontaneous emission is dominant as evident by the flat optical output power at these current values.

The increase in the optical power of the spontaneous emission in CW mode, when compared to SPW mode, can be attributed to the thermionic enhancement effect associated with the temperature rise due to the continuous current injection which results in charge carriers' acquisition of thermal energy that is equal to $K_B T$ leading to more carrier transitions and higher electron occupancy in the conduction band.

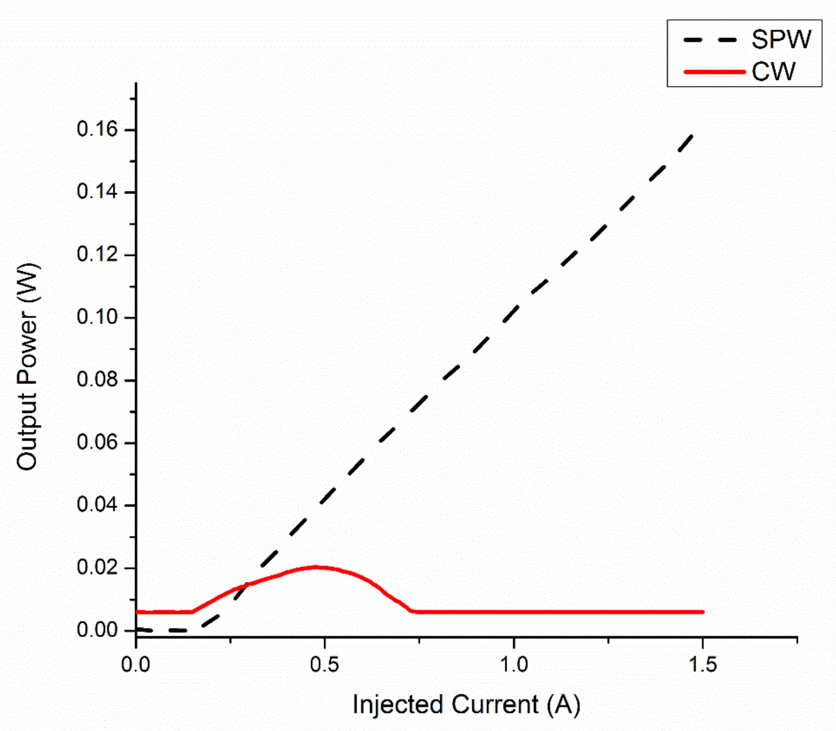

Figure 4.8: Comparison between the L-I curves operating under SPW and CW modes.

From Figure 4.7 and Figure 4.8, we observe that the threshold current values of the different laser devices are lower in CW mode when compared to their operation in the different SPW modes which indicates earlier lasing occurrences. This behavior has been observed in all examined laser devices. In CW mode, the reasonable junction temperature rise at low current injections ($< I_{th}$) introduces more carrier transitions by the virtue of the shortly discussed thermionic emission resulting in quicker achievement of population inversion and ultimately earlier stimulated emission. Moreover, Figure 4.9 demonstrates the overall small ~7% reduction of the extracted transparency current density in CW mode (~ 2024 A/cm^2) when compared to the extracted J_o under 0.2% SPW operation (~ 2183 A/cm^2) for the same ridge width.

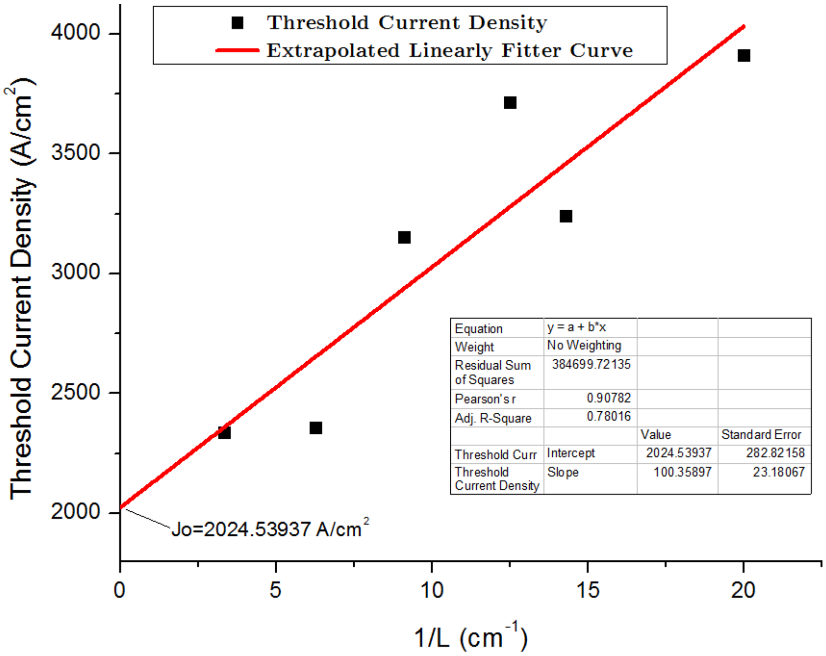

Equation	y = a + b*x		
Weight	No Weighting		
Residual Sum of Squares	384699.72135		
Pearson's r	0.90782		
Adj. R-Square	0.78016		
		Value	Standard Error
Threshold Curr	Intercept	2024.53937	282.82158
Threshold Current Density	Slope	100.35897	23.18067

Figure 4.9: Extrapolated liner fit of the threshold current densities as a function of the inverse of the cavity length in order to extrapolate Jo.

4.2.3 CW Characteristic Temperature

In order to find the characteristic temperature of the QDash laser under CW operation, we found the normalized L-I characteristic curves at different temperatures (15, 20, 30, 40, 50, and 60° C) as shown in Figure 4.10.

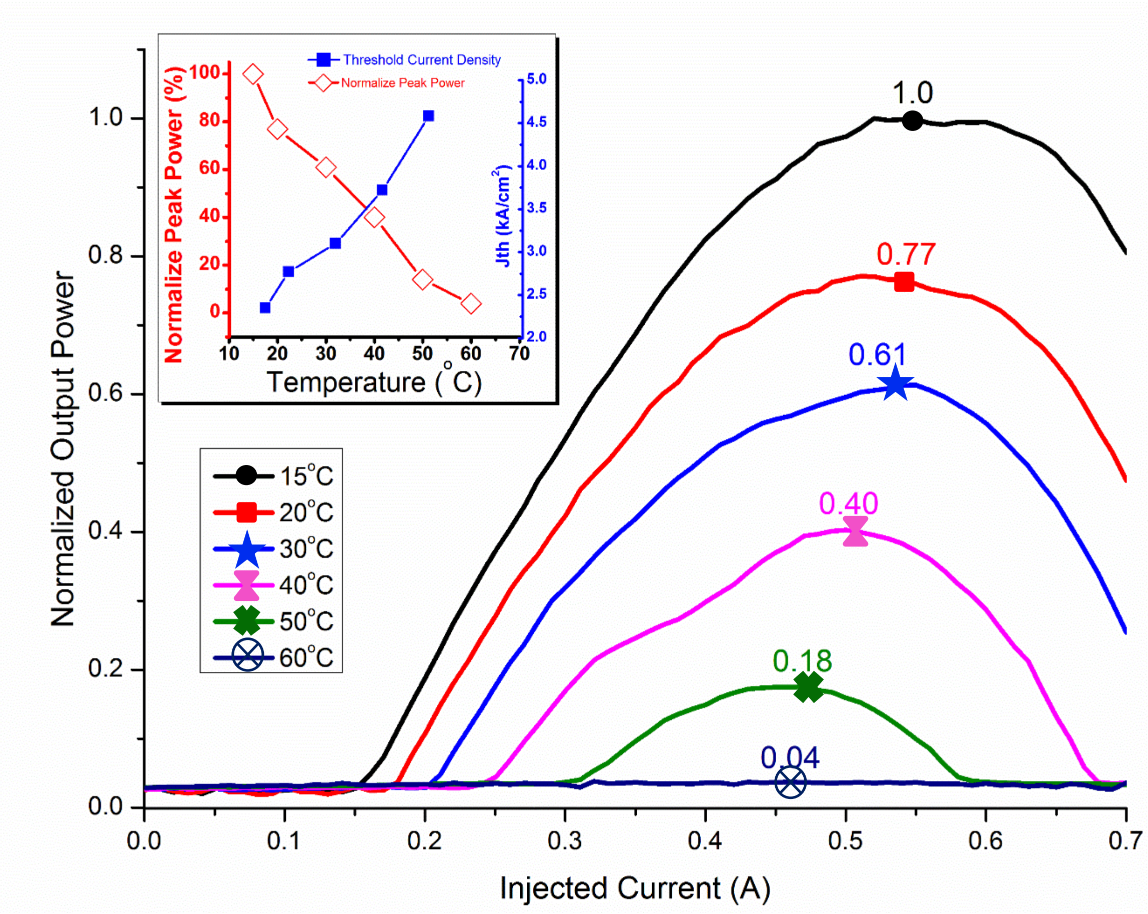

Figure 4.10: Normalized CW L-I characteristics under different temperatures (15, 20, 30, 40, 50, and 60°C). The maximum normalized power is shown over each curve. The inset shows the reduction of the normalized peak power and the increase in the threshold current density as functions of the temperature.

The inset of the figure shows the increase in the threshold current density and the reduction of the normalized peak power as functions of temperature. As observed from the figure, raising the temperature shows a detrimental impact on the lasing characteristics under CW that exceeds that of SPW mode which is shown in Figure 3.19. The impact of raising the temperature is most apparent in the figure in the case of 60^{o} C temperature beyond which the laser ceases to operate in stimulated emission while the spontaneous emission dominates the optical output. As discussed in the previous chapter, high characteristic temperature values indicate more stability and consistency of the performance of the laser diode against rising temperatures. The slope of the linearly fitted curves in Figure 4.11 denotes the reciprocal of the characteristic temperatures for this device under SPW and CW modes. Nevertheless, the characteristic temperature is equal to 56^{o} K in CW mode while it was found to be 73^{o} K in SPW as previously demonstrated. This gap in the characteristic temperature between both operation modes further assures our previous discussion of the CW mode being very sensitive to temperature variations which is evident as the threshold current in both cases are reasonably close at lower temperatures and diverge from each other as the temperature is raised as shown in Figure 4.11.

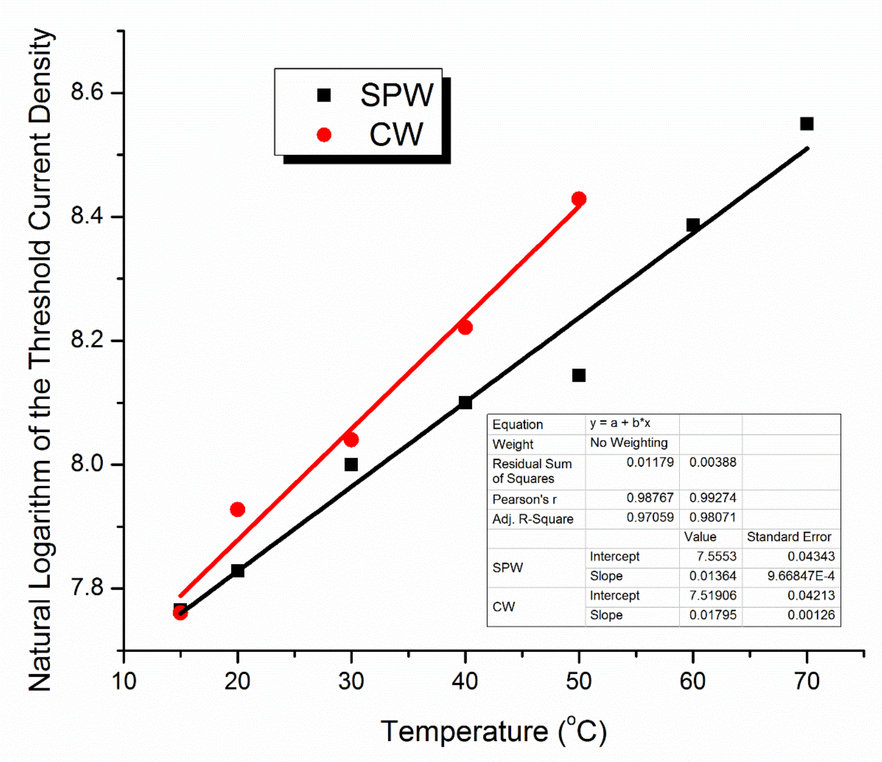

Equation	y = a + b*x		
Weight	No Weighting		
Residual Sum of Squares	0.01179	0.00388	
Pearson's r	0.98767	0.99274	
Adj. R-Square	0.97059	0.98071	
		Value	Standard Error
SPW	Intercept	7.5553	0.04343
	Slope	0.01364	9.66847E-4
CW	Intercept	7.51906	0.04213
	Slope	0.01795	0.00126

Figure 4.11: Linearly fitted values of the natural logarithm of the threshold current densities as functions of temperature for SPW and CW operation modes. The slope of each line denotes the reciprocal of the characteristic temperature in each case.

4.2.4 CW Lasing Spectral Profiles

As previously stated, CW emission from these sub-optimally grown devices is highly unstable. The lasing behavior in all the examined QDash laser didoes can be classified as:

- Devices that lase in CW very briefly then quickly die out leading to spontaneous emission overtaking the stimulated emission. This behavior was observed in the majority of the devices.

- Devices that do not lase at all in the CW mode.
- Devices that lase in CW consistently for long periods of time. Only four devices displayed such behavior with cavity lengths of 700 µm, 800 µm, 1100 µm, and 1600 µm.

Figure 4.12 shows the emission spectrum of the 4 µm × 800 µm QDash laser device under SPW and CW modes at a current injection of ~ 2 I_{th} for both cases. The first observation in CW mode is that the spontaneous emission (regions outside of the outline window in the figure) possesses much more power when compared to SPW which agrees with the optical power offset shown in the L-I characteristic curve shown in Figure 4.8.

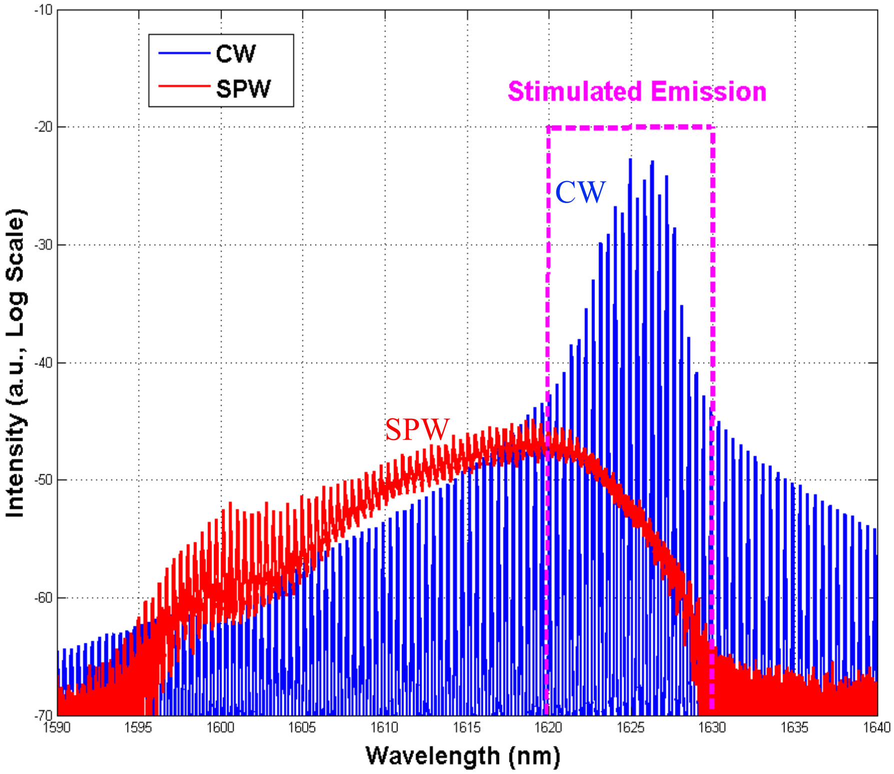

Figure 4.12: Emission spectra of a 4 µm × 800 µm laser diode at a current injection of 2 I_{th} for both SPW and CW operation modes.

More interestingly, while thermionic emission has been demonstrated to broaden the emission at higher order SPW according to (4.5), CW on the other hand results in a severe reduction on the emission bandwidth. Ultimately, in a well optimized laser structure, both emissions of SPW and CW should be very close to each other. However, in this case, only the longest wavelength (lowest energy) components of emission of SPW are present in the CW's emission as outlined by the magenta dashed window in Figure 4.12 between 1620 nm and 1630 nm. As stated in the previous chapter, according to (3.1), dashes of larger heights are responsible for longer wavelength emissions as they tend to result in smaller bandgaps and lower energy transitions (longer wavelength) in addition to having tighter and deeper quantum confinement as illustrated in Figure 3.3. As a result, the presence of the lowest energy emissions exclusively in Figure 4.12 strongly suggests that the exceedingly high temperature rise in the CW mode results in carrier acquisition of high thermal energies that leads to carrier leakage (spillover) from the potential of the shallow-offset QDash ensembles (S20 and S15) while the deeper S10 QDash family is still reasonably confined. Nevertheless, as the injection current is slightly increased (~2.1 I_{th}) the thermal energy enables the carriers within the stack (S10) to break confinement and the stimulated emission to entirely disappear as shown in Figure 4.13.

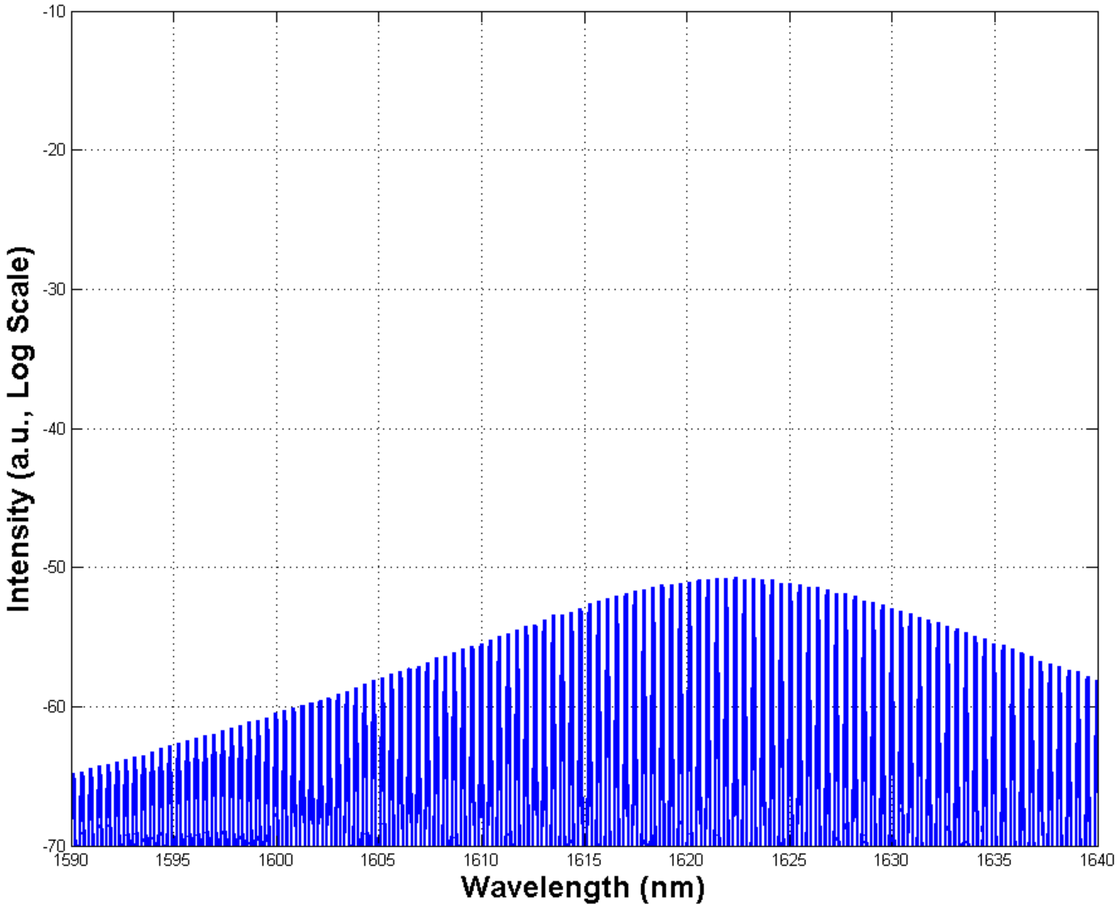

Figure 4.13: Spontaneous emission at current injection of ∼2.1 I_{th}.

CHAPTER 5

TEMPERATURE DEPENDENT LASING CHARACTERISITCS

From the previous chapter, we have observed that temperature rise within the QDash laser plays a very vital role in most of the carrier distribution and transition processes that take place within the active medium whether the temperature is directly increased or indirectly increased via the heat buildup in the active region resulting from current injections and higher order operation modes. In this chapter, we characterize the temperature dependent lasing emission of the chirped multi-stacked Qdash lasers and investigate the effect of varying the temperature and geometrical dimensions on their spectral profiles. The temperature dependent lasing spectra have been investigated for two device configuration. The first case was for index-guided ridge laser diodes of three different ridge width values, namely 2 µm, 3 µm and 4 µm. Secondly, a gain-guided broad area laser diode with a wide oxide-strip of 15 µm was investigated.

5.1 Ridge Devices

5.1.1 2 µm ridge Devices

Figures 5.1 (a)–(d) show the lasing spectra of a 2 µm × 700 µm chirped Qdash ridge-waveguide laser at varying current injections under different temperatures, namely 15° C, 20° C (room temperature), 30° C, and 40° C, respectively. Starting from 1.0 I_{th}, the current is swept from 1.2 I_{th} to 8.2 I_{th} in steps of 0.4 I_{th}.

The emission from this device at room temperature shows an ultra-broad emission from this device at room temperature that reached a −3dB bandwidth of 45 nm as shown in Figure 5.1(b) at current injection of 8.2 I_{th}. This peculiar broadening effect has been attributed to the exceeding inhomogeneity resulting from chirping the structure by the virtue of dissimilar barrier layer thickness values which was proven to have a distinct effect on the enhancement the emission −3 dB bandwidth.

At early current injections (below 4 Ith), a single lobe is witnessed centered around 1616 nm. The lasing is initiated from the Qdash ensemble S15 containing the dashes of the intermediate average height that constitute the largest number of available dashes in the structure. Moreover, tails of the excited energy states of other QDash stacks overlap with the ground state of S15. As a result, they are expected to be the first to overcome the losses of the medium.

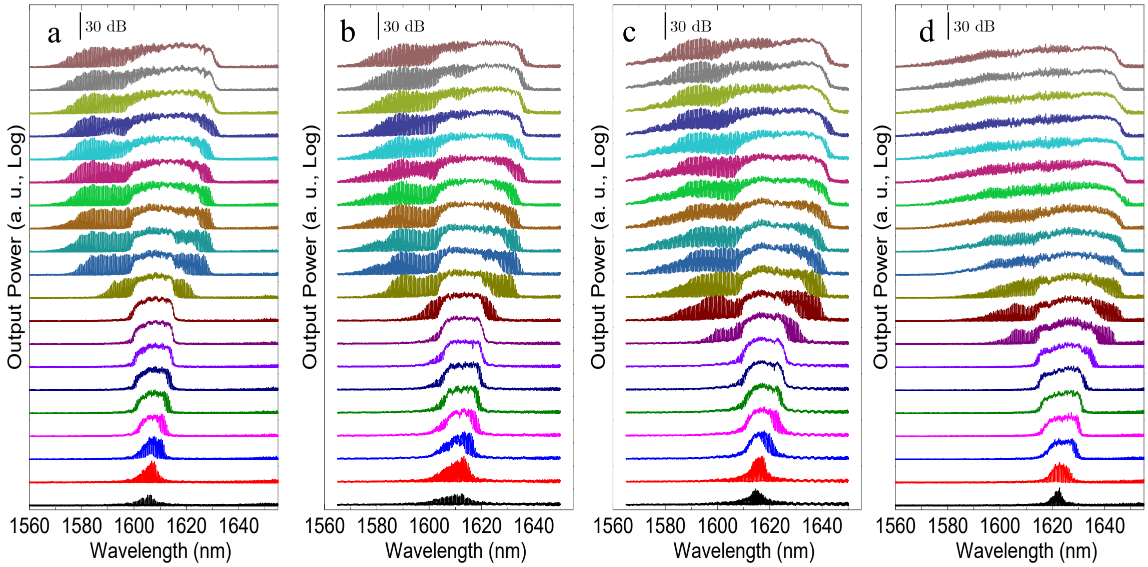

Figure 5.1: Lasing spectra of 2 µm × 700 µm chirped Qdash ridge-waveguide laser at varying current injections ($1.0I_{th}$, 1.2 - $8.2I_{th}$ in steps of $0.4I_{th}$) at different temperatures (from left to right) (a) 15°C, (b) 20°C (room temperature), (c) 30°C, and (d) 40°.

Multiple studies support this observation as they have demonstrated that in such structures with overlapping quasi-dimensionless density of states, the lasing is initialized from the intermediate average height dashes [70]. However, as more current is being pumped, more QDashes, in the S15 and overlapping tails energy states from other stacks, are able to achieve population inversion resulting in emission broadening as more current is being injected. In addition to the emission broadening, a small red shift is witnessed by the center of the spectra. In more quantum-efficient structures, such as QDots, early current pumping causes a blue shift in the emission as a result of the overlap between the excited energy tails of the smaller dots and the ground states of the larger dots making the excited carriers from the smaller dots able to fit into higher energy states of the larger dots resulting in a blue shift in the emission [71]. Nevertheless, the effect of the generated high rise in the junction temperature of the QDash laser diode in the form of bandgap shrinkage exceeds that of the overlapping energy states resulting in a net red shift as seen in Figure 5.1(b). This is probably a direct result of the lower quantum efficiency associated with exceedingly high inhomogeneous structures, as demonstrated in [72], as a result of their high thermal resistivity that results in heat buildup that ultimately deteriorates the performance of the device as more non-radiative recombinations take place in addition to the increasing carrier scattering as the junction temperature increases.

When the current injection reaches 4 I_{th}, two side-lobes start to emerge at either side of the main lobe which persist even for higher injection. The fact that the emission spectrum consists of three lobes although four stacks of dashes exist is an indication that two stacks are coupled to lase collectively as had been observed in previous reports [68] for such dispersive structures with overlapping quasi-dimensionless DOS. The upper S10a and lower S10b dash groups are believed to be vertically coupled (S10) since they have the same barrier layer thickness which has been shown in previous reports [73] to have a clear effect on dash emission energy as the barrier thickness plays a significant role in affecting the vertical strain resulting in altering the dash size and thus the ground energy state emission. The appearance of these side lobes suggests that S20 and the well-coupled S10 ensembles are starting to overcome the losses of the medium and are starting to lase resulting in the shorter and longer wavelength emission lobes, respectively. When the injection current is increased further, the high (low) energy lobe is broadened while getting blue (red) shifted indicating ground state emission is taking place within the S20 (S10) ensemble in addition to the emission of tail energy states. Nonetheless, a faint emission tail is witnessed at the high energy side of the emission spectrum around 1580 nm that keeps growing as current injection is increased. However, further current injection beyond 6 I_{th} results in quenching of these components probably due to thermal carrier leakage induced by the heat buildup as the pumped current is increased due to the small band offset of the shorter dashes associated with lower wavelengths that can easily exhibit a thermally induced carrier spillover due to their shallow quantum confinement.

The progressive emission spectra at 15°C are shown in Figure 5.1(a). When compared to the room temperature emission profile, a slight blue shift is observed in the overall spectrum at all current injections. More interestingly, it is clear that a slower progressive spectrum broadening is taking place at the lower temperature value. In addition, the high energy emission tail that was visible at current injections around 6 I_{th} in room temperature never appears in the case of 15°C at any current injection. Both observations suggest that increasing the temperature and the inherent temperature rise via high current injections play a role in fully exploiting the inhomogeneous optical transitions within the active region possibly due to thermionic emission as more optical transitions become available and consequently increasing the lasing wavelength coverage. These effects become more apparent at higher temperatures as shown in Figures 5.1 (c) and (d) that show the progressive emission spectra at 30 °C and 40° C. As expected, an overall redshift in the emission throughout all current injections that is very apparent at 40 °C. In addition, onset lasing from the S20 and S10, associated with the emission side lobes, takes place at earlier current injections as the temperature increases which agrees with our previous postulation. On the other hand, while increasing temperature indeed increases the lasing wavelength coverage, a significant reduction in the quantum efficiency is observed in the form of quenching of the emission in the short wavelength region of the lasing spectra that correspond to S20 and S15 ensembles possibly to the higher probability of carrier escape from the confined active region especially in the former case as shown in high current injections in Figure 5.1(d).

5.1.2 3 µm ridge Devices

Next, we discuss the temperature dependent lasing characteristics of a different laser diode with dimensions of 3 µm × 700 µm whose progressive emission spectra are shown at Figures 5.2 (a)–(d) for temperatures of 15°C, 20°C, 30°C, and 40°C, respectively.

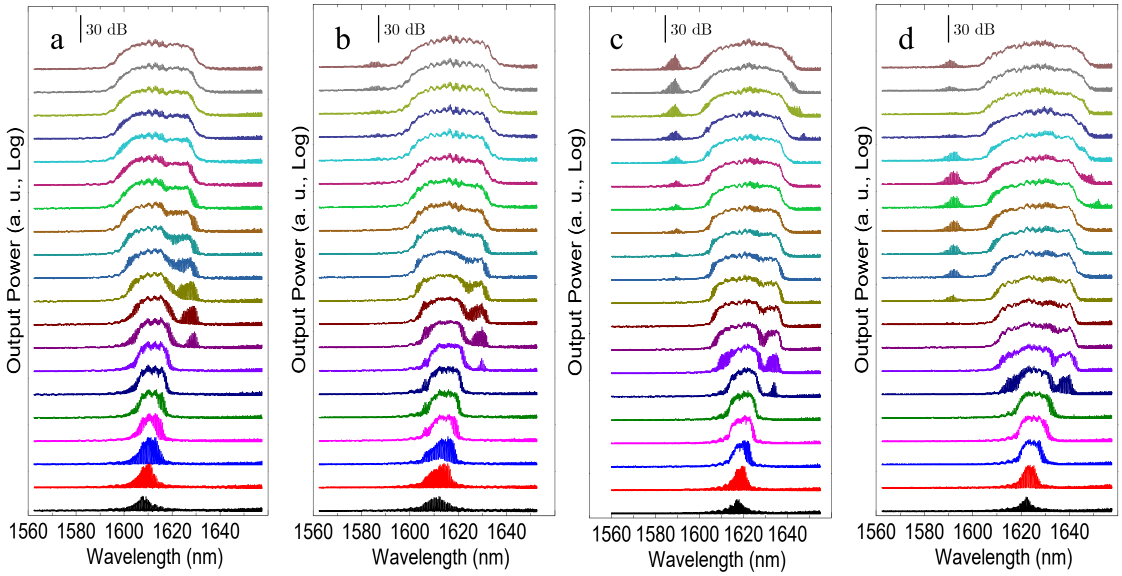

Figure 5.2: Lasing spectra of 3 µm × 700 µm chirped Qdash ridge-waveguide laser at varying current injections (1.0Ith, 1.2 - 8.2Ith in steps of 0.4Ith) at different temperatures (from left to right) (a) 15°C, (b) 20°C (room temperature), (c) 30°C, and (d) 40°.

At 15°C, as shown in Figure 5.2(a), early current injections show similar emission spectra when compared with the 2 µm wide ridge device indicating similar lasing onset from the S15 ensemble. As current injection is increased beyond 3.6 I_{th}, the emission spectra of the 2 µm wide ridge laser exhibited two side lobes. On the other hand, the 3 µm wide ridge device showed only one side lobe centered at a longer wavelength from the main lobe generated from the ground state emission of the two coupled S10 ensembles while the emission from the smaller height S20 stack of dashes is absent. In addition, in contrast with the 2 µm ridge laser, there is no appreciable overlap between the emission of high energy tails of the S10 stack and the ground state of S15 stack at intermediate current injections (below 5 I_{th}) causing a gap between both lobes which indicates no overlap between their respective DOS. These behaviors could be possibly attributed to the higher cavity losses exhibited by the wider ridge laser diodes that require a higher number of dashes to overcome the losses of the medium at intermediate current injection. However, at higher current injections, the high energy tail dashes of S10 stack are able to achieve population inversion and thus start to lase leading both lobes to merge into a single broad lobe at high current injection regime. Such merging suggests a marginal vertical potential coupling between the S10 and S15 dash ensembles probably as a result of thermally accelerated carrier tunneling between those stacks as pumping current and temperature increase evident by the stronger merging and coupling.

Much like the effect of increasing the temperature in the 2 µm device, an overall red shift is observed in all spectra as previously discussed as the temperature is increased accompanied by a slight emission broadening at the expense of the quantum efficiency in the form of power density reduction. This reduction, however, is less apparent since the higher energy emission lobe is absent for this particular ridge width as discussed previously which was shown to be drastically affected by the temperature rise. In addition, the longer wavelength side lobe emission emerges at earlier current injections as the temperature is increased. Moreover, within the high current injection regime, a portion of the ground state emission from the S20 stack starts to appear around 1590 nm. Such behavior is can be attributed to the previously discussed thermionic enhancement. However, regardless of the current injection, only ground state emission from the average height dashes within the S20 stack is observed and therefore, the whole emission spectrum fails to be fully utilized.

At 40°C, as evident by Figure 5.2(b), both long wavelength and the small portion of short wavelength components corresponding to the S10 and S20 ensembles, respectively, are able to appear at even earlier current injections. More interestingly, as pumping current is gradually increased, the short wavelength lobe portion keeps growing to a specific point and then starts getting attenuated until it fully disappears. At later current injections, however, this portion starts to reappear indicating a periodic behavior which is possible in such unstable energy-state system possibly due to thermally induced carrier spillover and redistribution. Another possible explanations are leaky substrate modes and retarded carrier diffusion. However, it is safe to neglect the former as this behavior was shown to be current and temperature dependent.

Thereafter, we shift our focus to the 4 μm ridge laser diode whose progressive emission spectral profile is shown in Figures 5.3 (a)–(d) for temperatures of 15°C, 20°C, 30°C, and 40°C, respectively.

5.1.3 4 μm ridge Devices

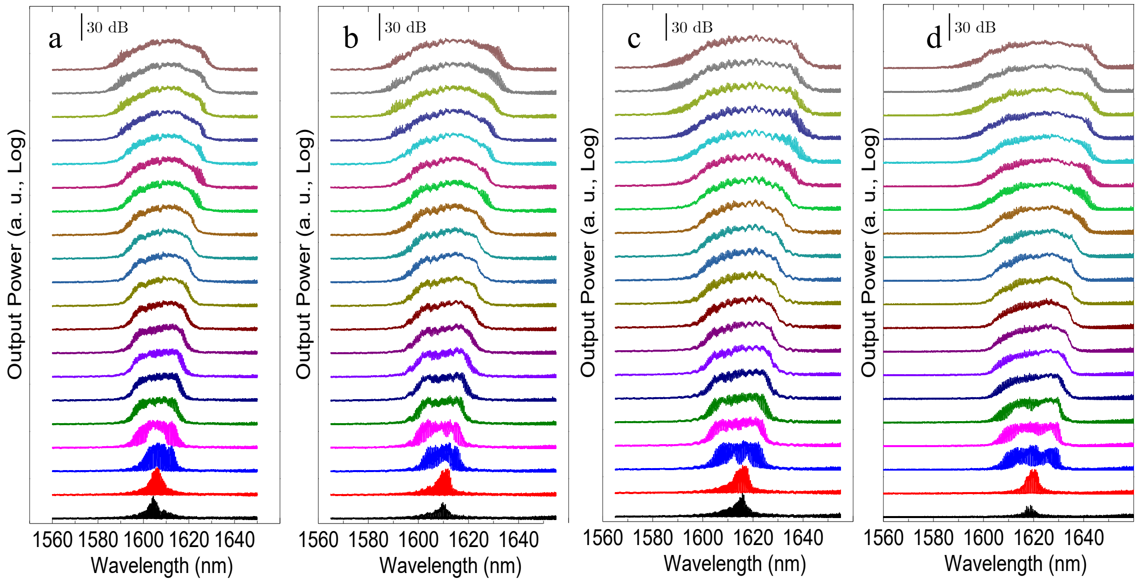

Figure 5.3: Lasing spectra of 4 μm × 700 μm chirped Qdash ridge-waveguide laser at varying current injections (1.0Ith, 1.2 - 8.2Ith in steps of 0.4Ith) at different temperatures (from left to right) (a) 15°C, (b) 20°C (room temperature), (c) 30°C, and (d) 40°.

From the first glance, a dual peak is observed at early current injections at all temperature values. However, the spectra rapidly evolve into single lobe emission spectra at much faster pace when compared with the 2 μm ridge device throughout all temperatures as more current is being injected. Consequently, we postulate that different stacks, i.e. S10, S15, and possible lower energy tail of S20, are well coupled in this case due to phono-enhanced photon-carrier coupling among these dash stacks and their appreciable overlapping DOS. By comparing all three ridge lasers, we observe that all three stack families are potentially decoupled in the case of the 2 µm ridge device enabling all of them to lase individually achieving a very broad emission by the virtue of fully exploiting the deliberate inhomogeneity nature of the device. However, as the ridge width increased, different stacks are marginally coupled in the case of the 3 µm ridge while being well coupled in the case of the 4 µm wide ridge. As a result, these stacks lase collectively limiting the potential emission broadening from such dispersive inhomogeneous structures. We attribute the coupling dependence on the larger geometrical dimensions of the ridge to the higher temperature buildup within the active region that thermally accelerate the photon-carrier tunneling between adjacent QDash ensembles.

Besides that, much like the previous cases, an overall red shift is observed as current and temperature are increased. Furthermore, a reduction in the quantum efficiency is observed as an emission instability at 30°C represented by the slight modulation effect witnessed in Figure 5.3 (c) which evolves into a flat spectral quenching at 40°C, especially at high current injections, as shown in Figure 5.3 (d).

5.2 Broad Area Device

A 15 µm × 600 µm chirped quantum dash laser has been used as a broad area laser diode. Such a structure with a geometrically larger active region, as a result of its relatively large ridge width, is expected to be associated with higher heat buildup within its active medium when compared to narrower ridge devices. Figures 5.4 (a)–(d) show the progressive emission spectra of this broad area laser at temperatures of 15°C, 20°C, 30°C, and 40°C, respectively.

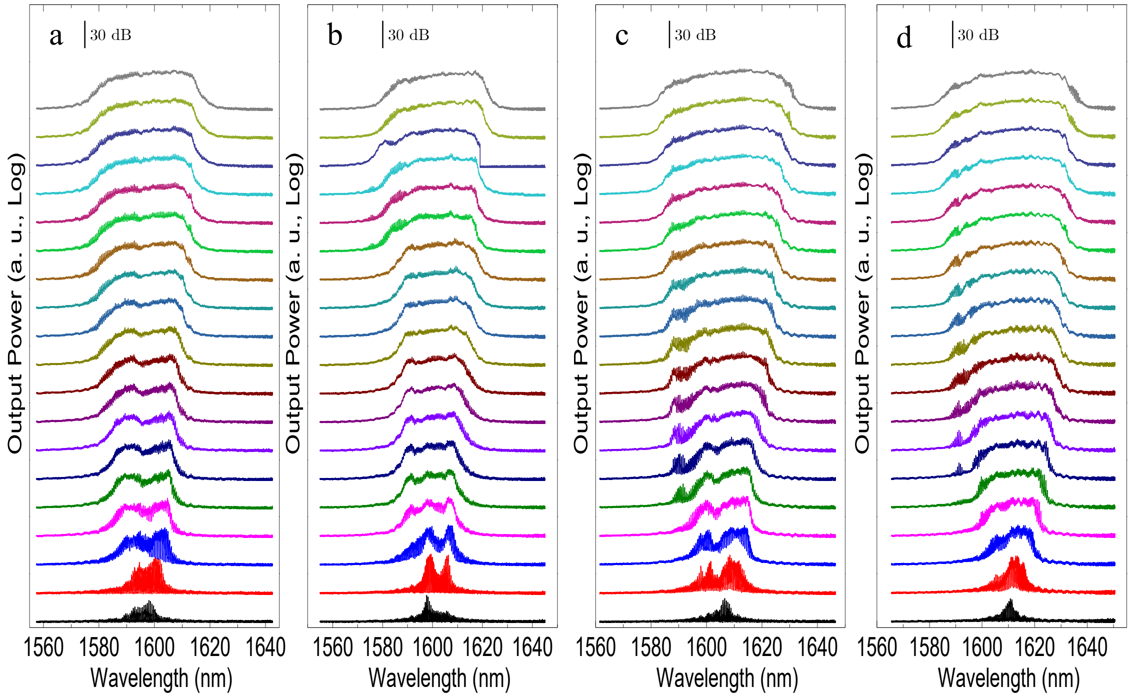

Figure 5.4: Lasing spectra of 15 µm × 600 µm chirped Qdash ridge-waveguide laser at varying current injections (1.0Ith, 1.2 - 8.2Ith in steps of 0.4Ith) at different temperatures (from left to right) (a) 15°C, (b) 20°C (room temperature), (c) 30°C, and (d) 40°.

Indeed, although onset lasing occurs at lower wavelengths, the center rapidly red shifts at a higher rate, compared to ridge devices, as current injection or temperature increase. Moreover, at intermediate current injections, an overall broader single lobe emission is observed, even at the low temperature of 15°C as shown in Figure 5.4(a), when compared to single lobe emission of the 3 µm and 4 µm ridge devices shown in Figure 5.2(a) and Figure 5.3(a), respectively. Yet again, such broadening occurs at the expense of reducing the quantum efficiency. However, this reduction is balanced out by the excess number of available carriers as a direct result of the broader active medium area leading to more electron-hole pair recombinations and ultimately resulting in a higher number of generated photons. In addition, at intermediate current injections at temperatures of 30°C and 40°C as shown in Figures 5.4 (c) and (d) respectively, a third small side lobe starts to emerge at shorter wavelengths from the main lobe. As more current is being injected, this side lobe merges with the main lobe resulting in a somewhat broader emission. All these behaviors further confirm and agree with our previous attribution to the thermionic emission that takes place at high temperatures.

CHAPTER 6

IMPLEMENTATION OF THE CHIPRED QUANTUM DASH LASER IN OPTICAL COMMUNICATION SYSTEMS

By employing the knowledge acquired in the previous chapters on the lasing characteristics of the chirped QDash lasers, we were able to optimize different operation parameters for their implementation in an optical communication system. In this chapter, we show the employment of QDash laser's entire lasing emission spectral range as a carrier in ON-OFF-KEYING (OOK) modulation. Thereafter, we explore the viability of using a single FP mode instead of the entire spectrum via a tunable optical filter (TOF) and through injection locking. We ultimately then explore the limits of applying this laser in optical communications in terms of maximum transmission data rate and longest fiber length possible.

6.1 Adopted Operation Parameters

The chosen QDash laser was one of an intermediate cavity length of 1100 µm that sustained CW probing while maintaining a good balance between high output optical power and lasing emission center of relatively short wavelength in order to meet the wavelength specifications of the different C and L band communication system elements. Moreover, among the few laser devices that can sustain CW pumping for long periods of time, this particular device showed a great deal of stability and consistency between the measured transient peak power and the steady-state integrated average power. The ridge width was selected to be the widest, *i.e.* W=4 µm, yielding in broadest area of active medium (among ridge lasers) in order to get the maximum output optical power. Although, narrower ridge values achieve broader emission as discussed in the previous chapter, in OOK, however, emission bandwidth does not play any role in the success or quality of optical signal modulation.

The operation temperature was set at low 15^{o}C in order to blue shift the emission spectrum as much as possible. Temperatures below 15^{o}C have been avoided in order to reduce the probability of frost formation over the brass base that could lead to severely damaging the laser diode. Furthermore, CW mode has been adopted in order to ensure valid continuous optical signal modulation while emitting at high enough power to be transmitted and detected at the receiver side.

Finally, the value of the injected DC current was 340 mA (~2.25 I_{th}) that results in a maximum peak power of ~2.34 mW as evident by the L-I characteristic curve of this device at 15°C shown in the inset of Figure 6.1. The lasing spectrum at this DC current injection is shown in Figure 6.1 where the emission is centered at ~1632 nm with a -3dB bandwidth of ~ 6 nm and a wavelength coverage of ~ 35 nm.

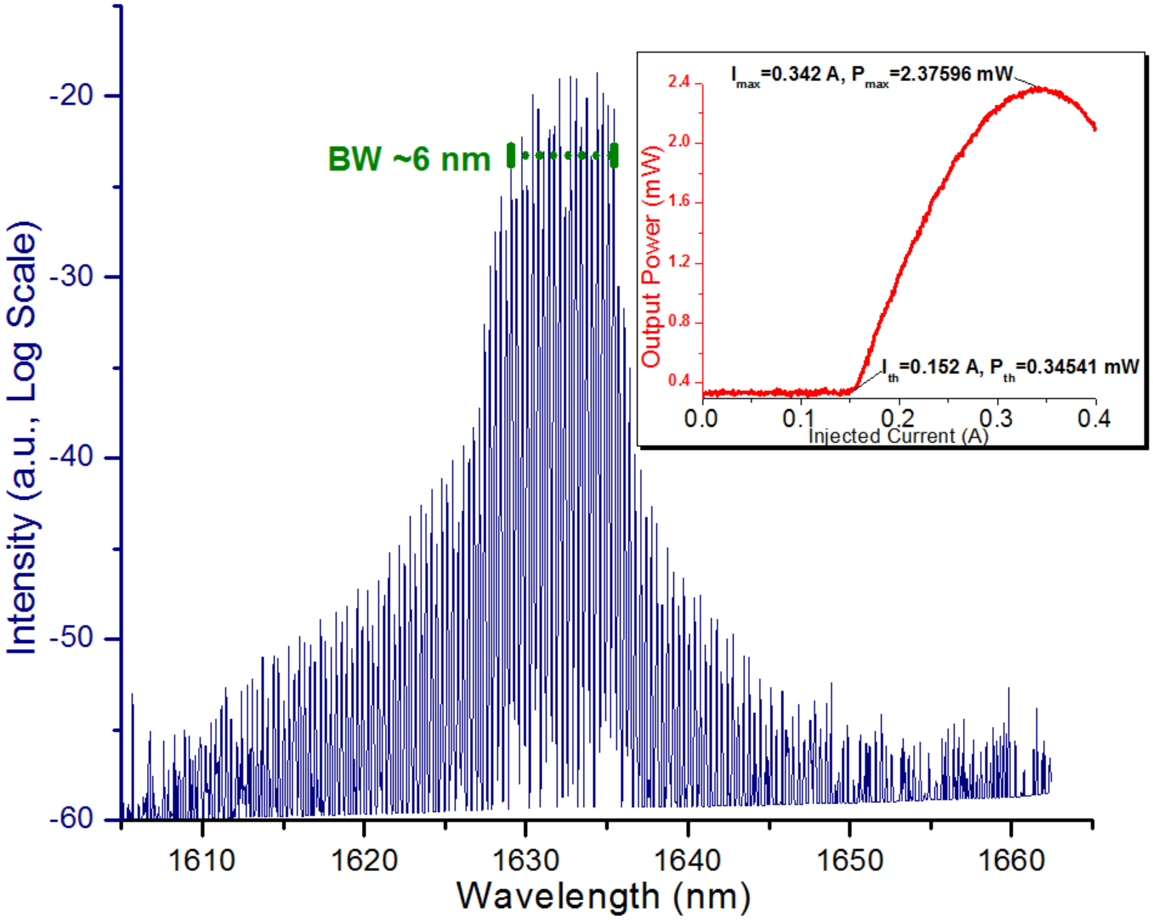

Figure 6.1: CW emission spectrum of the 4 µm × 1100 µm QDash laser at a current injection of 0.34 A at 15°C. The inset shows the associated L-I characterisitc curve at the same temperature.

6.2 OOK Modulation of the Entire Emission Spectrum

After setting up all the operation parameters, we coupled the CW stimulated emission optical power from one of the laser facet, into a lensed single mode fiber. The entire emission spectrum of the laser has been used as a sub-carrier to modulate and transmit the OOK signal in a back-to-back (BTB) configuration which serves as a reference case and later via by an optical fiber link.

6.2.1 Optical Communication System Setup

The emission from the laser diode has been coupled to a tapered-lensed faceted single mode fiber. The tapered facet design was adopted in order to avoid the formation of an external cavity between the laser facet and the fiber facet that can reduce the spectral modulation effects in the emission spectrum. Thereafter, we used a variable optical attenuator (VOA), shown in Figure 6.2, in order to adjust the optical output power and investigate its variation over the communication system.

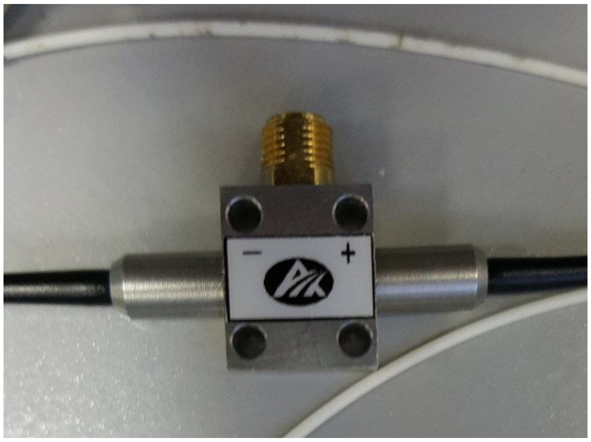

Figure 6.2: Variable optical attenuator used to attenuate the optical output power of QDash laser.

The message signal in this system is an electrical radio frequency (RF) 2^{15}-1 long pseudo-random bit sequence (PRBS) that has been generated using a super high frequency (SHF) bit pattern generator that is shown in Figure 6.3.

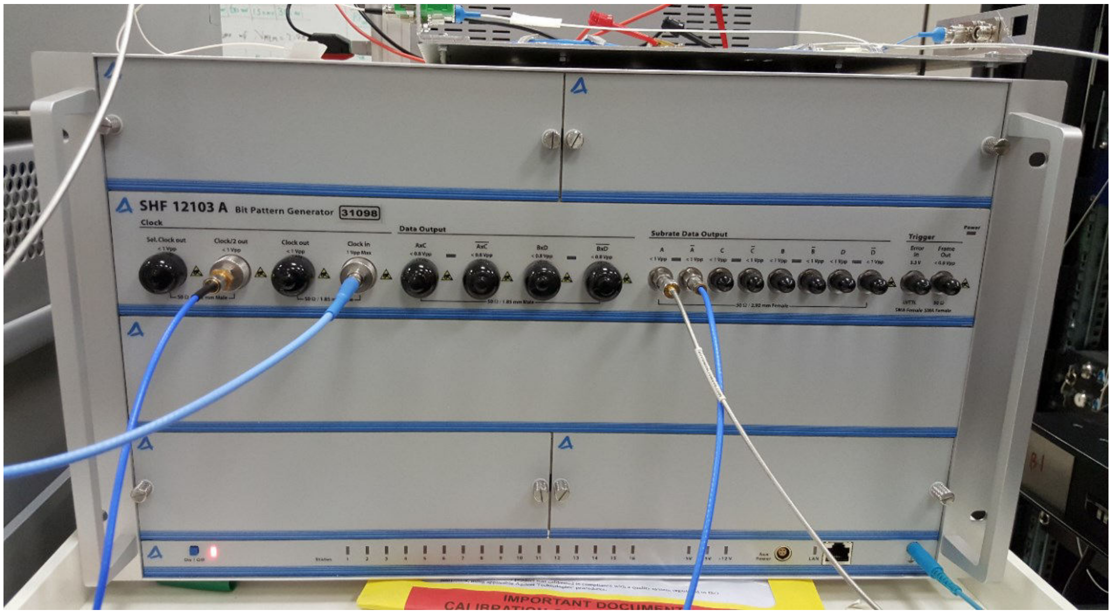

Figure 6.3: SHF 12103A bit pattern generator that is used to generate the message signal.

This bit pattern generator has been clocked at different frequencies in order to achieve different data rates via the vector signal generator shown in Figure 6.4 that can generate frequencies up to 44 GHz.

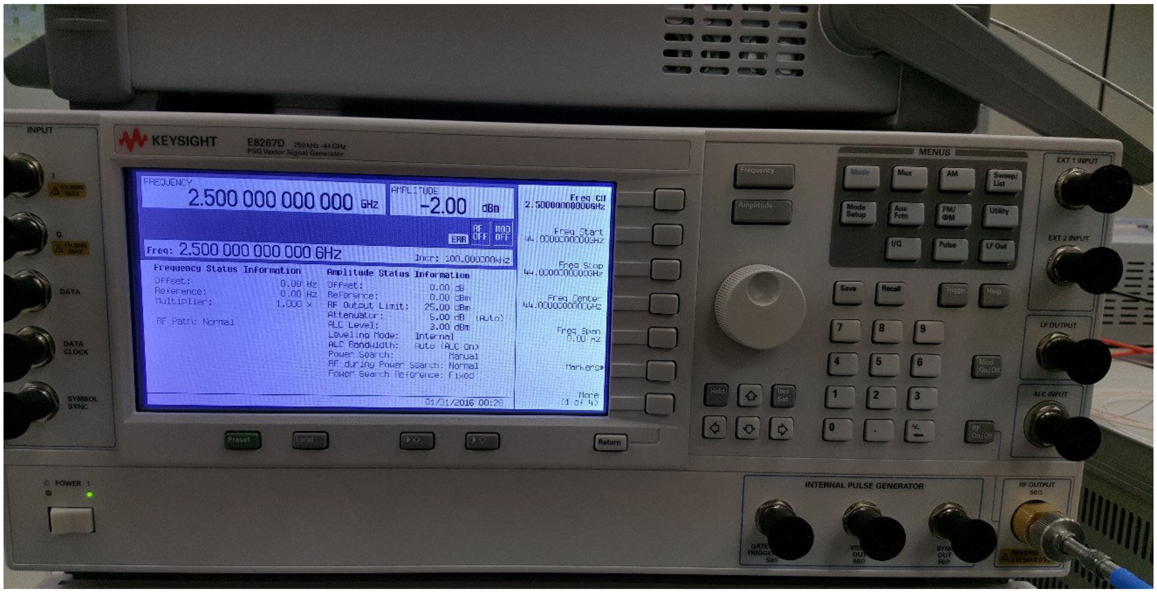

Figure 6.4: KEYSIGHT E8267D Vector signal generator that is used to clock the SFH bit pattern generator.

Thereafter, the RF message signal (bit stream) is pre-amplified via a SHF electrical amplifier and then passed through a Lithium Niobate ($LiNbO_3$) Mach-Zehnder modulator (MZM), in order to modulate (intensity modulation) the optical CW emission of the QDash laser which is passed through the input port of the modulator circuit, shown in Figure 6.5 where the MZM and the SHF amplifier are highlighted in green and yellow, respectively.

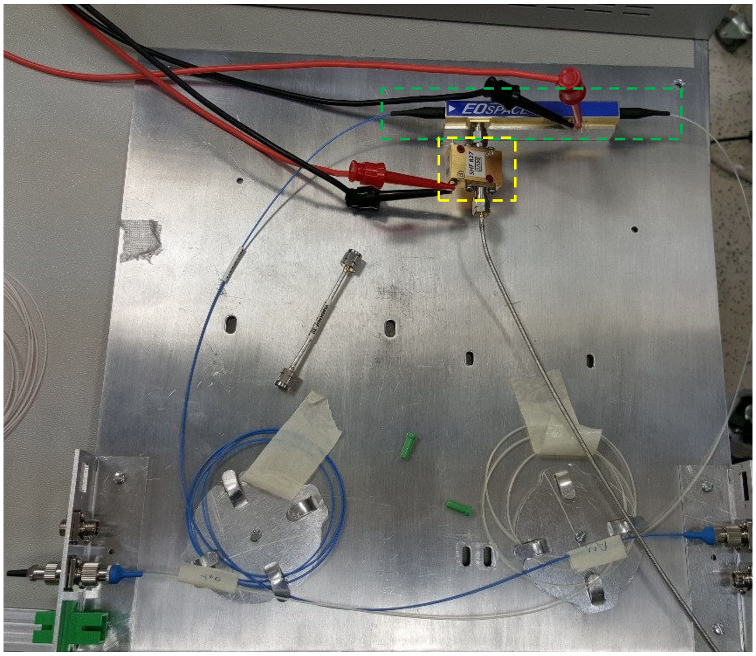

Figure 6.5: The optical modulation circuit. The EOSPACE MZM and the SHF 32950 RF amplifier are highlighted in green and yellow, respectively.

The output of the modulator circuit is an optical intensity modulated signal that is ready to be transmitted. All of the aforementioned elements constitute the transmitter side of the optical communication system.

After transmission, at the receiver side, the optical modulated signal is detected though a lightwave multimeter acting as a reference receiver, thus converting the optical signal to an equivalent electrical (RF) signal. Without any attenuation enforced by the VOA, the detected power at the receiver was measured to be approximately -6.5 dBm after modulation and transmission whereas the unmodulated CW emission of the QDash laser was about $+1.85$ dBm as measured by the lightwave multimeter, as shown in Figure 6.6, which can be used as an optical power meter as well. This indicates that the power losses associated with insertion and modulation losses accumulate to a power reduction of ~ 8.35 dB.

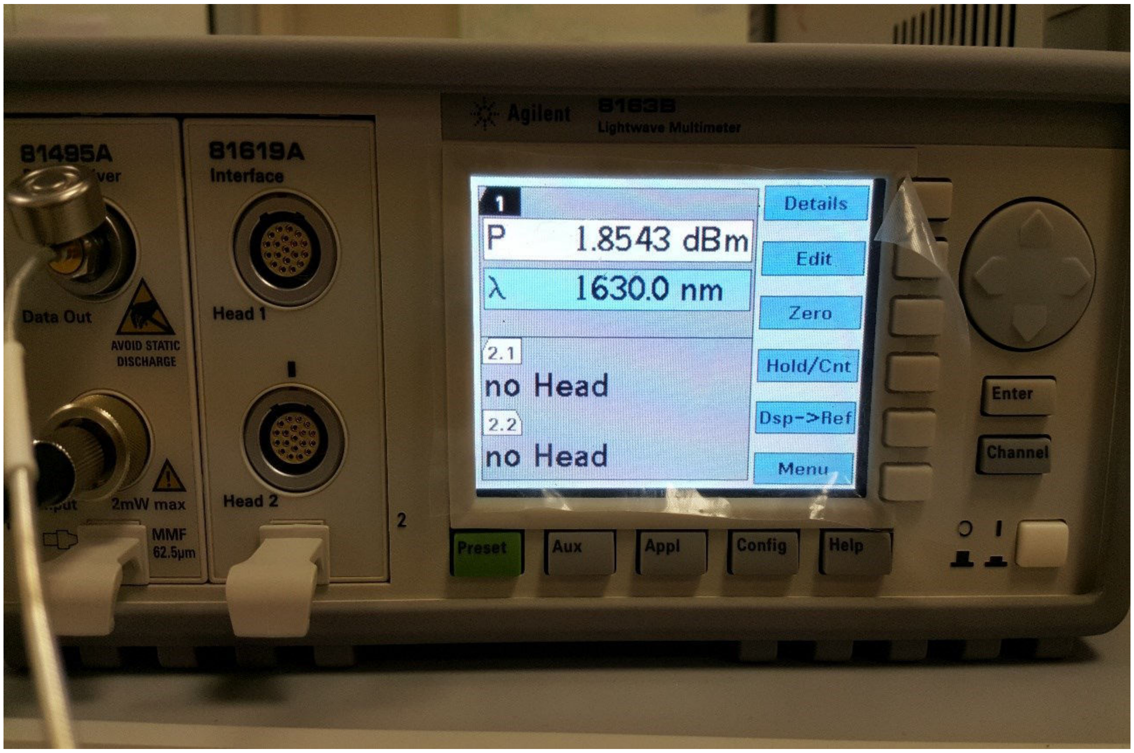

Figure 6.6: The AGILENT 8163B Lightwave multimeter used at the receiver side of the communication system to detect and convert the modulate signal into an RF signal.

Finally, the recovered RF signal is inputted into a digital communication analyzer (DCA), shown in Figure 6.7, in order to evaluate and analyze the recovered signal. Nevertheless, in order to ensure accurate detection, a copy of the clock signal generated by the vector signal generator is passed into the DCA in order to synchronize the recovered signal with the original message signal.

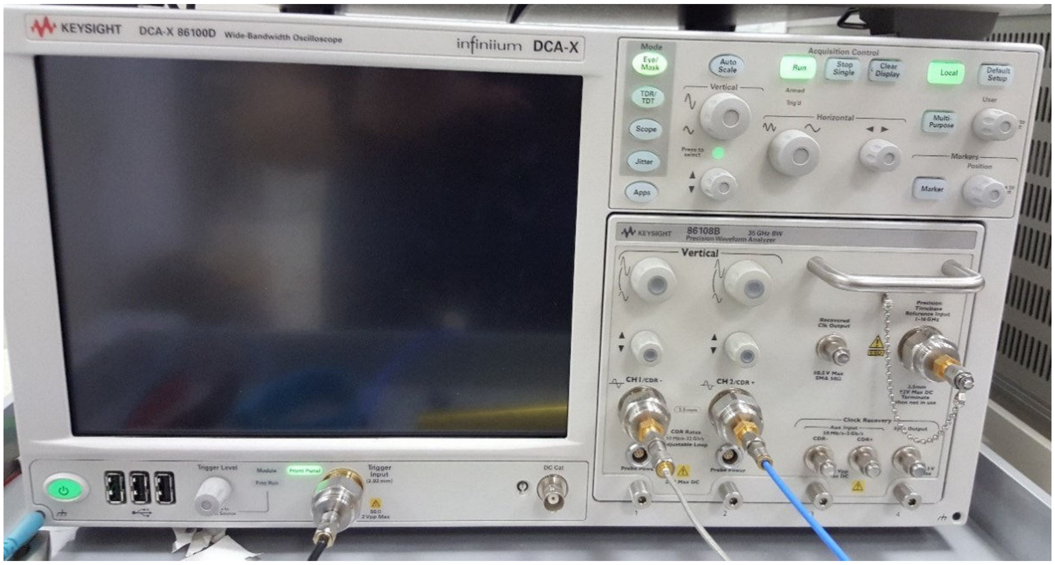

Figure 6.7: The KEYSIGHT 86100D DCA that is used to evaluate and analyze the recovered signal.

Figure 6.8(a) shows an illustration of the whole communication system in which the QDash laser has been employed. Figure 6.8(b) shows the block diagram of this system.

6.2.2 OOK Modulation in BTB Configuration

The DCA generates the eye diagrams of the recovered signals. The eye diagram is a powerful diagnosis tool that can infer different parametric information that reflect the healthiness of digital signals. After using the aforementioned setup, we carried out a parametric study by sweeping through different optical output powers from the QDash laser via the VOA while varying the clock frequency and, in turn, the data rate.

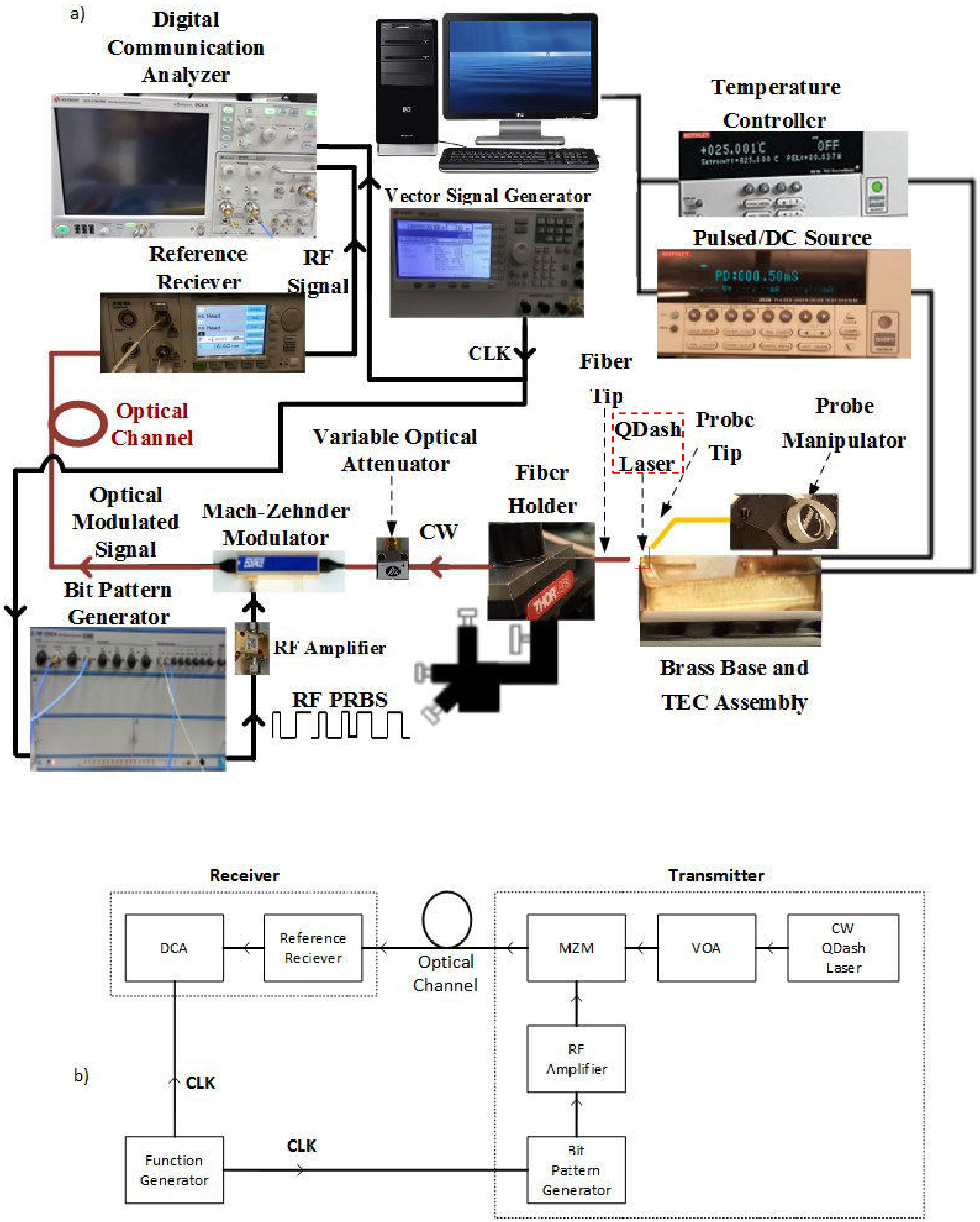

Figure 6.8: (a) An illustration showing the different elements of the OOK optical communication system where red and black represent optical and RF connections, respectively. (b) Block diagram of the communication system.

Figure 6.9 shows the bit pattern diagram of the message signal modulated at 5 Gb/s and the recovered signal represented by the green and yellow diagrams, respectively, where the pattern diagram of the recovered signal in Figure 6.9 is a delayed version of the transmitted signal and hence they do not match in the Figure.

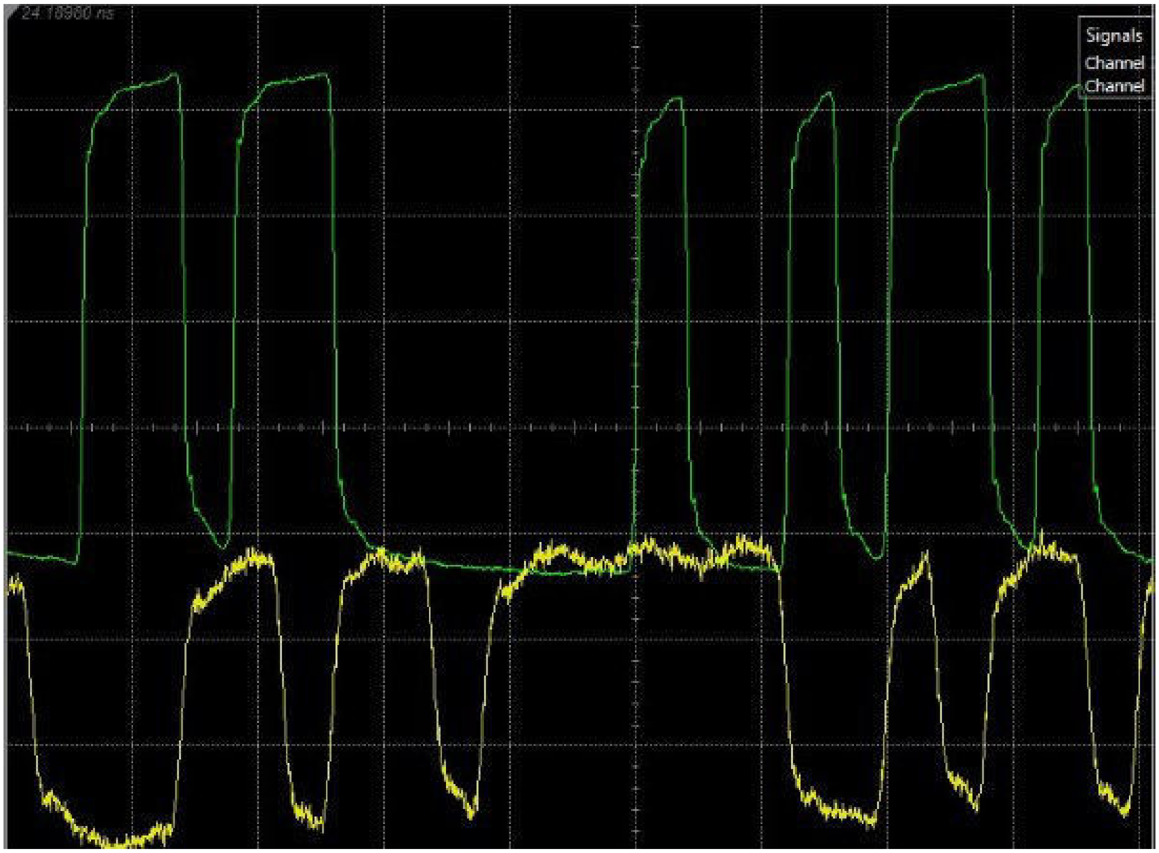

Figure 6.9: The bit pattern diagram of the original message signal (top) and the recovered signal (bottom).

Figure 6.10 shows the measured eye diagrams of the recovered signals at different received powers, namely -6.5, -8, -11, -14, -17, and -20 dBm (from top to bottom), while the signal was modulated and transmitted at 5 Gbps.

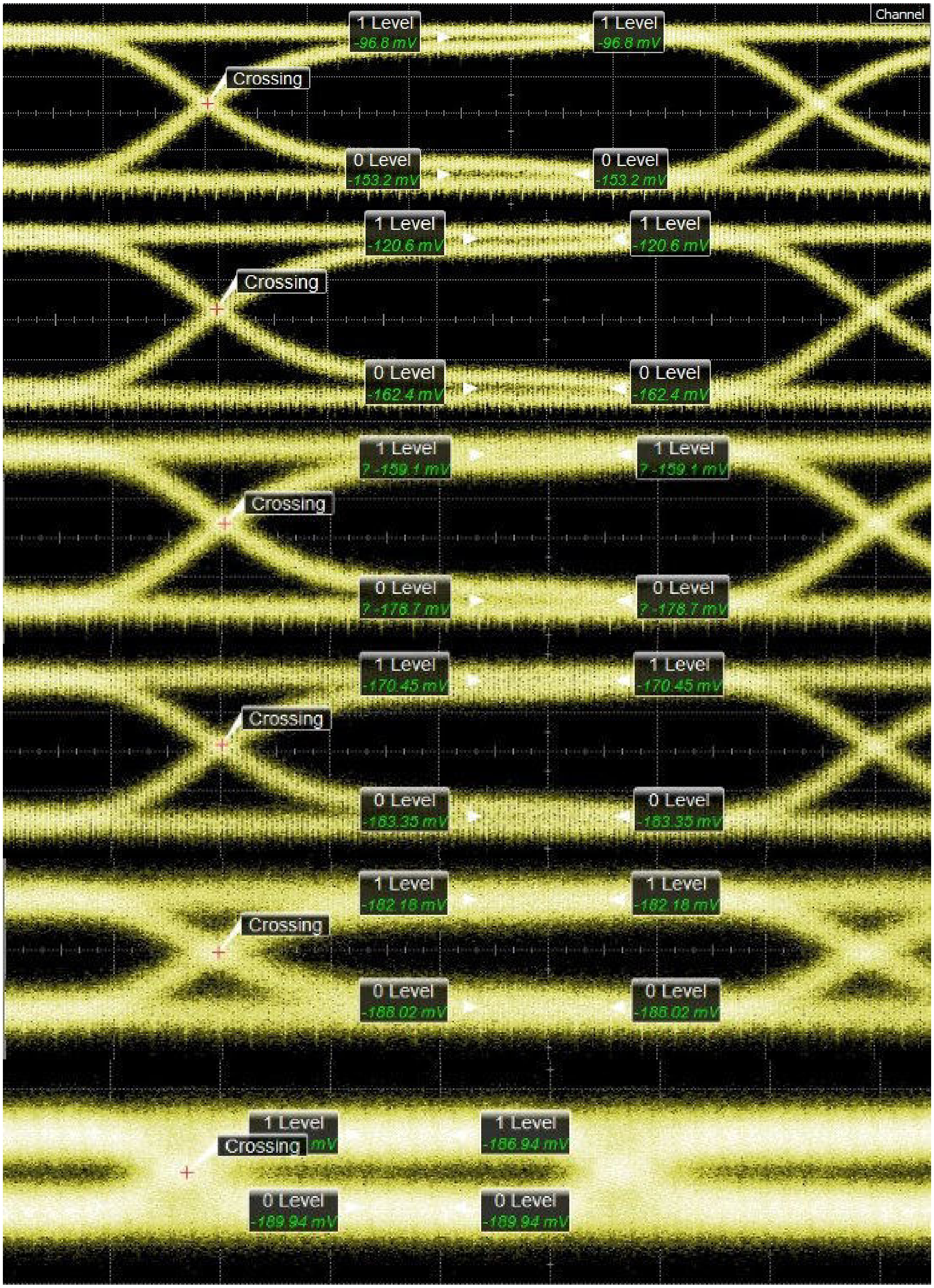

Figure 6.10: The eye diagrams of the recovered signals at different received powers, namely -6.5, -8, -11, -14, -17, and -20 dBm (from top to bottom) at 5 Gbps.

The openness of an eye diagram, both vertically and horizontally, is a direct indication of the quality of the recovered signal. The horizontal openness of an eye diagram (eye width) reflects how well aligned both the rise and fall times of each bit are, which constitutes the jitter time and the duty cycle distortion (DCD). These parameters represent the deviation of the rise and fall times of the bits with respect to their average and are desired to be as low as possible. As the transmission rate is increased, reflections, chromatic dispersion, signal distortion, and inter-symbol interference (ISI) play a major role in increasing the jitter time and the DCD of the eye diagram and in turn reducing its width. The DCD is given by [74]:

$$DCD = 100 \times \frac{Width\ between\ rising\ and\ falling\ edges\ @\ 50\%\ level}{Eye\ Width} \tag{6.1}$$

On the other hand, the vertical eye openness (eye height) of the eye, plays a significant role in received bit decision making between 0 and 1. The standard deviation of the Gaussian probability density function (PDF) of the 0's and 1's occurrences are used to define eye height as [74]

$$Eye\ Height = 1\ level + 3\sigma_1 - 0\ level - 3\sigma_0 \tag{6.2}$$

where

- σ_0 is the standard deviation of the PDF of 0's occurrences.
- σ_1 is the standard deviation of the PDF of 1's occurrences.

From the eye height, we can find the Q-factor according to [75]

$$Q = \frac{Eye\ Height}{\sigma_0 + \sigma_1} \tag{6.3}$$

In addition, the crossing point between 0 bits and 1 bits is required to be as close as possible to 50% of the overall amplitude in order to ensure accurate distinction and decision making between 0's and 1's. The eye crossing percentage can be calculated through [74].

$$Crossing_{\%} = 100 \times \frac{Crossing\ level - Zero\ level}{Eye\ Height} \tag{6.4}$$

Table 6.1 summarizes the extracted eye diagram parameters at the different received power values at a transmission rate of 5 Gb/s.

We notice that as optical power is approaching the sensitivity limit of the reference receiver in the case of -17 dBm and -20 dBm, the DCA becomes unable to measure the DCD.

Table 6.1: The extracted eye diagram parameters at the different received power values (-6.5, -8, -11, -14, -17, and -20 dBm) at a transmission rate of 5 Gb/s.

Detected Power (dBm)	Eye Width (ps)	DCD (ps)	Jitter (ps)	Eye Amp. (mV)	Eye Height (mV)	Q factor	Crossing (%)
-6.5	184.4	1.80	2.665	56.44	34.18	7.63	52.4
-8.0	184.0	1.80	2.665	41.74	25.34	7.60	52.1
-11	178.90	2.65	3.510	19.61	10.74	6.63	53.3
-14	177.45	2.65	3.755	12.91	7.00	6.56	52.1
-17	155.8	--	7.360	5.824	1.874	4.42	51.0
-20	15.20	--	30.805	3.012	0.602	2.66	48.1

Next, we repeated the measurement at a data rate of 10 Gb/s while attenuating the CW emission of the QDash laser to different optical powers of -6.5, -8, -11, -14, -17, and -20 dBm. Figure 6.11 shows the eye diagrams of the recovered signals at 10 Gb/s at received power of -6.5, -8, -11, -14, -17, and -20 dBm (from top to bottom) while the extracted eye diagram parameters are tabulated in Table 6.2.

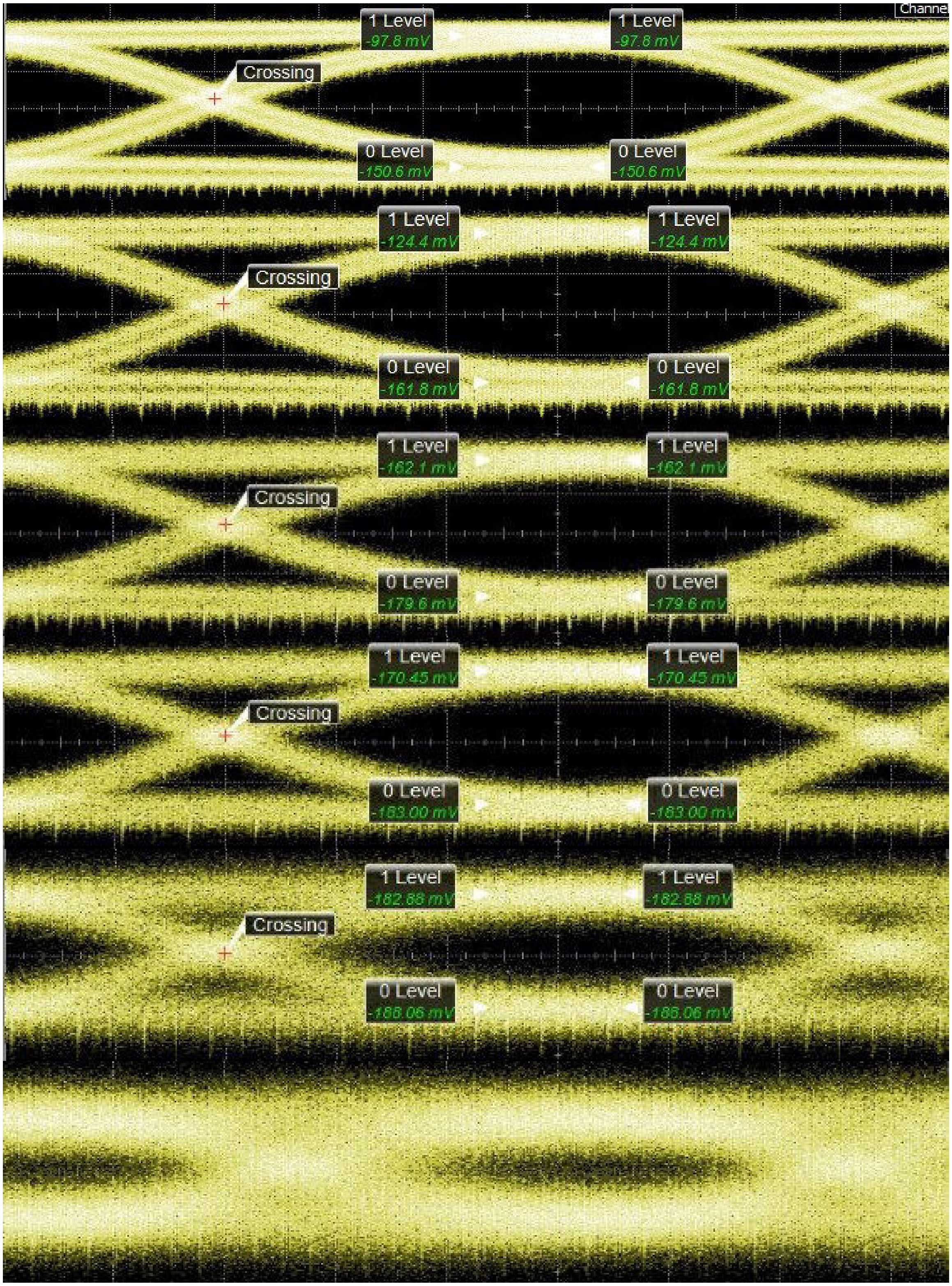

Figure 6.11: The eye diagrams of the recovered signals at different received powers, namely -6.5, -8, -11, -14, -17, and -20 dBm (from top to bottom) at 10 Gb/s.

According to the closeness of the last eye diagram in Figure 6.11, a received power of -20 dBm renders the demodulation of the signal impossible while the eye in case of -17dBm is barely open.

Table 6.2: The extracted eye diagram parameters at the different received power values (-6.5, -8, -11, -14, -17, and -20 dBm) at a transmission rate of 10 Gb/s.

Detected Power (dBm)	Eye Width (ps)	DCD (ps)	Jitter (ps)	Eye Amp. (mV)	Eye Height (mV)	Q factor	Crossing (%)
-6.5	76.92	2.66	2.850	52.80	30.78	7.19	52.3
-8.0	76.04	3.66	2.996	37.28	21.48	7.08	52.5
-11	73.90	4.10	4.543	15.47	8.35	6.45	52.2
-14	71.48	5.00	4.756	12.56	6.58	6.31	52.5
-17	49.44	--	8.432	5.184	1.496	4.22	47.8
-20	--	--	--	--	--	--	--

Finally, Figure 6.12 shows the eye diagrams of the recovered signals at 20 Gb/s at received power of -6.5, -8, -11, -14, -17, and -20 dBm (from top to bottom) while the extracted eye diagram parameters are tabulated in Table 6.3.

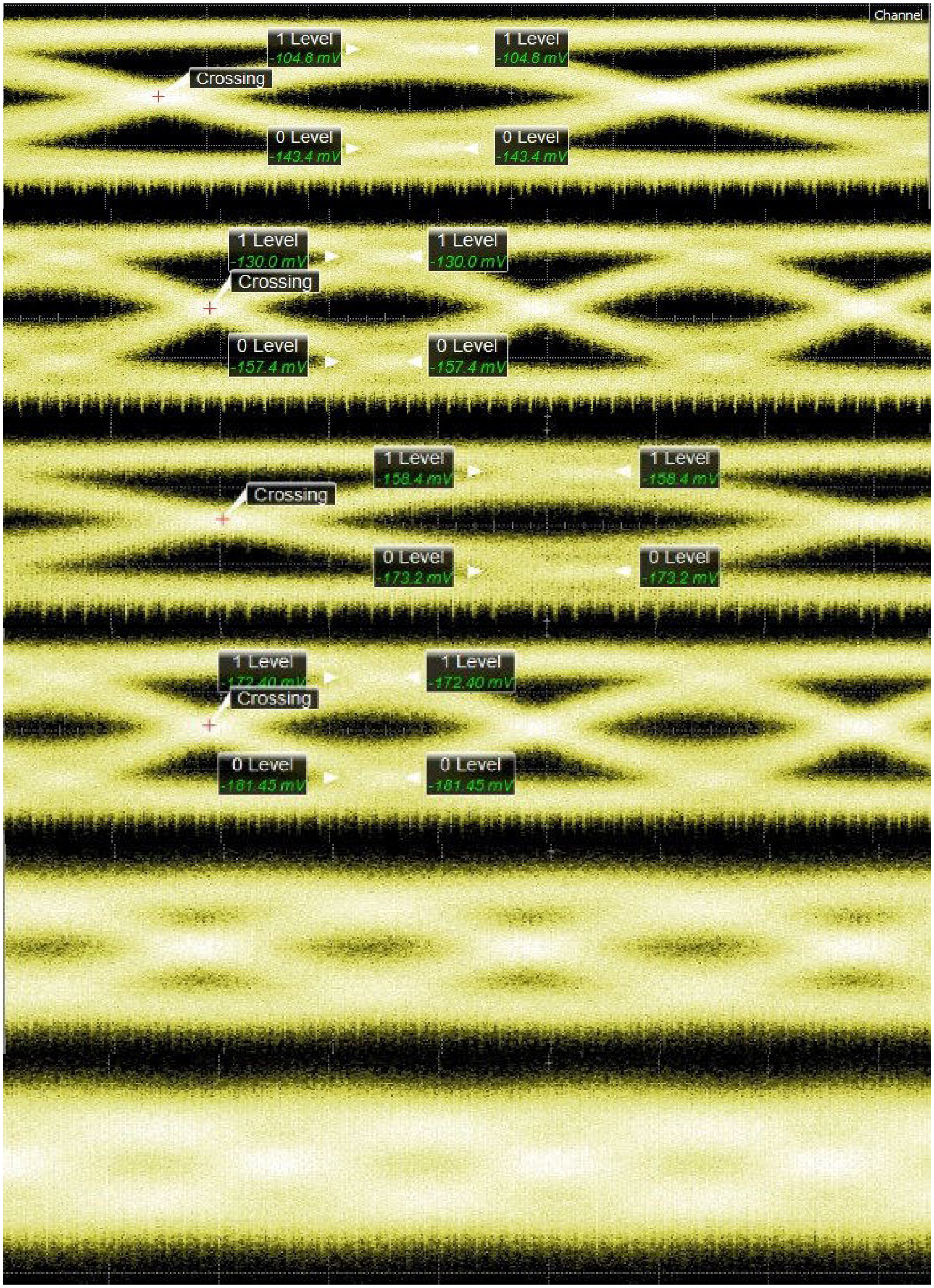

Figure 6.12: The eye diagrams of the recovered signals at different received powers, namely -6.5, -8, -11, -14, -17, and -20 dBm (from top to bottom) at 20 Gb/s.

Figure 6.12 indicates that successful transmission and demodulation are achieved at data rate only given that the received power is at least -14 dBm as evident by the eye closeness in subsequent data rate.

Table 6.3: The extracted eye diagram parameters at the different received power values (-6.5, -8, -11, -14, -17, and -20 dBm) at a transmission rate of 20 Gb/s.

Detected Power (dBm)	Eye Width (ps)	DCD (ps)	Jitter (ps)	Eye Amp. (mV)	Eye Height (mV)	Q factor	Crossing (%)
-6.5	27.01	4.80	3.831	38.60	5.938	2.96	52.1
-8.0	26.28	4.12	3.954	27.26	5.45	2.94	51.8
-11	24.42	5.45	5.260	14.86	2.972	2.90	51.7
-14	19.80	4.12	5.036	9.02	1.80	2.80	52.1
-17	--	--	--	--	--	--	--
-20	--	--	--	--	--	--	--

With all said and done, in BTB configuration, we conclude that without any artificial attenuation (received power of -6.5 dBm), the maximum transmission data rate is 20 Gb/s which is evident by the closed eye diagram shown in Figure 6.13 when the data rate is raised to 21 Gb/s.

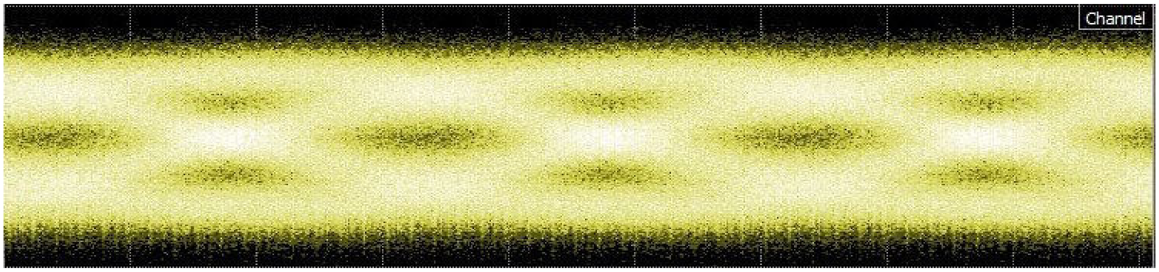

Figure 6.13: The closed eye diagram when the data rate is set at 21 Gb/s with no artificial power attenuation.

The limitation of the successful transmission are imposed by different factors. These factors either empede the the vertical opennes or the horizontal opnnenss of the eye diagram and their respective parameters. Vertical opnness of the eye diagram is afftected by the optical output power of the QDash laser in addition to different lossess that occur at different elements of the communication system. Horizontal openness, on the other hand, is affected mainly at high rates by pulse spreading due to chromatic dispersion and reflections. In order to visualize how these parameters are affected , Figure 6.14 shows the variation of the horizontal openness parameters, *i.e.* eye width, DCD, and jitter time, as functions of the received power in green, red, and blue, respectively, while Figure 4.15 shows the variation of the vertical openness parameters, *i.e.* eye amplitude, eye height, and Q-factor, as functions of the received power in green, red, and blue, respectively, for each of transmission rates of 5, 10, and 20 Gb/s.

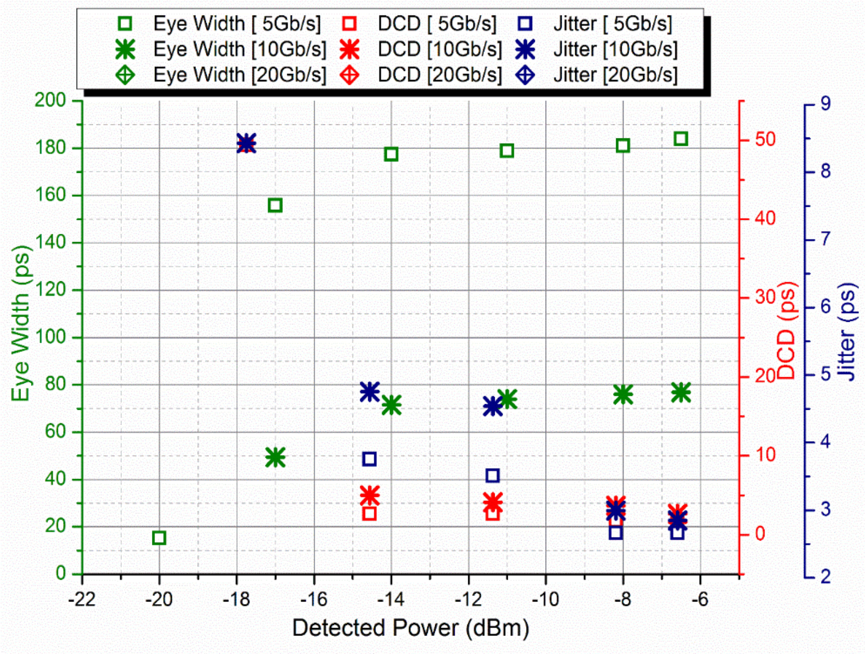

Figure 6.14: The variation of the eye width, DCD, and jitter time as functions of the received power in green, red, and blue, respectively, for each of transmission rates of 5, 10, and 20 Gb/s.

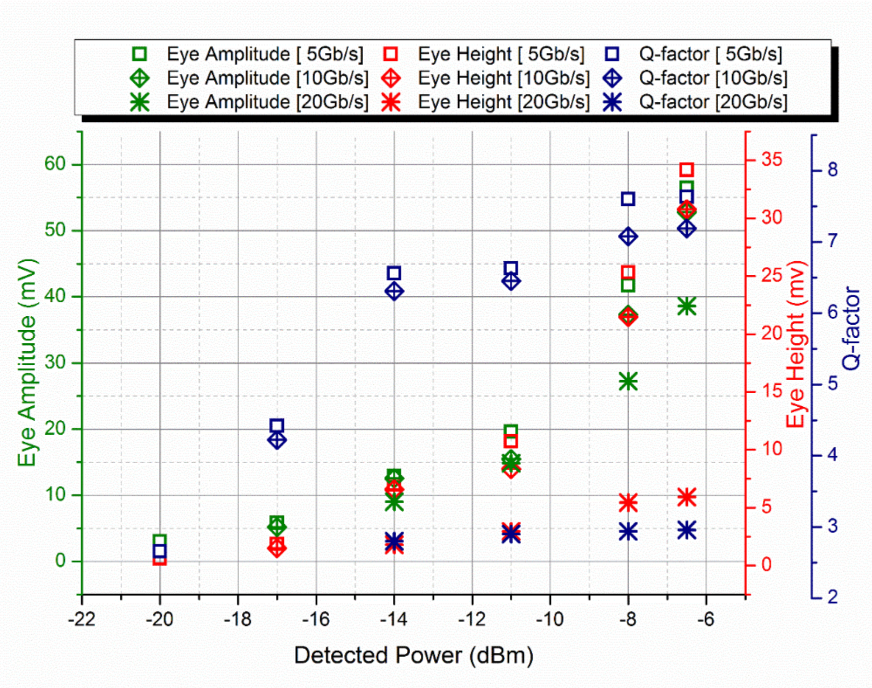

Figure 6.15: The variation of the vertical openness parameters, i.e. eye amplitude, eye height, and Q-factor, as functions of the received power in green, red, and blue, respectively, for each of transmission rates of 5, 10, and 20 Gb/s.

From these figures, we observe that as the optical power is attenuated, all vertical openness parameters witness a decrease in their values as the received power approaches the sensitivity rating of the photo-detector. The decrease of both eye height and eye amplitude is relatively gradual while this decrease is more abrupt in the case of Q-factor since, by definition, it depends entirely on the power value of the signal. Moreover, by comparing the rates at which both the vertical and horizontal openness of the eye diagrams, we can conclude that output optical power of the laser is the most limiting factor in this communication system.

In order to evaluate the performance of the communication system, the bit error rate (BER) is estimated. BER is measure that quantifies the probability of erroneous in decoding a digital signal. Given that the noise inside the communication channel is Additive White Gaussian Noise (AWGN), BER in OOK modulation can be estimated as a function of the Q-factor via [75]

$$BER_{OOK} = \frac{1}{2}\operatorname{erfc}\left(\frac{Q}{\sqrt{2}}\right) \tag{6.5}$$

where

- erfc is the complementary error function which is given by

$$\operatorname{erfc}(x) = \frac{2}{\sqrt{\pi}}\int_{x}^{\infty} \exp(-t^2)\, dt \tag{6.6}$$

Several studies have shown that the AWGN model for the noise is valid to a great degree over short-long haul and metropolitan fiber link communications systems that follows direct non-return-to-zero (NRZ) direct detection where no Erbium-Doped Fiber Amplifiers (EDFA) are used [76-79]. This claim is further supported by compliance of estimated BER according to (6.2) with the measured values demonstrated in [79, 80]. Figure 6.16 shows the estimated BER as a function of the received power at data rates of 5, 10, and 20 Gb/s while the dashed green line represents the error-free transmission level (BER$\leq 10^{-9}$).

From the figure, we observe that the BER is consistent in the case of 20 Gb/s with BER ~ 10^{-3} regardless of the received power. On the other hand, in the case of lower transmission rates the same BER is observed when the received power is lowest (-20 dBm). However, as the received power is increase, the BER is improved dramatically till it reached 10^{-12} and 10^{-14} at a received power of -8 dBm in the cases of 5 and 10 Gb/s, respectively. Moreover, error-free transmission can be achieved for these rates at received powers greater than ~ -15 dBm.

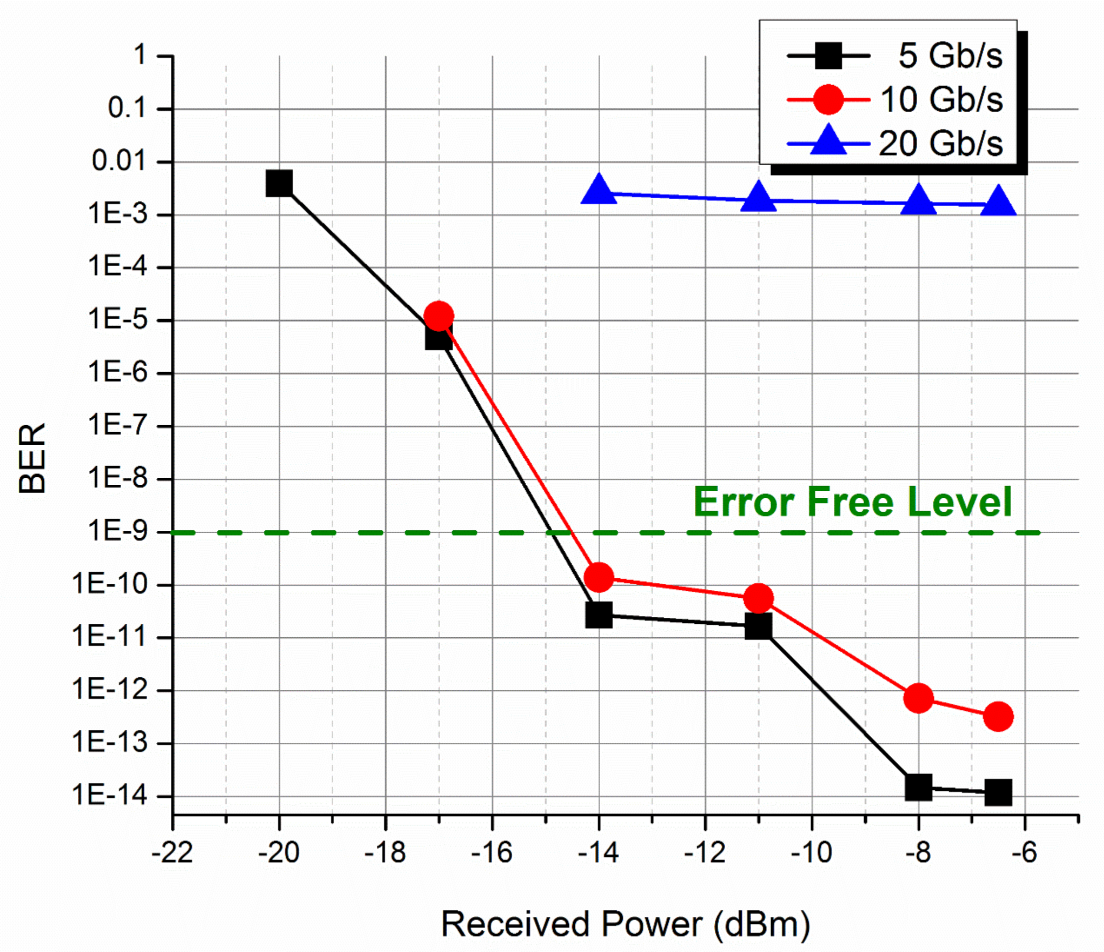

Figure 6.16: BER vs. the received power for different data rates.

6.2.3 OOK Modulation over Optical Fiber Link

Figure 6.17 shows the bit pattern diagram (top) and the eye diagram (bottom) when the BTB configuration is replaced by a single mode optical fiber link of 10 km length at a transmission rate of 5 Gb/s. The extracted eye diagram parameters in the case of transmission are tabulated in Table 6.4.

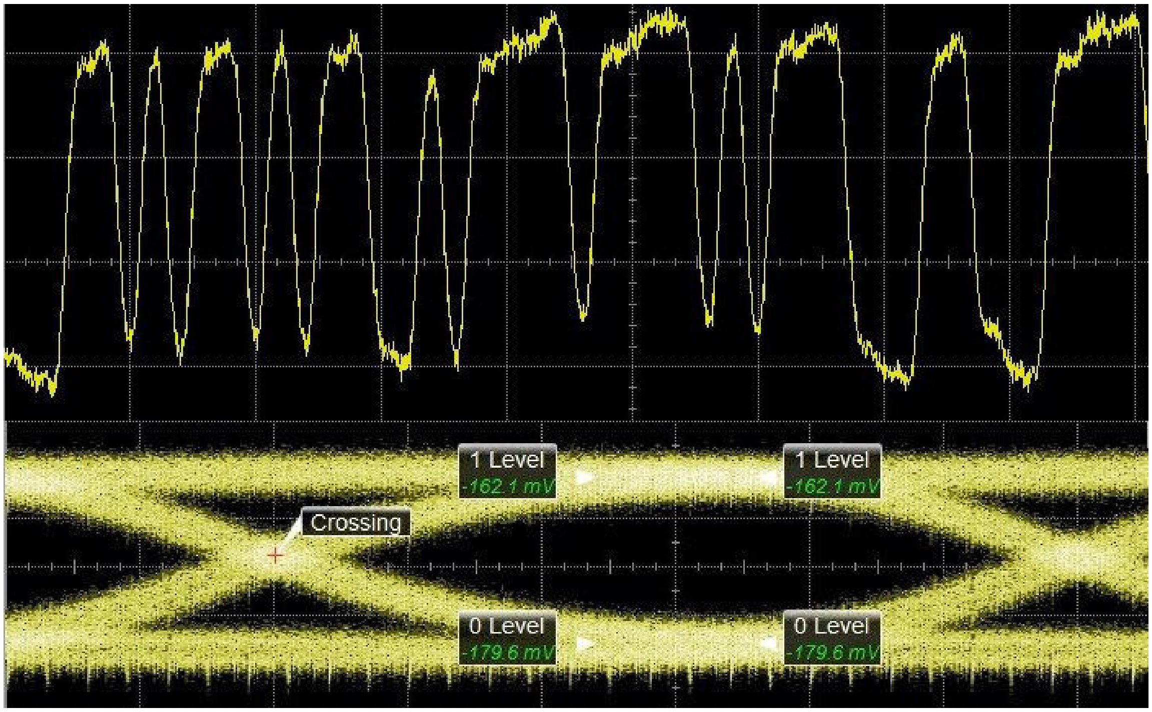

Figure 6.17: Bit pattern diagram (top) and eye diagram (bottom) in the case of transmission over a 10 km long single mode optical fiber link.

Table 6.4: Extracted eye diagram parameters in the case of transmission over a 10 km long single mode optical fiber link.

Detected Power (dBm)	Eye Width (ps)	DCD (ps)	Jitter (ps)	Eye Amp. (mV)	Eye Height (mV)	Q factor	Crossing (%)
-10.5	173.90	4.00	4.354	17.54	9.53	6.57	52.2

It has been observed that transmission over this fiber introduced an attenuation of ~0.4dB/km as the emission wavelength is 80 nm red shift from the rated 1550 nm of the single mode fiber. Moreover, both the eye height and eye amplitude have witnessed a reduction of 24 mV and 38 mV, respectively. Given our power budget, the maximum fiber link length that is estimated to attenuate the maximum received power (-6.5 dBm) to the minimum power (-20 dBm) is ~35 km after which the eye diagram is fully closed. Moreover, when comparing the 10 km fiber case with the reference BTB configuration, we observe a DCD increase of 2.2 ps from 1.80 to 4.0 ps. Similarly, the jitter time exhibited an increase of of ~1.7 ps. This increase in both parameters resulted in reducing the eye width from 184 to 173.9 (~1ps/km). These observations are expected due to the chromatic dispersion that results in pulse spreading since the center wavelength of the emission is at a 330 nm red shift from the rated 1300 nm zero-dispersion wavelength in silica based optical fibers in addition to the wide emission bandwidth (~ 6nm). Therefore, between power attenuation (-0.4 dB/km) and pulse spreading (1 ps/km due to dispersion), power attenuation over the fiber link plays the limiting factor in determining fiber link length in our system. BER is a function of the Q-factor which is solely affected by the received power. Hence, in order to estimate the BER for different fiber lengths, we first estimated the fiber lengths that will attenuate the received power to the specific values that were examined in BTB configuration (-6.5, -8, -10, -14, -17, and -20 dBm) whose corresponding Q-factors had been previously acquired as shown earlier in this chapter.

These fiber length values were estimated using

$$P_o = P_{in} - \alpha L \tag{6.7}$$

where

- P_o is the desired attenuated optical power at the output of the fiber.
- P_{in} is the optical power at the input of the fiber (~ -6.5 dBm).
- α is the attenuation rate (0.4 dB/km).
- L is the fiber length in km.

Table 6.5 shows the estimated received powers and their corresponding Q-factors in addition to the measured case of 10 km fiber.

Table 6.5: The estimated received powers and their corresponding Q-factors in addition to the measured case (underlined) of 10 km fiber.

Fiber Length (km)	0	4	<u>10</u>	20	25	35
Received Power (dBm)	-6.5	-8	<u>-10.5</u>	-14	-17	-20
Q-factor	7.63	7.60	<u>6.57</u>	6.56	4.42	2.66

Figure 6.18 shows the estimated BER, using 6.5, over different fiber length values at 5Gb/s using the attenuation rate of 0.4 dB/km to estimate the Q-factor over each length while the dashed green line indicates the error-free transmission level (BER$\leq 10^{-9}$).

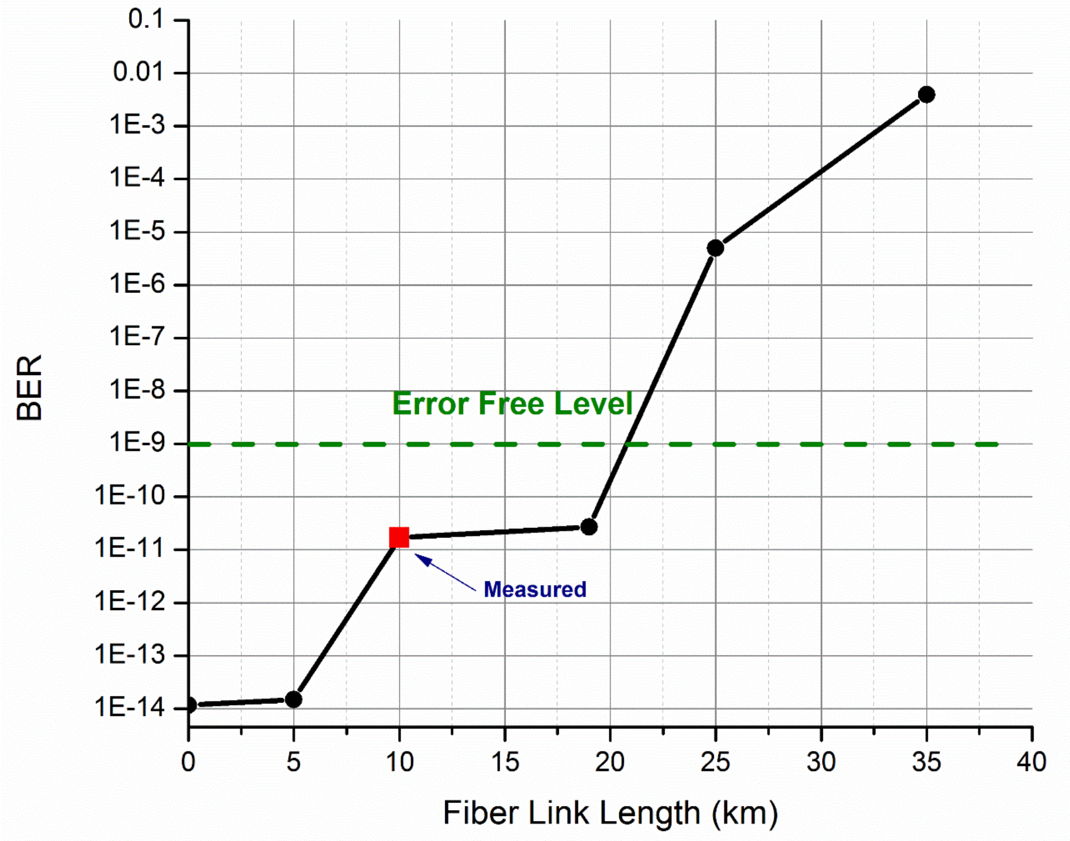

Figure 6.18: Estimated BER at different fiber lengths. The measured case is represented by the red mark. The dashed line indicates the error-free level.

From the figure, the fiber link length that results in error-free communication is estimated to be ~20 km. Moreover, the maximum length that results in an open eye diagram (~35 km) is associated with a BER of ~$10^{-2.5}$.

6.3 OOK Modulation of a Single Fabry-Perot Mode

The emission of the QDash laser has been passed through an optical tunable filter (OTF) to filter out a single FP mode as shown in Figure 6.19(a) which was then amplified employing two EDFAs to increase its optical power.

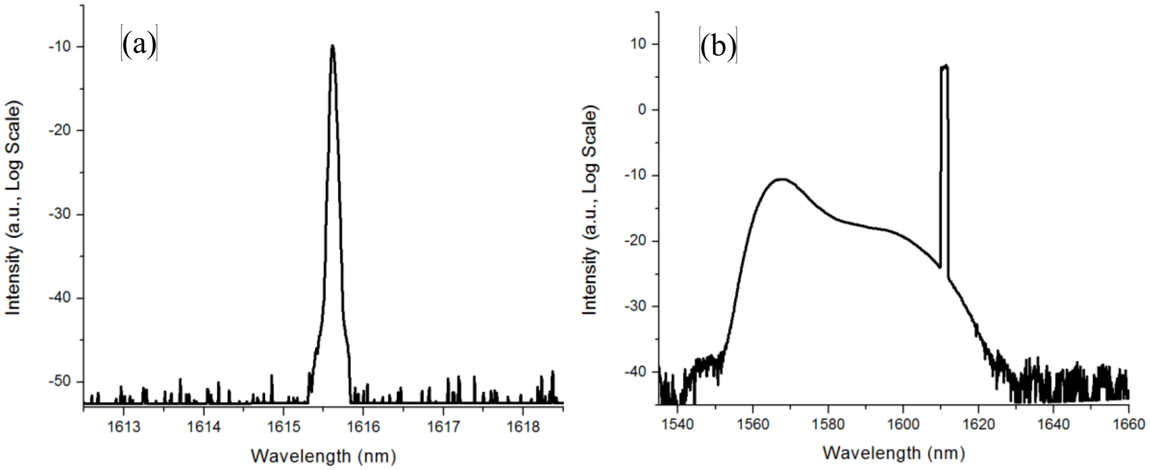

Figure 6.19: A filtered out single mode (a) before amplification and (b) after amplification.

However, because of the low optical power of the filtered mode due to insertion loss of the OTA and the inherent low power of the single mode, it was not possible to amplify the optical power of the filtered FP peak independently without amplifying the noise which is the amplified spontaneous emission (ASE) coming from the EDFA. As a result, successful modulation of this peak was not realizable.

However, a different technique has been implemented in order to achieve a single emission mode while attaining a relatively high power. This technique was injection locking in which a commercial laser diode of a tunable single emission mode is used as a master laser that is injected into a 4 µm x 700 µm QDash laser which is acting as a slave laser. When the emission of the master laser is injected into the slave laser, the emission of the latter is frequency locked to that of the master which causes an emission of identical wavelength to that of the master's. As shown in Figure 6.20, an optical circulator is used for injection locking. The master laser is inputted into port 1 of the optical circulator to be passed through port 2 to be injected into the QDash laser.

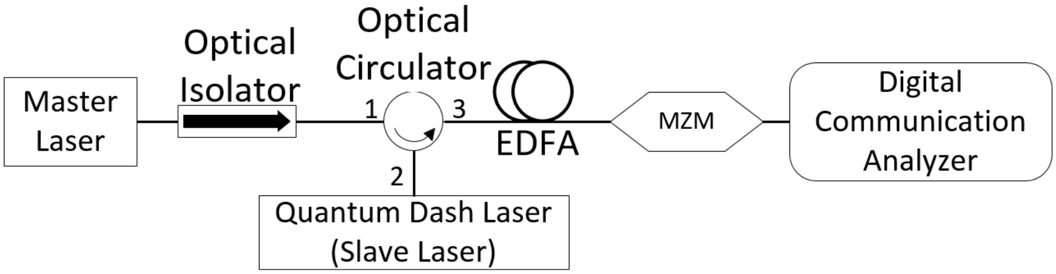

Figure 6.20: Block diagram showing the injection locking setup.

Only when the wavelength of the master laser was tuned to one of FP modes of the QDash laser (1617.6 nm) with a precision of 0.01 nm while keeping a power ratio of +5 dB between the optical power of the master and slave lasers, injection locking occurs as shown in Figure 6.21 where the emission spectra of the QDash laser before and after locking are shown in blue and red, respectively.

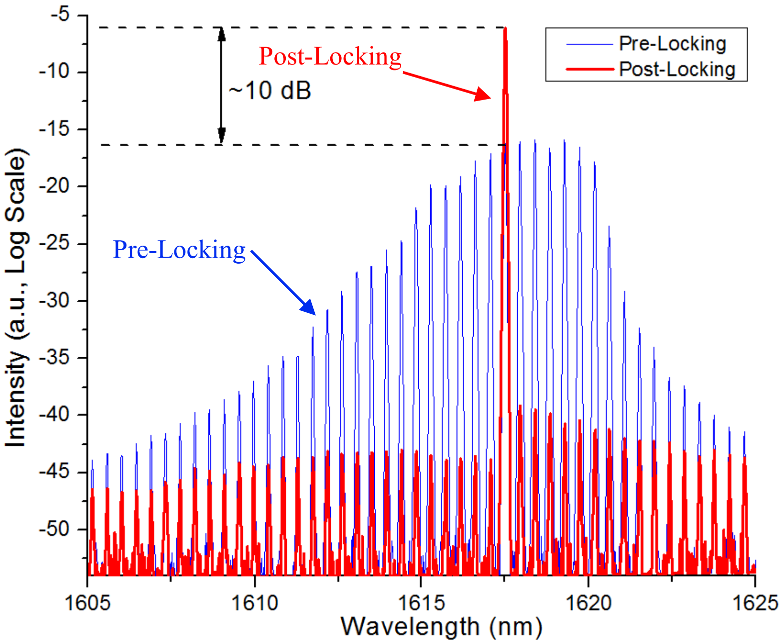

Figure 6.21: Emission spectra of the 4µm x 700 µm QDash laser before and after injection locking.

In addition to lasing into a single FP mode that matches that of the master laser, a 10 dB gain is exhibited by that mode while the integrated average power in spectra was identical in both cases which was equal to ~ -5 dBm.

Finally, this peak was then amplified through an EDFA and then successfully used in OOK modulation over the same setup shown in Figure 6.8. Figure 6.22 shows the bit pattern (top) and eye (bottom) diagrams of the recovered signal.

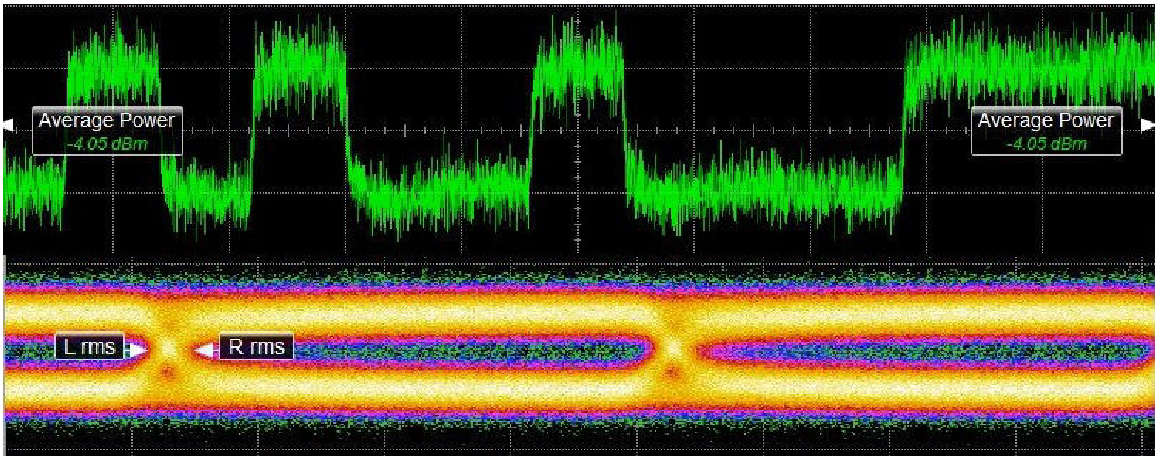

Figure 6.22: Bit pattern diagram (top) and eye diagram (bottom) of the recovered signal while using the injection-locked QDash laser as an optical source.

However, due to the non-negligible presence of ASE, accurate measurement of the communication parameters becomes obsolete.

CHAPTER 7

CONCLUSIONS AND POTENTIAL FUTURE WORK EXPANSION

7.1 Thesis Conclusion

The most significant conclusions of this work involve four main points:

- Investigating the performance and spectral characteristics of the chirped QDash laser including the effect of varying its geometrical parameters on these characteristics while demonstrating its ultra-broad emission due to its high inhomogeneity.
- Investigating the lasing operation of the QDash laser under higher duty cycle SPW and CW modes in terms of output optical power, performance and spectral characteristics, and the utilization of the structure's inhomogeneity.
- Investigating the temperature dependent lasing characterization via direct temperature rise or implicit temperature increase with high current injections and higher duty cycle SPW or CW operations.

- Highlighting the best geometrical, ambient, and operation conditions of the QDash laser in an OOK-modulation-based communication system and evaluating the system under these conditions in terms of data rate and fiber link length.

Firstly, we thoroughly investigated and acquired the fundamental laser diode principle parameters for several cavity lengths and two ridge width values, namely 2 µm and 4 µm. The material dependent internal quantum efficiency was found to be ~82% ± 1.5% while the internal loss was averaged around 11.3 cm^{-1} ± 0.55 cm^{-1}. The characteristic temperature was equal to ~73^{o} K. However, the size dependent transparency current density temperature showed better (lower) value for wider ridge devices which is ~ 2183.4 A/cm^2 while the narrower devices showed a transparency current density of ~ 3349.07 A/cm^2. Moreover, an ultra-broad emission of has been demonstrated ~ 38.4 nm (4.41 THz) as a result of the inhomogeneous nature of this structure.

Secondly, we extensively inspected higher order SPW and CW operation modes and their effect on the lasing characteristics. Due to the non-optimal growth nature of our research-based QDash laser specimens, higher order SPW and CW are associated with heat generation within the active medium resulting in reducing the quantum efficiency of the device and accelerating the quenching of the stimulated emission at higher current injections leading ultimately in reducing the peak optical output power. This heat instability is affirmed by the lower characteristic temperature of 56^o K associated with this laser in CW when compared to that of 0.2% SPW mode which was found to be 73^o K. Nevertheless, the rate at which the integrated average power increases in these modes exceeds that of the peak power reduction resulting in a total net of integrated power increase. Furthermore, as a result of the thermionic enhancement effect due to the heat buildup in higher order modes, more electrons are transitioned into the conduction band which resulted in earlier population inversion and stimulated emission occurrence as evident by the lower (7%) transparency threshold current density of 2024 A/cm^2 showed in CW operation when compared to 0.2% SPW. In addition, QDashes of sizes that are not able to achieve stimulated emission in SPW mode become able to overcome the active medium losses and achieve stimulated emission in CW mode. As a result, emission of more spectral wavelength components is achieved resulting in more utilization of the structure inhomogeneity and spectral broadening. On the other hand, as heat is built up, carriers within shallowly confined QDash ensembles become able to escape the quantum confinement and leak out causing severe quenching of their associated emission components especially in CW mode where only a single QDash stack (deepest confined S10 stack) is able to sustain stimulated emission.

Thirdly, we extensively investigated the temperature dependent spectral profile of these structures. In general, narrower ridge width laser devices behaved as a well decoupled system of QDash ensembles resulting in dissimilar emission wavelengths and more exploitation of the inhomogeneous nature of these structures that is further increased as temperature is increased directly or indirectly as more current is being injected. On the other hand, wider ridge showed high coupling between the different QDash stacks resulting in narrower emission. As temperature and temperature increases, the different stacks become more strongly coupled due to phonon-assisted tunneling. Both increasing the temperature and the inherent temperature rise at high current injections generally resulted in red shifting the emission spectra due to the resulting bandgap shrinkage. Moreover, due to thermionic emission, higher junction temperature resulted in emission broadening as more as more optical transitions become available. However, this broadening occurs at the expense of deteriorating the quantum efficiency of the device due to thermally induced carrier leakage, especially in the case of small offset potential dash ensembles. Depending on the application in which these QDash lasers are to be employed in, proper optimization of the geometrical dimensions, temperature, and operation mode becomes crucial to balance out the trade-off emission broadband and output optical power.

Finally, in OOK-modulation-based communication system, we prioritized the output optical power and short emission center wavelength, since emission bandwidth does not affect this scheme in short-haul OOK communications. Hence, we used an intermediate length laser device of length of 1100 µm while choosing the widest ridge width. Moreover, the temperature was kept at low 15°C under CW operation for continuous signal modulation. In back-to-back configuration, maximum transmission rate that resulted in an open eye was 20 Gb/s while error-free transmission (BER$\leq 10^{-9}$) was achieved at 10 Gb/s. Thereafter, through a 10-km fiber link, transmission at 5 Gb/s, was achieved with an attenuation rate of 0.4 dB/km. Given our power budget (~14 dB), power attenuation plays the limiting factor in determining the fiber link length since its rate far exceeds that of pulse spreading due to dispersion at which the eye-width is diminished (-1 ps/km) in perspective with the eye-width of the reference case (184 ps). Therefore, the maximum length of the fiber that results in an open eye is estimated to be ~ 35 km while maximum fiber length associated with error-free transmission is estimated to be ~ 20 km.

7.2 Future Work

The results obtained in the study presented in this work constitutes a foundation over which this novel structure of chirped QDash lasers can be employed as a source in system level applications. We demonstrated in this work such application which is OOK communication. However, further expansion and different applications can be achieved.

- Proper optimization of the multi-stack active region in order to fully utilize optical transitions while maintaining high quantum efficiency to achieve ultra-broad emission without compromising the optical power.

- In order to increase the coupled optical power into the fiber, passive optical components, such as lenses, can be used. Moreover, multi-mode fibers can be used instead of single-mode fibers in applications where pulse spreading and dispersion pose minor influence such as OOK in short-haul communication systems.

- Post-growth bandgap engineering (Intermixing) is advised in order to blue shift the QDash laser emission and bring it as close as possible to C- and early L-bands to reduce the power attenuation over fibers links in addition for their emission to be more compatible with different communication system elements and equipment.

- Higher data rates can be achieved through higher order modulation schemes, such as QDPSK and M-ary QAM. However, the linewidth of the FP modes needs to be reduced in order to decrease the chromatic dispersion, increase the temporal coherence and coherence length, and reduce the phase mismatch in coherent demodulation which becomes necessary in these modulation schemes.

- Injection-locking is one technique that can be used to reduce the linewidth of the FP modes while amplifying the optical power of the locked-mode.

- Mode-locking is another technique that can be used to eliminate the phase noise between the different FP modes which can be achieved through an external cavity or monolithically by separating the structure into an active amplifying region and an absorbing region.

- Aside from communication systems, a myriad of applications can benefit greatly from the ultra-broad emission such as tunable amplifiers and biochemical sensing and monitoring.

Bibliography

[1] R. Krebs, Groundbreaking scientific experiments, inventions, and discoveries of the Middle Ages and the Renaissance. Westport, CT: Greenwood Press, 2004.

[2] Hong, I-Wei. “Dispersion compensation in fiber optic communication systems.” (2002).

[3] M. Karbassian. “Optical Communications and Networks - Review and Evolution” (2012).

[4] David R. Goff. Fiber Optic Video Transmission, 1st ed. Focal Press Woburn, Massachusetts, 2003

[5] Kao, K. C., and George A. Hockham. "Dielectric-fibre surface waveguides for optical frequencies." Proceedings of the Institution of Electrical Engineers. Vol. 113. No. 7. IET Digital Library, 1966.

[6] Hill, Goff. The Cable and Telecommunications Professionals' Reference: PSTN, IP and cellular networks, and mathematical techniques. Vol. 1. Taylor & Francis, 2007.

[7] F. P. Kapron, D. B. Keck, and R. D. Maurer, "Radiation losses in glass optical waveguides," Applied Physics Letters 17 pp. 423-425, Nov. 15, 1970, p. 423. 28.

[8] Steele, Robert V. (February 1, 2005). "Diode-laser market grows at a slower rate". Laser Focus World 41 (2).

[9] Massa, Nick. "Fiber optic telecommunication." Fundamentals of Photonics. University of Conneticut (2000).

[10] R. N. Hall, G. E. Fenner, J. D. Kingsley, T. J. Soltys, and R. O.Carlson, “Coherent Light Emission From GaAs Junctions,”Physical Review Letters, Vol. 9, Issue 9, pp. 366-368, 1962.

[11] Ujager, Farhan S., S. M. H. Zaidi, and Usman Younis. "A review of semiconductor lasers for optical communications." 7th International Symposium on High-capacity Optical Networks and Enabling Technologies. 2010.

[12] Zhang, Yuchi. "Review of free-space optical communications with diverging beam." (2011).

[13] D. Kedar and S. Arnon, \Urban optical wireless communication networks: the main challenges and possible solutions," Communications Magazine, IEEE, vol. 42, no. 5, pp. s2, 2004.

[14] Dutton, Harry JR. Understanding optical communications. Prentice Hall PTR, 1998.

[15] Paschotta, 'Encyclopedia of Laser Physics and Technology - optical fiber communications, data transmission, capacity, telecom windows, C band, L band, WDM', Rp-photonics.com, 2015. [Online]. Available: https://www.rp-photonics.com/optical_fiber_communications.html.

[16] Gaponenko, Sergey V. Optical properties of semiconductor nanocrystals. Vol. 23. Cambridge university press, 1998.

[17] Harrison, Paul. Quantum wells, wires and dots: theoretical and computational physics of semiconductor nanostructures. John Wiley & Sons, 2005.

[18] Toma T., Takizuka T., Kanou M., Taniguchi T., Koike Y. Dual full high definition 3D video real-time communication system. In: International Conference on Plastic Optical Fibers, ICPOF 2011, Bilbao, Spain, 2011, 475-479.

[19] Brackett, Charles. "Dense wavelength division multiplexing networks: Principles and applications." Selected Areas in Communications, IEEE Journal on 8.6 (1990): 948-964.

[20] Tan, Chee L., Boon S. Ooi, and Hery S. Djie. Broadband Emission in Quantum-Dash Semiconductor Laser. INTECH Open Access Publisher, 2010.

[21] Kroemer, H. (1963). A proposed class of heterojunction lasers, Proc. IEEE 5 1, 1782-1783.

[22] Wood al l, J. M., Rupprecht, H., and Petti t, G. D. (1967). Solid state device conference, June 19, 1967, Santa Barbara, California. [Abstract reported in IEEE Trans. Electron. Devices ED-14, 630 (1967).]

[23] Zory, Peter S. Quantum well lasers. Academic Press, 1993.

[24] Van Ruyven, L. J. "Double heterojunction lasers and quantum well lasers." Journal of luminescence 29.5 (1984): 123-161.

[25] Alferov, Zhores. "Double heterostructure lasers: early days and future perspectives." IEEE Journal of Selected Topics in Quantum Electronics 6.6 (2000): 832-840.

[26] Alferov, Zhores I. "Nobel Lecture: The double heterostructure concept and its applications in physics, electronics, and technology." Reviews of modern physics 73.3 (2001): 767.

[27] Miller, R. C., et al. "Laser oscillation with optically pumped very thin GaAs-AlxGa1− xAs multilayer structures and conventional double heterostructures." Journal of Applied Physics 47.10 (1976): 4509-4517.

[28] Holonyak Jr, N., et al. "Low-threshold continuous laser operation (300–337° K) of multilayer MO-CVD AlxGa1− xAs-GaAs quantum-well heterostructures." Applied Physics Letters 33.8 (1978): 737-739.

[29] Dupuis, R. D., et al. "Continuous room-temperature multiple-quantum-well AlxGa1− xAs-GaAs injection lasers grown by metalorganic chemical vapor deposition." Applied Physics Letters 35.7 (1979): 487-489.

[30] Nelson, R. J., et al. "High-output power InGaAsP (λ= 1.3 μm) strip-buried heterostructure lasers." Applied Physics Letters 36.5 (1980): 358-360.

[31] InGaAsP double heterostructure lasers (lambda=1.3 µm) with etched reflectors. Appl. Phys. Lett. 36, 518 (1980); 10.1063/1.91565

[32] Low-threshold 1.3-µm GaInAsP/InP buried heterostructure lasers by liquid phase epitaxy and metalorganic chemical vapor deposition Appl. Phys. Lett. 39, 188 (1981); 10.1063/1.92697

[33] A.G.Foyt, J. Cryst. Growth. 54, no.1, pp.1-8 (1981).

[34] Koren, U., et al. "Low internal loss separate confinement heterostructure InGaAs/InGaAsP quantum well laser." Applied physics letters 51.21 (1987): 1744-1746.

[35] InGaAs/InGaAsP distributed feedback quantum well laser with an intracavity phase modulator Appl. Phys. Lett. 53, 2132 (1988); 10.1063/1.100296.

[36] Dupuis, Russell D., et al. "Room-temperature laser operation of quantum-well Ga (1− x) AlxAs-GaAs laser diodes grown by metalorganic chemical vapor deposition." Applied physics letters 32.5 (1978): 295-297.

[37] Coleman, James J., Jonathan D. Young, and Akash Garg. "Semiconductor quantum dot lasers: a tutorial." Lightwave Technology, Journal of 29.4 (2011): 499-510.

[38] Khan, Mohammed Zahed Mustafa, Tien Khee Ng, and Boon S. Ooi. "Self-assembled InAs/InP quantum dots and quantum dashes: Material structures and devices." Progress in Quantum Electronics 38.6 (2014): 237-313.

[39] Alghoraibi, Ibrahim, et al. "InAs self-assembled quantum dot and quantum dash lasers on InP for 1.55 µm optical telecommunications." Information and Communication Technologies, 2006. ICTTA'06. 2nd. Vol. 2. IEEE, 2006.

[40] D. Bimberg, M. Grundmann, and N. N. Ledentsov, Quantum dot heterostructures: John Wiley & Sons, 1999.

[41] Zhukov, M. Maksimov, and A. Kovsh, "Device characteristics of long-wavelength lasers based on self-organized quantum dots," Semiconductors, vol. 46, pp. 1225-1250, 2012.

[42] Kovsh, A.; Krestnikov, I.; Livshits, D.; Mikhrin, S.; Weimert, J. & Zhukov, A. (2007). Quantum dot laser with 75 nm broad spectrum of emission. Opt. Lett., Vol. 32, No. 7, (April 2007) 793-795.

[43] Huolei, Wang, et al. "InGaAs/GaAs quantum well laser with broad spectrum of stimulated emission at 1.06 µm." CLEO: QELS_Fundamental Science. Optical Society of America, 2014.

[44] Bauer, Ernst. "Phänomenologische theorie der kristallabscheidung an oberflächen. II." Zeitschrift für Kristallographie-Crystalline Materials 110.1-6 (1958): 395-431.

[45] V. Ustinov, A. Zhukov, A. Y. Egorov, A. Kovsh, S. Zaitsev, N. Y. Gordeev, et al., "Low threshold quantum dot injection laser emitting at 1.9µm," Electronics Letters, vol. 34, pp. 670-672, 1998.

[46] K. Nishi, M. Yamada, T. Anan, A. Gomyo, and S. Sugou, "Long-wavelength lasing from InAs self-assembled quantum dots on (311) B InP,"Applied Physics Letters, vol. 73, pp. 526-528, 1998.

[47] P. Caroff, C. Paranthoen, C. Platz, O. Dehaese, H. Folliot, N. Bertru, et al., "High-gain and low-threshold InAs quantum-dot lasers on InP,"Applied Physics Letters, vol. 87, pp. 243107-243107-3, 2005.

[48] E. Homeyer, R. Piron, F. Grillot, O. Dehaese, K. Tavernier, E. Macé, et al., "First demonstration of a 1.52 µm RT InAs/InP (3 1 1) B laser with an active zone based on a single QD layer," Semiconductor Science and Technology, vol. 22, p. 827, 2007.

[49] K. Klaime, C. Calò, R. Piron, C. Paranthoen, D. Thiam, T. Batte, et al., "23 and 39 GHz low phase noise monosection InAs/InP (113)B quantum dots mode-locked lasers," Optics Express, vol. 21, pp. 29000-29005, 2013/11/18 2013.

[50] H. Saito, K. Nishi, and S. Sugou, "Ground-state lasing at room temperature in long-wavelength InAs quantum-dot lasers on InP (311) B substrates," Applied Physics Letters, vol. 78, pp. 267-269, 2001.

[51] K. Akahane, N. Yamamoto, H. Sotobayashi, and M. Tsuchiya, "1.7-µm laser emission at room temperature using highly-stacked InAs quantum dots," in

Indium Phosphide and Related Materials, 2008. IPRM 2008. 20th International Conference on, 2008, pp. 1-3.

[52] K. Akahane, N. Yamamoto, and T. Kawanishi, "The dependence of the characteristic temperature of highly stacked InAs quantum dot laser diodes fabricated using a strain-compensation technique on stacking layer number," in Semiconductor Laser Conference (ISLC), 2012 23rd IEEE International, 2012, pp. 82-83.

[53] K. Akahane, N. Yamamoto, and T. Kawanishi, "Wavelength tunability of highly stacked quantum dot laser fabricated by a strain compensation technique," in Semiconductor Laser Conference (ISLC), 2010 22nd IEEE International, 2010, pp. 37-38.

[54] S. Bhowmick, M. Z. Baten, T. Frost, B. S. Ooi, and P. Bhattacharya, "High Performance InAs/In0. 53Ga0. 23Al0. 24As/InP Quantum Dot 1.55 µm Tunnel Injection Laser," IEEE Journal of Quantum Electronics, vol. 50, pp. 7-14, 2013.

[55] R. Wang, A. Stintz, P. Varangis, T. Newell, H. Li, K. Malloy, et al., "Room-temperature operation of InAs quantum-dash lasers on InP [001]," IEEE Photonics Technology Letters, vol. 13, pp. 767-769, 2001.

[56] R. Schwertberger, D. Gold, J. Reithmaier, and A. Forchel, "Long-wavelength InP-based quantum-dash lasers," IEEE Photonics Technology Letters, vol. 14, pp. 735-737, 2002.

[57] T. Rotter, A. Stintz, and K. Malloy, "InP based quantum dash lasers with 2 µm wavelength," in IEE Proceedings Optoelectronics 2003, pp. 318-321.

[58] S. Deubert, A. Somers, W. Kaiser, R. Schwertberger, J. Reithmaier, and A. Forchel, "InP-based quantum dash lasers for wide gain bandwidth applications," Journal of Crystal Growth, vol. 278, pp. 346-350, 2005.

[59] Somers, W. Kaiser, J. Reithmaier, and A. Forchel, "InP-based quantum dash lasers for broadband optical amplification and gas sensing applications," in International Conference on Indium Phosphide and Related Materials, 2005. , 2005, pp. 56-59.

[60] M. Z. M. Khan, T. K. Ng, C.-S. Lee, P. Bhattacharya, and B. S. Ooi, "Investigation of Chirped InAs/InGaAlAs/InP Quantum Dash Lasers as Broadband Emitters," IEEE Journal of Qantum Electronics, vol. 50, pp. 51-61, 2014.

[61] Zhukov, M. Maksimov, and A. Kovsh, "Device characteristics of long-wavelength lasers based on self-organized quantum dots," Semiconductors, vol. 46, pp. 1225-1250, 2012.

[62] Akrout, Akram, et al. "Separate error-free transmission of eight channels at 10 Gb/s using comb generation in a quantum-dash-based mode-locked laser." Photonics Technology Letters, IEEE 21.23 (2009): 1746-1748.

[63] Nguyen, Quoc Thai, et al. "16x2. 5 Gbit/s Downstream Transmission in Colorless WDM-PON based on Injection-Locked Fabry-Perot Laser Diode using a single Quantum Dash mode-locked Fabry-Perot laser as multi-wavelength seeding source." Optical Fiber Communication Conference. Optical Society of America, 2009.

[64] M'Sallem, Yousra Ben, et al. "Quantum-dash mode-locked laser as a source for 56-Gb/s DQPSK modulation in WDM multicast applications." IEEE Photonics Technology Letters 23.7 (2011): 453-455.

[65] Pfeifle, Joerg, et al. "Coherent Terabit Communications using a Quantum-Dash Mode-Locked Laser andSelf-Homodyne Detection." Optical Fiber Communication Conference. Optical Society of America, 2015.

[66] Mobarhan, Kamran S. "Test and characterization of laser diodes: determination of principal parameters." Newport Corporation (1995).

[67] Ban, D., et al. "Direct observation of lateral current spreading in ridge waveguide lasers using scanning voltage microscopy." Applied physics letters 82.23 (2003): 4166-4168.

[68] Shi-Guo, Li, et al. "Junction-Temperature Measurement in InAs/InP (100) Quantum-Dot Lasers." Chinese Physics Letters 32.1 (2015): 014208.

[69] Kittel, Charles. Introduction to solid state physics. Wiley, 2005.

[70] K. Nishi, H. Saito, S. Sugou, and J. S. Lee, “A narrow photoluminescence linewidth of 21 meV at 1.35 µm from strain-reduced InAs quantum dots covered by In0.2Ga0.8As grown on GaAs substrates,” Appl. Phys. Lett., vol. 74, no. 8, pp. 1111–1113, 1999.

[71] Li, S. G., et al. "Cavity Length and Stripe Width dependent Lasing Characteristics of InAs/InP (100) quantum dot lasers." Infrared Physics & Technology (2016).

[72] Li, S. G., et al. "Thermal coefficient of InP-based quantum dot laser from cavity-mode measurements." Infrared Physics & Technology 68 (2015): 119-123.

[73] P. Miska, J. Even, C. Paranthoen, O. Dehaese, A. Jbeli, M. Senes, et al., “Vertical electronic coupling between InAs/InP quantum-dot layers emitting in the near-infrared range,” Appl. Phys. Lett., vol. 86, pp. 111905-1–111905-3, Mar. 2005.

[74] Anritsu, Application Note No. 11410 pp.5-11.

[75] Freude, Wolfgang, et al. "Quality metrics for optical signals: eye diagram, Q-factor, OSNR, EVM and BER." Transparent Optical Networks (ICTON), 2012 14th International Conference on. IEEE, 2012.

[76] Haykin, Simon. Communication systems. John Wiley & Sons, 2008.

[77] Alic, N., et al. "Performance Bounds of MLSE in Intensity Modulated Fiber Optic Links." Optical Communication Theory and Techniques. Springer US, 2005. 197-203.

[78] Zweck, John, and Curtis R. Menyuk. Validity of the additive white Gaussian noise model for quasi-linear long-haul return-to-zero optical fiber communications systems. Lightwave Technology, Journal of 27.16 (2009) 3324-3335.

[79] Chan, Benjamin, and Jan Conradi. "On the non-Gaussian noise in erbium-doped fiber amplifiers." Journal of lightwave technology 15.4 (1997): 680-687.

[80] Dahlgren, Robert. "Noise in fiber optic communication links." signal 2.2.

Vitae

Name : Emad AbdulShafi Moawad Moustafa Alkhazraji.

Nationality : Egyptian.

Date of Birth : June 15th, 1992.

Email : pxemad@hotmail.com, alkhazraji@kfupm.edu.sa

Address : 9-931 Al-Bustan, Jubail 31961, Saudi Arabia.

Academic Background :

- Master of Science (M.Sc) in Electrical Fingering, King Fahd University of Petroleum and Minerals, May 2016.
- Bachelor of Science (B.Sc) in Electrical Engineering, King Fahd University of Petroleum and Minerals, June 2014.

Publication :

- E. Alkhazraji, M. A. Alsunaidi, "Analysis of Voids in a Nanorod Plasmonic Cluster for Imaging Applications," (Accepted in META'16, Malaga, Spain).

- E. Alkhazraji, A. Ghalib, K. Manzoor and M. A. Alsunaidi, “Scattering Characteristics of Plasmonic Nanostructured Cellular Automata”. (Accepted in AFMAT 2015, Turkey)
- E. Alkhazraji, M. Shemis, M. Najmi, M. A. Abalkhail, and M. A. Alsunaidi, “Development of ZnO Plasmonics as Novel Materials for Enhanced Florescence Light-emitters”. (Presented in The 3rd Saudi International Nanotechnology Conference, 2014)
- Alhadidi, H. Al-Taweel, A. Al-Dakhil, A. Al-Zahrani, E. Alkhazraji and M. A. Alsunaidi, "Efficient light extraction from GaN LEDs using gold-coated ZnO nanoparticles," Applied Electrical Engineering and Computing Technologies (AEECT), 2015 IEEE Jordan Conference on, Amman, 2015, pp. 1-3. (Published)
- M. Shemis, M. Gondal, E. Alkhazraji, M. Najmi, M. A. Abalkhail, I. Khan, T. B. Susilo, S. G. Rashid and M. A. Alsunaidi, “Synthesis and Photoluminescence of Metal Coated ZnO Nanoparticles,” IEEE HONET 2014, Charlotte, NC, USA. (Published)